FERMILAB-PUB-14-548-AE

Submitted to ApJS
Preprint typeset using LaTeX style emulateapj v. 08/22/09

arXiv:1409.0850v1 [astro-ph.CO] 2 Sep 2014

GALAXY CLUSTERS DISCOVERED VIA THE SUNYAEV-ZEL'DOVICH EFFECT IN THE 2500-SQUARE-DEGREE SPT-SZ SURVEY

L. E. Bleem[1,2,3], B. Stalder[4], T. de Haan[5], K. A. Aird[6], S. W. Allen[7,8,9], D. E. Applegate[10], M. L. N. Ashby[4], M. Bautz[11], M. Bayliss[4,12], B. A. Benson[2,13,14], S. Bocquet[15,16], M. Brodwin[17], J. E. Carlstrom[1,2,3,14,18], C. L. Chang[1,2,18], I. Chiu[15,16], H. M. Cho[19], A. Clocchiatti[20], T. M. Crawford[2,14], A. T. Crites[2,14,21], S. Desai[15,16], J. P. Dietrich[15,16], M. A. Dobbs[5,22], R. J. Foley[4,23,24], W. R. Forman[4], E. M. George[25,26], M. D. Gladders[2,14], A. H. Gonzalez[27], N. W. Halverson[28], C. Hennig[15,16], H. Hoekstra[29], G. P. Holder[5], W. L. Holzapfel[25], J. D. Hrubes[6], C. Jones[4], R. Keisler[2,3,7,8], L. Knox[30], A. T. Lee[25,31], E. M. Leitch[2,14], J. Liu[15,16], M. Lueker[21,25], D. Luong-Van[6], A. Mantz[2], D. P. Marrone[32], M. McDonald[11], J. J. McMahon[33], S. S. Meyer[2,3,14,18], L. Mocanu[2,14], J. J. Mohr[15,16,26], S. S. Murray[4], S. Padin[2,14,21], C. Pryke[34], C. L. Reichardt[25,35], A. Rest[36], J. Ruel[12], J. E. Ruhl[37], B. R. Saliwanchik[37], A. Saro[15], J. T. Sayre[37], K. K. Schaffer[2,18,38], T. Schrabback[10], E. Shirokoff[21,25], J. Song[33], H. G. Spieler[31], S. A. Stanford[30,39], Z. Staniszewski[21,37], A. A. Stark[4], K. T. Story[2,3], C. W. Stubbs[4,12], K. Vanderlinde[40,41], J. D. Vieira[23,24], A. Vikhlinin[4], R. Williamson[2,14,21], O. Zahn[25,42], and A. Zenteno[15,43]

Submitted to ApJS

ABSTRACT

We present a catalog of galaxy clusters selected via their Sunyaev-Zel'dovich (SZ) effect signature from 2500 deg^2 of South Pole Telescope (SPT) data. This work represents the complete sample of clusters detected at high significance in the 2500 deg^2 SPT-SZ survey, which was completed in 2011. A total of 677 (409) cluster candidates are identified above a signal-to-noise threshold of $\xi = 4.5$ (5.0). Ground- and space-based optical and near-infrared (NIR) imaging confirms overdensities of similarly colored galaxies in the direction of 516 (or 76%) of the $\xi > 4.5$ candidates and 387 (or 95%) of the $\xi > 5$ candidates; the measured purity is consistent with expectations from simulations. Of these confirmed clusters, 415 were first identified in SPT data, including 251 new discoveries reported in this work. We estimate photometric redshifts for all candidates with identified optical and/or NIR counterparts; we additionally report redshifts derived from spectroscopic observations for 141 of these systems. The mass threshold of the catalog is roughly independent of redshift above $z \sim 0.25$ leading to a sample of massive clusters that extends to high redshift. The median mass of the sample is $M_{500c}(\rho_{\rm crit}) \sim 3.5 \times 10^{14}\, M_\odot\, h_{70}^{-1}$, the median redshift is $z_{\rm med} = 0.55$, and the highest-redshift systems are at $z >$1.4. The combination of large redshift extent, clean selection, and high typical mass makes this cluster sample of particular interest for cosmological analyses and studies of cluster formation and evolution.

Subject headings: cosmology: observations – galaxies: clusters: individual – large-scale structure of universe

[1] Argonne National Laboratory, High-Energy Physics Division, 9700 S. Cass Avenue, Argonne, IL, USA 60439
[2] Kavli Institute for Cosmological Physics, University of Chicago, 5640 South Ellis Avenue, Chicago, IL 60637
[3] Department of Physics, University of Chicago, 5640 South Ellis Avenue, Chicago, IL 60637
[4] Harvard-Smithsonian Center for Astrophysics, 60 Garden Street, Cambridge, MA 02138
[5] Department of Physics, McGill University, 3600 Rue University, Montreal, Quebec H3A 2T8, Canada
[6] University of Chicago, 5640 South Ellis Avenue, Chicago, IL 60637
[7] Kavli Institute for Particle Astrophysics and Cosmology, Stanford University, 452 Lomita Mall, Stanford, CA 94305
[8] Department of Physics, Stanford University, 382 Via Pueblo Mall, Stanford, CA 94305
[9] SLAC National Accelerator Laboratory, 2575 Sand Hill Road, Menlo Park, CA 94025
[10] Argelander-Institut für Astronomie, Auf dem Hügel 71, D-53121 Bonn, Germany
[11] Kavli Institute for Astrophysics and Space Research, Massachusetts Institute of Technology, 77 Massachusetts Avenue, Cambridge, MA 02139
[12] Department of Physics, Harvard University, 17 Oxford Street, Cambridge, MA 02138
[13] Fermi National Accelerator Laboratory, Batavia, IL 60510-0500
[14] Department of Astronomy and Astrophysics, University of Chicago, 5640 South Ellis Avenue, Chicago, IL 60637
[15] Department of Physics, Ludwig-Maximilians-Universität, Scheinerstr. 1, 81679 München, Germany
[16] Excellence Cluster Universe, Boltzmannstr. 2, 85748 Garching, Germany
[17] Department of Physics and Astronomy, University of Missouri, 5110 Rockhill Road, Kansas City, MO 64110
[18] Enrico Fermi Institute, University of Chicago, 5640 South Ellis Avenue, Chicago, IL 60637
[19] NIST Quantum Devices Group, 325 Broadway Mailcode 817.03, Boulder, CO, USA 80305
[20] Departamento de Astronomia y Astrosifica, Pontificia Universidad Catolica, Chile
[21] California Institute of Technology, 1200 E. California Blvd., Pasadena, CA 91125
[22] Canadian Institute for Advanced Research, CIFAR Program in Cosmology and Gravity, Toronto, ON, M5G 1Z8, Canada
[23] Astronomy Department, University of Illinois at Urbana-Champaign, 1002 W. Green Street, Urbana, IL 61801 USA
[24] Department of Physics, University of Illinois Urbana-Champaign, 1110 W. Green Street, Urbana, IL 61801 USA
[25] Department of Physics, University of California, Berkeley, CA 94720
[26] Max-Planck-Institut für extraterrestrische Physik, Giessenbachstr. 85748 Garching, Germany
[27] Department of Astronomy, University of Florida, Gainesville, FL 32611
[28] Department of Astrophysical and Planetary Sciences and Department of Physics, University of Colorado, Boulder, CO 80309
[29] Leiden Observatory, Leiden University, Niels Bohrweg 2, 2333

Operated by Fermi Research Alliance, LLC under Contract No. De-AC02-07CH11359 with the United States Department of Energy.

1. INTRODUCTION

Galaxy clusters are the largest collapsed objects in the universe, and their abundance is exponentially sensitive to the conditions and processes that govern the cosmological growth of structure (see Allen et al. 2011 and references therein). In particular, measurements of cluster abundance have the power to constrain the matter density, the amplitude and shape of the matter power spectrum, and the sum of the neutrino masses (Wang & Steinhardt 1998; Wang et al. 2005; Lesgourgues & Pastor 2006), and to test models of the cosmic acceleration (Wang & Steinhardt 1998; Haiman et al. 2001; Weinberg et al. 2013) in ways that complement constraints from other observational methods. Clusters are also unique laboratories in which to characterize the interplay between gravitational and astrophysical processes (see Kravtsov & Borgani 2012 for a recent review). Well-defined cluster samples over a broad redshift range are critical for such studies.

Large samples of clusters were first compiled from optical and infrared datasets, in which clusters are identified as overdensities of galaxies. Clusters identified in this manner typically contain of tens to thousands of galaxies (e.g., Abell 1958; Gladders & Yee 2000; Koester et al. 2007; Eisenhardt et al. 2008; Wen et al. 2012; Rykoff et al. 2014). Clusters of galaxies are also bright sources of extended X-ray emission: the majority of the baryonic matter in clusters (70-95%) is found in the intracluster medium (ICM) in the form of diffuse gas that has been heated by adiabatic compression and shocks to X-ray emitting temperatures of 10^7 to 10^8 K (see review by Voit 2005). The observational expense of detecting high-redshift systems currently limits the size of X-ray samples; however, the tight correlation between ICM observables and the underlying cluster mass enables even modest samples of X-ray-selected systems to place competitive constraints on cosmological models (e.g., Vikhlinin et al. 2009; Mantz et al. 2010).

Over the past decade, clusters have begun to be identified via their signature in the millimeter-wave sky. As photons from the cosmic microwave background (CMB) pass through a galaxy cluster, roughly 1% of the photons will inverse-Compton scatter off the energetic electrons in the ICM. This imparts a characteristic spectral distortion to the CMB, known as the thermal Sunyaev-Zel'dovich (SZ) effect (Sunyaev & Zel'dovich 1972). The observed temperature difference, ΔT, relative to the mean CMB temperature, $T_{\rm CMB}$, is

$$\begin{aligned}\Delta T &= T_{\rm CMB}\ f_{\rm SZ}(x) \int n_{\rm e} \frac{k_{\rm B} T_{\rm e}}{m_{\rm e} c^2} \sigma_{\rm T} dl \\ &\equiv T_{\rm CMB}\ f_{\rm SZ}(x)\ y_{\rm SZ}\end{aligned} \tag{1}$$

where the integral is along the line of sight, $x \equiv h\nu/k_{\rm B}T_{\rm CMB}$, $k_{\rm B}$ is the Boltzmann constant, c the speed of light, $n_{\rm e}$ the electron density, $T_{\rm e}$ the electron temperature, $\sigma_{\rm T}$ the Thomson cross-section, $f_{\rm SZ}(x)$ encodes the frequency dependence of the thermal SZ effect:

$$f_{\rm SZ}(x) = \left(x \frac{e^x + 1}{e^x - 1} - 4 \right) (1 + \delta_{\rm rc}) \tag{2}$$

(Sunyaev & Zel'dovich 1980), and $y_{\rm SZ}$ is the Compton y-parameter. The term $\delta_{\rm rc}$ represents relativistic corrections (Nozawa et al. 2000), which become important at $T_{\rm e} \gtrsim 8$ keV. This frequency dependence leads to a decrement of observed photons (relative to a blackbody at $T_{\rm CMB}$) below the thermal SZ null frequency of $\sim$220 GHz and a corresponding increment of photons above this frequency. The surface brightness of the thermal SZ effect is independent of redshift, and the integrated thermal SZ signal is expected to be a low-scatter proxy for the cluster mass, as it is proportional to the total thermal energy of the ICM (Motl et al. 2005). These properties make cluster samples produced by SZ surveys attractive for cosmological analyses (Carlstrom et al. 2002).

The observed temperature distortions in the CMB caused by the thermal SZ effect are small, typically on the level of hundreds of $\mu{\rm K}_{\rm CMB}$ for the most massive clusters.[1] The development over the past decade of high-sensitivity bolometric cameras has enabled the wide and deep surveys required to find these rare systems via the SZ effect. The first discovery of a previously unknown cluster through its SZ signature was published in 2009 (Staniszewski et al. 2009); today such discoveries have become routine, with catalogs produced by the South Pole Telescope (SPT), Atacama Cosmology Telescope (ACT), and *Planck* teams containing tens to hundreds of massive clusters out to $z \sim 1.5$ (Reichardt et al. 2013; Hasselfield et al. 2013; Planck Collaboration et al. 2013a).

In this paper we present a cluster catalog extracted from the full 2500 deg^2 SPT-SZ survey. This sample consists of 677 galaxy cluster candidates detected at SPT statistical significance $\xi > 4.5$, of which 516 (76%) have been confirmed as clusters via dedicated optical and near-infrared (NIR) follow-up imaging. Follow-up imaging was obtained for all 477 candidates detected above

CA, Leiden, the Netherlands
[30] Department of Physics, University of California, One Shields Avenue, Davis, CA 95616
[31] Physics Division, Lawrence Berkeley National Laboratory, Berkeley, CA 94720
[32] Steward Observatory, University of Arizona, 933 North Cherry Avenue, Tucson, AZ 85721
[33] Department of Physics, University of Michigan, 450 Church Street, Ann Arbor, MI, 48109
[34] Physics Department, University of Minnesota, 116 Church Street S.E., Minneapolis, MN 55455
[35] School of Physics, University of Melbourne, Parkville, VIC 3010, Australia
[36] Space Telescope Science Institute, 3700 San Martin Dr., Baltimore, MD 21218
[37] Physics Department, Center for Education and Research in Cosmology and Astrophysics, Case Western Reserve University, Cleveland, OH 44106
[38] Liberal Arts Department, School of the Art Institute of Chicago, 112 S Michigan Ave, Chicago, IL 60603
[39] Institute of Geophysics and Planetary Physics, Lawrence Livermore National Laboratory, Livermore, CA 94551
[40] Dunlap Institute for Astronomy & Astrophysics, University of Toronto, 50 St George St, Toronto, ON, M5S 3H4, Canada
[41] Department of Astronomy & Astrophysics, University of Toronto, 50 St George St, Toronto, ON, M5S 3H4, Canada
[42] Berkeley Center for Cosmological Physics, Department of Physics, University of California, and Lawrence Berkeley National Labs, Berkeley, CA 94720
[43] Cerro Tololo Inter-American Observatory, Casilla 603, La Serena, Chile

[1] Throughout this work, noise units and amplitudes expressed in terms of $\rm K_{CMB}$ refer to the equivalent deviations in temperature from a 2.73 K blackbody required to produce the observed signals.

$\xi = 4.8$ and 172 (86%) of the remaining 200 candidates down to $\xi = 4.5$. For all confirmed clusters, we report photometric redshifts—or, where available, spectroscopic redshifts—and estimated masses. Of the confirmed clusters, 251 (49%) are reported for the first time in this work. Masses are computed using the framework developed for Reichardt et al. (2013, hereafter R13); we report masses using the best-fit ξ-mass relation for a fixed flat ΛCDM cosmology with $\Omega_{\rm m} = 0.3$, $h = 0.7$ and $\sigma_8 = 0.8$. A detailed cosmological analysis incorporating new information from follow-up X-ray observations will be presented in de Haan et al. (in preparation, hereafter referred to as dH14).

This paper is organized as follows. Observations and map-making are described in §2. The extraction of galaxy clusters from the maps is detailed in §3. We describe our optical and NIR follow-up campaign in §4 and associated confirmation of clusters and measurement of redshifts in §5. In §6 we present the full sample of galaxy cluster candidates from the 2500 deg^2 SPT-SZ cluster survey and highlight particularly notable clusters, and we conclude in §7. All masses are reported in terms of M_{500c}, where M_{500c} is defined as the mass enclosed within a radius at which the average density is 500 times the critical density at the cluster redshift. Selected data reported in this work, as well as future updates to the properties of these clusters, will be hosted at `http://pole.uchicago.edu/public/data/sptsz-clusters`.

2. OBSERVATIONS AND DATA REDUCTION

2.1. *Telescope and Observations*

The SPT (Carlstrom et al. 2011) is a 10 m diameter telescope located at the National Science Foundation Amundsen-Scott South Pole station in Antarctica. From 2008 to 2011 the telescope was used to conduct the SPT-SZ survey, a survey of ∼2500 deg^2 of the southern sky at 95, 150, and 220 GHz . The survey covers a contiguous region from 20^h to 7^h in right ascension (R.A.) and -65 to $-40°$ in declination (see, e.g., Figure 1 in Story et al. 2013) and was mapped to depths of approximately 40, 18, and 70 μK-arcmin at 95, 150, and 220 GHz respectively.

The telescope was designed for high-resolution measurements of the CMB, with particular attention to the science goal of discovering high-redshift galaxy clusters through the SZ effect. The large primary mirror leads to beam sizes of roughly 1.6′, 1.1′, and 1.0′ at 95, 150 and 220 GHz. Beams of this scale are well matched to the expected angular size of massive clusters at high redshift. For a non-relativistic thermal SZ spectrum, the centers of the measured 95 and 150 GHz bands are at 97.6 GHz and 152.9 GHz, while the 220 GHz band is approximately at the thermal SZ null.

The 2500 deg^2 SPT-SZ survey was not observed as one contiguous patch; rather it was broken into 19 subregions, or fields, individually scanned to survey depth. These fields range in size from ∼ 70 to 250 deg^2, and their borders overlap slightly (∼ 4%). The total area searched for clusters over all fields, after correcting for point-source masking (see §3) is 2365 deg^2.

The majority of fields were observed in an identical fashion: the telescope was scanned back and forth across the width of the field in azimuth and then stepped in elevation; the scan and step procedure was repeated until the full field had been imaged. The process, which constitutes a single *observation* of the field, took between 0.5 and 2.5 hours, depending on the field size and the elevation step. Each field was imaged in this fashion at least 200 times, and final maps are the sum of all individual observations. One field, RA21HDEC−50,[2] was observed with two different strategies: roughly one-third of the data were obtained with the strategy described above, while the remainder of the observations were conducted by scanning the telescope in elevation at a series of fixed azimuth angles. In Table 1 we have listed the name, location, area, and depths at 95, 150, and 220 GHz for each field, as well as the year in which the field was observed. The depth estimates are obtained as in Schaffer et al. (2011), using the Gaussian beam approximation described in that work.

The top two panels of Figure 1 show 6°-by-6° cutouts of 95 and 150 GHz maps from the RA21HDEC−60 field. The maps shown here have been very minimally filtered (high-passed at an angular multipole value of roughly $l = 50$ in the scan direction) and show the main signal components present in SPT-SZ survey data, namely the large-scale primary CMB fluctuations, emissive point sources, and SZ decrements from galaxy clusters. The data described in the next section and used as input to the cluster finding pipeline are more strongly filtered in the time domain before being processed into maps.

2.2. *Map Making*

A series of operations are performed to convert the raw data from the field observations to calibrated maps. The map-making process in this work is almost identical to that in R13; the most significant change lies in the treatment of the RA5H30DEC−55 and RA23H30DEC−55 fields. These two fields, originally observed in 2008, were re-observed in 2010 (RA23H30DEC−55) or 2011 (RA5H30DEC−55) in order to add coverage at 95 GHz (the array fielded in 2008 did not have enough high-quality 95 GHz detectors to produce survey-depth data). These additional observations also resulted in deeper final maps at 150 GHz (see Table 1). For these two fields, R13 analyzed the 150 GHz maps described in Vanderlinde et al. (2010). The filtering and calibration for these two fields were treated differently from the other fields. In this analysis we use the full, two-season data (including the 95 GHz data), and the treatment of filtering and calibration is uniform across the survey.

We briefly summarize the map-making process here; these steps are described in detail in Schaffer et al. (2011).

- For each observation, time-ordered detector data are first notch-filtered to remove sensitivity to the pulse-tube cooler of the cryostat housing the SPT-SZ receiver. Which detectors' data to include in mapmaking is then determined using a series of cuts based upon noise performance and response to both a chopped thermal source and on-sky sources. Following these cuts the array is "flat-fielded" by adjusting each detector's data according to its re-

[2] Fields are named via the R.A. and declination of their centers.

TABLE 1
The fields observed by the South Pole Telescope between 2008 and 2011

Name	R.A. (°)	δ (°)	Area (deg^2)	σ_{95} (μK-arcmin)	σ_{150} (μK-arcmin)	σ_{220} (μK-arcmin)	Survey Year
RA5H30DEC−55	82.7	−55.0	82.9	38.2	12.8	37.0	2008,2011
RA23H30DEC−55	352.5	−55.0	100.2	36.9	11.7	35.0	2008,2010
RA21HDEC−60	315.0	−60.0	147.6	35.5	15.0	58.1	2009
RA3H30DEC−60	52.5	−60.0	222.6	35.7	15.7	59.0	2009
RA21HDEC−50	315.0	−50.0	190.0	40.7	17.7	65.7	2009
RA4H10DEC−50	62.5	−50.0	155.5	30.9	14.4	59.5	2010
RA0H50DEC−50	12.5	−50.0	156.2	36.8	16.1	64.2	2010
RA2H30DEC−50	37.5	−50.0	155.7	35.1	15.2	58.5	2010
RA1HDEC−60	15.0	−60.0	145.9	34.6	15.6	60.1	2010
RA5H30DEC−45	82.5	−45.0	102.7	39.1	17.7	72.7	2010
RA6H30DEC−55	97.5	−55.0	83.3	35.6	15.7	65.2	2011
RA3H30DEC−42.5	52.5	−42.5	166.8	34.0	15.4	62.4	2011
RA23HDEC−62.5	345.0	−62.5	70.5	35.9	15.8	62.2	2011
RA21HDEC−42.5	315.0	−42.5	111.2	36.7	16.5	67.0	2011
RA1HDEC−42.5	15.0	−42.5	108.6	35.4	15.3	62.9	2011
RA22H30DEC−55	337.5	−55.0	83.6	37.3	16.3	67.2	2011
RA23HDEC−45	345.0	−45.0	204.5	35.0	15.6	64.4	2011
RA6H30DEC−45	97.5	−45.0	102.8	35.8	15.6	67.0	2011
RA6HDEC−62.5	90.0	−62.5	68.7	34.9	15.9	67.9	2011

Note. — Descriptive information for the 19 fields that comprise the 2500 deg^2 SPT-SZ survey. Here we list the field name, center, effective area following point source masking, noise levels at 95, 150, and 220 GHz, and the year the field was imaged. The noise levels are estimated as in Schaffer et al. (2011), using the Gaussian beam approximation.

sponse relative to other detectors of the same frequency.

- In every scan across the field, each detector's data is high-pass filtered by removing the best-fit Legendre polynomial (with the polynomial order depending on the length of the scan) and a series of sine and cosine modes. The resulting filter has an effective cutoff frequency corresponding to angular multipole $l = 400$ (roughly 1/2 degree scales) in the scan direction. This filtering step removes large-scale noise from the atmosphere and low-frequency noise from the readout. To further reduce atmospheric contamination, the mean signal from detectors in a single wedge[3] is subtracted from the data of all detectors in that wedge. This common-mode subtraction acts as an isotropic high-pass filter with a cutoff at approximately $l = 500$. Bright point sources detected at $> 5\sigma$ (~ 6 mJy at nominal survey depth) in 150 GHz data are masked in both of these filtering steps.

- Following filtering, the telescope pointing model is used to project the data onto two-dimensional maps. For this analysis we use the Sanson-Flamsteed projection (Calabretta & Greisen 2002) in which pixel rows in the map correspond to constant elevation. As (for the majority of observations) the telescope also scans at constant elevation, this projection simplifies the characterization of the applied filtering at the cost of slight shape distortions at the map edges.

- Individual maps, weighted by their noise properties at $1500 < l < 4500$, are then coadded to produce the final maps. Maps with anomalously high or low weights or noise are not included in the coadd.

- A calibration factor based on observations of the galactic HII region RCW38 is applied to provide the absolute temperature calibration for the maps (Staniszewski et al. 2009). We have repeated the cluster-finding procedure described in §3 using maps with a CMB-based calibration and find negligible differences in the detection significances of galaxy clusters.

[3] The modular SPT-SZ receiver consists of 6 independent sub-arrays or "wedges" of 160 bolometers that operate at a single frequency.

3. CLUSTER EXTRACTION AND MM-WAVE CHARACTERIZATION

In this section, we provide a summary of the process by which galaxy cluster candidates are identified and characterized in the SPT survey data. This procedure is almost identical to that used in recent SPT publications; readers are referred to Williamson et al. (2011) and R13 in particular for more details. The small differences between R13 and this analysis are discussed in §6.3.

3.1. *Cluster Extraction*

As described in §2, the SPT-SZ survey fields are observed at 3 frequency bands centered at approximately 95, 150 and 220 GHz. These maps contain signal from a range of astrophysical sources. For the purposes of this analysis, we characterize the observed temperature, T, in the maps at frequency ν_i and location $\mathbf{x}$ by:

$$T(\mathbf{x}, \nu_i) = B(\mathbf{x}, \nu_i) * [f_{\rm SZ}(\nu_i) T_{\rm CMB} y_{\rm SZ}(\mathbf{x}) + n_{\rm astro}(\mathbf{x}, \nu_i)] + n_{\rm noise}(\mathbf{x}, \nu_i). \quad (3)$$

Here B encompasses the effects of the beam and applied filtering; the expected thermal SZ signal is given by the product of the frequency dependent term $f_{\rm SZ}$, the CMB temperature $T_{\rm CMB}$, and the Compton-y parameter $y_{\rm SZ}$;

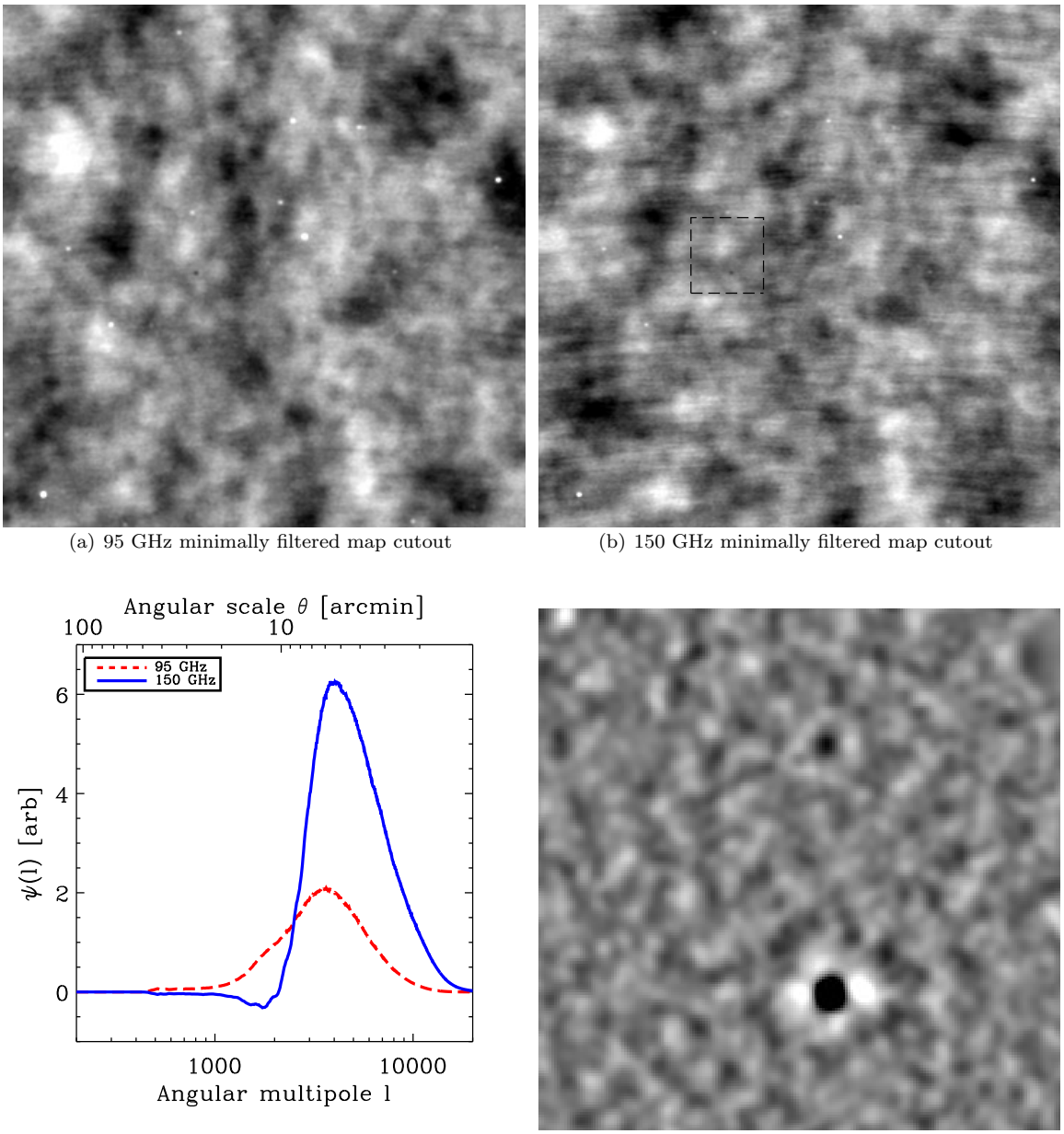

(a) 95 GHz minimally filtered map cutout

(b) 150 GHz minimally filtered map cutout

(c) Azimuthally averaged cluster-matched two-band filter

(d) Cluster-filtered map, zoomed in to 1°-by-1°

FIG. 1.— Visual representation of the SPT-SZ data and matched filtering process described in §2 and §3. Panels (a) and (b) show 6°-by-6° cutouts of 95 and 150 GHz maps from the RA21HDEC−60 field; the displayed temperature range is $\pm 300\mu K$. These maps are made from data that have been only minimally filtered (scan-direction high-pass filter at $l{\sim}50$) and show the main features of SPT-SZ survey data: large-scale primary CMB fluctuations, emissive point sources, and SZ decrements from galaxy clusters. Panel (c) shows the azimuthally averaged spatial-spectral filter optimized for detection of $\theta_c = 0\farcm25$ clusters, with the red-dashed (blue-solid) curves showing the Fourier-domain coefficients for the 95 (150) GHz data. Panel (d) shows a zoomed-in view of the 1°-by-1° area delineated by the dashed box in panel (b) after the spatial-spectral filter has been applied. This map is in units of signal-to-noise, and the displayed range is $-5 < S/N < 5$. Visible in this panel are the $\xi = 22.2$, $z = 1.132$ cluster SPT-CL J2106−5844 and the $\xi = 4.6$, optically unconfirmed candidate SPT-CL J2106−5820.

$n_{\rm astro}$ encompasses astrophysical signals—all of which are modeled here as Gaussian noise—and $n_{\rm noise}$ corresponds to instrumental and residual atmospheric noise not removed by the filtering discussed in §2. For SPT maps, $n_{\rm astro}$ primarily consists of lensed primary CMB fluctuations, kinetic and thermal SZ from the clusters below the SPT detection threshold, and dusty extragalactic sources; radio sources below the SPT detection threshold contribute negligibly to the maps. As in previous work, we model these noise terms based upon recent SPT power spectrum constraints (Keisler et al. 2011; Shirokoff et al. 2011).

Given the known spatial and spectral characteristics of galaxy clusters as well as the sources of noise in the maps, we construct a filter designed to maximize our sensitivity to galaxy clusters (Melin et al. 2006). This

Fourier-domain filter takes the form:

$$\boldsymbol{\psi}(\mathbf{l},\nu_i) = \sigma_\psi^{-2} \sum_j \mathbf{N}_{ij}^{-1}(\mathbf{l}) f_{\rm SZ}(\nu_j) S_{\rm filt}(\mathbf{l},\nu_j), \quad (4)$$

where the predicted variance in the filtered map, σ_ψ^{-2}, is given by

$$\sigma_\psi^{-2} = \int d^2l \sum_{i,j} f_{\rm SZ}(\nu_i) S_{\rm filt}(\mathbf{l},\nu_i)\ \mathbf{N}_{ij}^{-1}(\mathbf{l}) \times f_{\rm SZ}(\nu_j) S_{\rm filt}(\mathbf{l},\nu_j), \quad (5)$$

$\mathbf{N}$ is the Fourier-domain version of the band-band, pixel-pixel covariance matrix, and $S_{\rm filt}$ is the Fourier transform of the real space cluster template convolved with $B(\mathbf{x},\nu_i)$. We use a projected isothermal β-model (Cavaliere & Fusco-Femiano 1976) with β fixed to 1 as our source template:

$$\Delta T = \Delta T_0 (1+\theta^2/\theta_{\rm c}^2)^{-1} \quad (6)$$

where ΔT_0 is the normalization, θ is the angular separation from the cluster center, and $\theta_{\rm c}$ is the core radius. As discussed in Vanderlinde et al. (2010), given the spatial resolution of the SPT this simple profile is adequate for our purposes: no improvement in the detection of clusters is seen using more sophisticated models (e.g., Nagai et al. 2007, Arnaud et al. 2010).

A series of profiles with evenly-spaced core radii ranging from $0\farcm25$ to $3'$ is used to construct 12 matched filters. Azimuthal averages of the $0\farcm25$ matched-filter coefficients for 95 and 150 GHz are shown as a function of ℓ in the bottom left panel of Figure 1. After the application of these filters to the 95 and 150 GHz maps (the relative noise levels in the 220 GHz maps are too high to significantly improve cluster detection, so these data are omitted here), cluster candidates are extracted via a peak detection algorithm similar to the `SExtractor` routine (Bertin & Arnouts 1996). We record the location and maximum detection significance across all filter scales, ξ, for all cluster candidates with $\xi \geq 4.5$. The bottom-right panel of Figure 1 shows the result of applying the $0\farcm25$ matched filter to 95 and 150 GHz maps of the RA21HDEC−60 field.

We take two steps to reduce the number of spurious sources created by filter artifacts (in particular decrements created by the filter "ringing" around strong sources). First, prior to filtering the maps we mask a $4'$ region around all point sources detected above 5σ in 150 GHz maps optimized for point source detection. Following filtering we additionally exclude cluster candidates detected within $8'$ of these emissive sources. This step removes 163 deg^2 from the survey. We perform a separate cluster-finding analysis on these masked regions and report on those detections (which we do not include in the official catalog) in §6.2. We also find it necessary to veto candidates around the strongest cluster detections: we exclude candidates within a $10'$ region around $\xi > 20$ detections. This final cut removes less than 1 deg^2 from the entire survey.

3.2. *Integrated Comptonization*

For every cluster candidate we measure the integrated Comptonization, $Y_{\rm SZ}$, within a $0\farcm75$ radius aperture. For a projected isothermal β-model, $Y_{\rm SZ}$ is defined as:

$$Y_{\rm SZ}^{0\farcm75} = 2\pi \int_0^{0\farcm75} y_0 (1+\theta^2/\theta_{\rm c}^2)^{-1} \theta d\theta \quad (7)$$

where y_0 is the peak Comptonization. The aperture is slightly smaller than the $1'$ radius utilized in R13: as demonstrated in Saliwanchik et al. (2013), at the resolution and noise levels of the SPT-SZ survey, the scatter of $Y_{\rm SZ}$ at fixed cluster mass is minimized at $\theta = 0\farcm75$. This scatter, measured to be $27 \pm 2\%$, is comparable to the scatter in the relation between SPT detection significance and mass that is used to estimate cluster masses in R13 and other SPT cluster publications.

$Y_{\rm SZ}$ is computed using the same procedure as in R13. Briefly, for every cluster candidate, the likelihood of the observed two-band SZ signal given the model of Eqn. 6 is estimated using a simple gridded parameter search. For every point in the four-parameter space of y_0, $\theta_{\rm c}$, x position, and y position, the value of $Y_{\rm SZ}^{0\farcm75}$ is calculated using Eqn. 7, and the best-fit value and 1σ constraints are estimated from the (one-dimensional) $Y_{\rm SZ}^{0\farcm75}$ posterior distribution. Effective step-function priors are placed on the values of $\theta_{\rm c}$, x, and y by restricting the parameter grid for each cluster such that x and y are within $1\farcm5$ of the best matched-filter position for that cluster (we note that the absolute difference between the best-fit and matched-filter positions is $< 0\farcm75$ for 97% of the cluster candidates) and that the physical core radius of each cluster is 50 kpc $\leq r_{\rm core} \leq$ 1 Mpc. For unconfirmed candidates we use a redshift of $z = 1.5$ to set the physical scale. The priors on $r_{\rm core}$ are motivated by the known mass distribution of SPT-selected clusters and the mass-concentration relation measured by, e.g., Mandelbaum et al. (2008).

3.3. *Contamination*

Simulations are used to estimate the level of contamination in the cluster catalog by false detections from instrumental noise and non-cluster astrophysical signals. The simulations are similar to those used in R13; we provide a brief summary here.

For each of the 19 SPT fields we create 100 simulated sky maps composed of contributions from the CMB, emissive sources, and noise (note that we do not include a thermal SZ contribution when quantifying the expected number of false detections). The CMB component is modeled as a Gaussian random field based on the best-fit WMAP7 + SPT lensed ΛCDM model (Komatsu et al. 2011; Keisler et al. 2011), and the point source model contains contributions from radio sources and dusty star-forming galaxies (DSFG): all source contributions are modeled as Gaussian fields. The simulated radio population follows the results of De Zotti et al. (2005), Vieira et al. (2010), and Reichardt et al. (2012). We assume 100% correlation between the bands, a spectral index of $\alpha = -0.53$ and, at 150 GHz, an amplitude of $D_l = l(l+1)C_l/2\pi = 1.28\ \mu$K^2 at $l = 3000$. The amplitudes and spectral indices of the DSFG contributions are also constrained by recent SPT measurements (Reichardt et al. 2012). At 150 GHz and $l = 3000$ the Poisson contribution has amplitude $D_l = 7.54\ \mu$K^2 and the clustered contribution $D_l = 6.25\ \mu$K^2; we use $\alpha = 3.6$ for

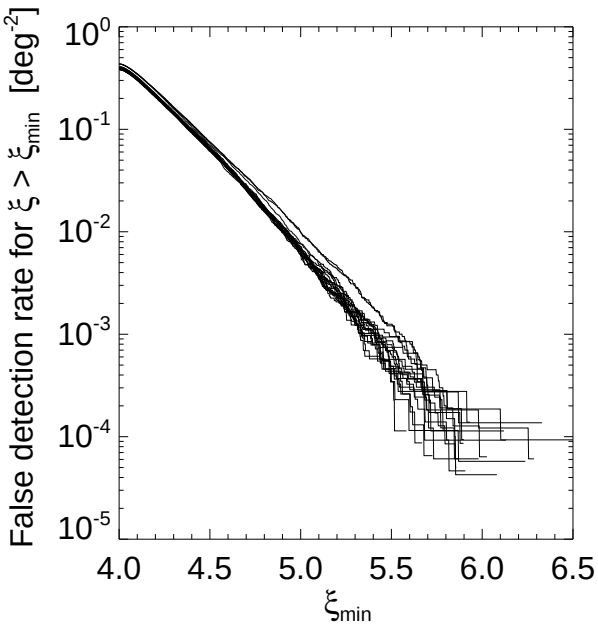

FIG. 2.— Simulated false-detection rate for each of the 19 fields in the SPT-SZ survey. Plotted is the cumulative density of false detections above a detection significance, $\xi_{\rm min}$. We expect 18.5 false detections at $\xi \geq 5$ and 172 at $\xi \geq 4.5$ for the entire survey.

both contributions. For each simulated map, we create noise realizations using jackknife noise maps (e.g., Sayers et al. 2009). The noise maps are created by randomly multiplying half of the observations of a field by -1 and then coadding the entire set of observations. This is a change from the R13 simulations which assumed stationary Gaussian noise.

To estimate the expected number of false detections, the cluster-detection algorithm is run (with point source masks and apodization matching the real data) on these cluster-free simulated maps. In Figure 2 we plot the expected rate of false detections in each individual SPT field. Two fields have slightly higher false-detection rates owing to the inclusion of boundary regions with uneven coverage in the area searched for clusters. In total, across all fields, we expect 172 false detections at $\xi > 4.5$ and 18.5 at $\xi > 5$. We return to the question of false detections again in §6 where we compare our expectations to the measured purity of the cluster sample.

4. FOLLOW-UP OBSERVATIONS

We use optical and in some cases NIR imaging to confirm candidates as clusters and to obtain redshifts for confirmed systems. In this section, we briefly describe our follow-up strategy and the reduction of imaging data. Follow-up imaging was obtained for all 477 candidates detected above $\xi = 4.8$ and 172 of the remaining 200 candidates down to $\xi = 4.5$. The procedures discussed here closely follow those presented in Song et al. (2012, hereafter S12).

4.1. *Follow-up Strategy*

Our candidate follow-up strategy evolved over the course of the SPT-SZ survey. Initially, clusters were confirmed using preexisting imaging from the Blanco Cosmology Survey (BCS; Desai et al. 2012, see §4.3) as well as targeted imaging on the Blanco/MOSAIC-II[4] and Magellan/IMACS imagers (Dressler et al. 2006) (see High et al. 2010 for more details). As the candidate sample size grew, we adjusted our imaging strategy to effectively incorporate a range of small- and large-aperture telescopes. Our resulting strategy is as follows:

- All cluster candidates are "pre-screened" using imaging data from the Digitized Sky Survey (DSS)[5] to determine if a cluster candidate lies at low redshift. We find the DSS images are generally sufficient to allow identification of the optical counterparts of SPT clusters out to redshift $z = 0.5$, with a tail extending to $z = 0.7$. Roughly 50% of confirmed SPT clusters are identifiable in DSS data; candidates not apparent in the DSS are classified as high-redshift targets.

- We observe potential low-redshift candidates at 1 m – 2 m class facilities. If the candidate is not confirmed in these data, it is reclassified as a potential high-redshift system.

- High-redshift targets are imaged on larger aperture (4 m – 6.5 m) telescopes. The majority of these cluster candidates with $\xi \geq 4.8$ and many candidates with $4.5 \leq \xi < 4.8$ have also been imaged in the NIR from ground- or space-based facilities. This threshold was $\xi = 4.5$ in S12; the increased threshold here is due to limited NIR resources.

- Following the release of the Wide-field Infrared Survey Explorer (WISE) all-sky catalogs (Wright et al. 2010), observations of $\xi < 4.8$ candidates were weighted towards those candidates with lower values of the NIR "blank-field" statistic presented in S12. This statistic quantifies the significance of any overdensity of galaxies at the candidate's location compared to random fields; lower values correspond to more dense regions. As such, the follow-up of these lower significance candidates is biased to maximize the number of confirmed clusters.

In Table 2 we list the facilities and instruments used in our follow-up campaign. We assign each telescope/instrument combination a numerical alias which we use in Table 4 to identify the source of redshift information.

4.2. *Targeted Observations and Data Reduction*

4.2.1. *Optical Data*

Our strategy for targeted optical follow-up varied with the aperture of the follow-up telescope. In this section, we first describe our strategy for observing candidates we expect to be at low redshift with 1 m – 2 m class telescopes; we then move on to our strategy for observing likely high-redshift candidates with larger telescopes. Note that in this section we quote depths relative to the

[4] http://www.ctio.noao.edu/mosaic/

[5] The DSS is a digitization of the photographic sky survey conducted with the Palomar and UK Schmidt telescopes; http://archive.stsci.edu/dss/.

TABLE 2
Optical and infrared imagers

Ref.[a]	Site	Telescope	Aperture (m)	Camera	Filters[b]	Field
1	Cerro Tololo	Blanco	4	MOSAIC-II	$griz$	$36' \times 36'$
2	Las Campanas	Magellan/Baade	6.5	IMACS f/2	$griz$	$27\farcm4 \times 27\farcm4$
3[c]	Las Campanas	Magellan/Clay	6.5	LDSS3	$griz$	$8\farcm3$ diam. circle
4[d]	Las Campanas	Magellan/Clay	6.5	Megacam	gri	$25' \times 25'$
5	Las Campanas	Swope	1	SITe3	$BVRI$	$14\farcm8 \times 22\farcm8$
6	La Silla	MPG/ESO	2.2	WFI	$BVRI$	$34' \times 33'$
7	La Silla	New Technology Telescope	3.6	EFOSC2	$griz$	$4\farcm1 \times 4\farcm1$
8	Cerro Tololo	Blanco	4	NEWFIRM	K_s	$28' \times 28'$
9	Las Campanas	Magellan/Baade	6.5	FourStar	J, H, K_s	$10\farcm8 \times 10\farcm8$
10	Satellite	Spitzer Space Telescope	0.85	IRAC	3.6μm, 4.5μm	$5\farcm2 \times 5\farcm2$
···	Satellite	Wide-field Infrared Survey Explorer	0.40	···	$W1, W2$	$47' \times 47'$

Note. — Optical and infrared cameras used in SPT follow-up observations.
[a] Shorthand alias used in Table 4.
[b] Not all filters were used to image every cluster.
[c] http://www.lco.cl/telescopes-information/magellan/instruments/ldss-3
[d] Megacam data were acquired for a large follow-up weak-lensing program.

apparent magnitude of L* galaxies: our model for the redshift evolution of these galaxies is described in §5.

In order to rapidly image a large number of systems, we adopt a minimalist approach for low-redshift candidates observed on the 1 m Swope telescope. Based on an initial "by-eye" redshift estimate from the DSS screening step[6], we choose a pair of filters (BV,VR,RI) expected to straddle the 4000 Å break. Three filters are used when required to avoid redshift degeneracies. Candidates are imaged to depths sufficient for robust estimation of red-sequence redshifts: we require detection of 0.4L* red-sequence galaxies at 8σ in the redder filter and 5σ in the bluer filter. A second round of deeper imaging is obtained for systems with significantly underestimated DSS redshifts. Non-confirmed candidates and clusters at higher redshift ($z > 0.7$) are re-observed on larger class telescopes and/or with NIR imagers.

Low-redshift candidates are also observed on the MPG/ESO 2.2 m telescope using the Wield Field Imager (WFI; Baade et al. 1999). These observations are deeper than those acquired on Swope as they were designed to also enable studies of the galaxy populations of these clusters (e.g., Zenteno et al. 2011). Based on its preliminary DSS redshift, each candidate is imaged in three filters (BVR or VRI), to depths sufficient to detect 0.4L* galaxies at 10σ in the bands straddling the 4000 Å break. The third band is used for photometric calibration (see below). Second-pass imaging is obtained as necessary to adjust for imperfect initial redshift estimates. As with our Swope program, non-confirmed candidates and clusters at higher redshift ($z > 0.75$) are re-observed on larger class telescopes and/or with NIR imagers.

As described in S12, we also adopt a two-pass strategy for observations on 4 m–6.5 m class telescopes. Candidates are first imaged in the g-, r-, z-bands (or g-, r- and i-bands early in the follow-up campaign) to depths sufficient to detect 0.4L* galaxies at $z = 0.75$ at 5σ in the redder bands. The g-band data is used for photometric calibration. Following this first-pass imaging, all non-confirmed candidates at $\xi \geq 4.8$ (and a subsample of non-confirmed candidates below this threshold) were further imaged in the z- and i- (or r-) bands to extend this redshift range to $z = 0.9$ and/or were imaged in the NIR, as described below.

With the exception of images from Magellan/Megacam (McLeod et al. 2006), all optical images were reduced with the PHOTPIPE pipeline (Rest et al. 2005; Garg et al. 2007; Miknaitis et al. 2007). Megacam images were reduced using the Smithsonian Astrophysical Observatory Megacam reduction pipeline. The PHOTPIPE reduction process as applied to SPT clusters is explained in High et al. (2010) and the Megacam pipeline in High et al. (2012). All reductions include the standard CCD image processing steps of masking bad or saturated pixels, applying crosstalk and overscan corrections, debiasing, flat-fielding, correcting for scattered light via illumination corrections, and—where necessary in the redder bands—defringing. Cosmic rays are also removed from the Megacam images. Images are coadded using the `SWarp` algorithm (Bertin et al. 2002), and astrometry is tied to the Two Micron All Sky Survey (2MASS) catalog (Skrutskie et al. 2006).

Sources are detected using the `SExtractor` algorithm (v 2.8.6) in dual-image mode; we use the deepest images with respect to red-sequence galaxies as the detection images. As in previous works, photometry is calibrated using Stellar Locus Regression (SLR, High et al. 2009) with absolute calibration derived using stars in the 2MASS catalog.

There are a few modifications to the calibration process discussed in previous SPT publications. For clusters only imaged in two bands at Swope, we combine J-band data from 2MASS with the optical data to create the two colors required for calibration via SLR. The SLR calibration for candidates imaged on the NTT was somewhat challenging owing to the small field of view ($4\farcm1 \times 4\farcm1$) of the EFOSC2 imager (Buzzoni et al. 1984). These calibrations were performed with fewer stars than the other imaging; for a few fields we jointly calibrated the data with other observations from the same night. We in-

[6] These crude redshifts are based on a combination of the color, brightness, and angular size of identified cluster galaxies. The uncertainty on these estimates is $\sigma_z \sim 0.1$, with large outliers owing to variable DSS image quality.

crease the expected uncertainty on the color calibration for these systems to 5% (compared to the typical 2-3% observed with SLR, see High et al. 2009; Bleem et al. 2014) and include this extra scatter in our estimates of redshift uncertainties. Finally, for a small subset of clusters located in the wings of the Large Magellanic Cloud (LMC), we restrict our fitting to stars with counterparts in the 2MASS catalog to enable convergence of the regression algorithm.[7]

4.2.2. *Near-Infrared Data*

Spitzer/IRAC imaging (Fazio et al. 2004) at 3.6 μm and 4.5 μm is obtained for the majority of high-redshift SPT cluster candidates at $\xi \geq 4.8$ and a subsample of systems at $4.5 \leq \xi \leq 4.8$. In total 276 candidates (241 candidates at $\xi > 4.8$) were observed as part of our *Spitzer* follow-up program.[8] These *Spitzer* data play a crucial role in confirming and determining the redshift of clusters at $z > 0.8$. Candidates are imaged in 8×100 s and 6×30 s dithered exposures at 3.6 and 4.5 μm, respectively; the resulting coadded images are sufficient for the detection in the 3.6 μm band of $z = 1.5$ 0.4L* galaxies at 10σ. These observations are reduced following the methodology of Ashby et al. (2009). Briefly, these reductions correct for column pulldown, mosaic the individual exposures, resample the images to $0\farcs86$ pixels (half the solid angle of the native IRAC pixels), and reject cosmic rays.

Ground-based NIR imaging of some candidates was acquired with the NEWFIRM imager (Autry et al. 2003) at the CTIO 4 m Blanco telescope and the FourStar imager (Persson et al. 2013) on the Magellan Baade 6.5 m telescope. NEWFIRM data with a target 10σ point source depth of 19 Vega magnitudes in the K_s filter were obtained for 31 candidates during two runs in November 2010 and July 2011 under photometric conditions. Typical observations consisted of 16 point dither patterns, with 6×10 s exposures obtained at each dither position. The data were reduced using the `FATBOY` pipeline, originally developed for the FLAMINGOS-2 instrument, and modified to work with NEWFIRM data in support of the Infrared Bootes Imaging Survey (Gonzalez et al. 2010). Images were coadded using `SCAMP` and `SWarp` (Bertin et al. 2002) and photometry was calibrated to 2MASS.

Additional JHK_s-band imaging was collected with FourStar for 34 candidates during several runs in 2012, 2013, and 2014 in average to good conditions. Several exposures were taken at 9–15 different pointed positions with the coordinates of the cluster centered on either the mosaic or one of the four detectors. The images were flat-fielded using standard IRAF routines; WCS registering and stacking were done using the PHOTPIPE pipeline and were calibrated photometrically to 2MASS.

4.2.3. *Spectroscopic Observations*

We have also used a variety of facilities to obtain spectroscopic observations of SPT clusters. These observations fall into two categories: small, few-night programs focused primarily on the highest-redshift subset of the SPT-selected clusters (e.g., Brodwin et al. 2010; Foley et al. 2011; Stalder et al. 2013; Bayliss et al. 2013) and longer, multi-semester campaigns. The longer programs include observations of high-redshift systems using FORS2 on the VLT (Appenzeller et al. 1998) and a large survey program on the Gemini-South telescope (NOAO PID 2011A-0034) using GMOS-S (Hook et al. 2004) that targeted 85 SPT clusters in the redshift interval $0.3 < z < 0.8$. In Ruel et al. (2013) we describe in detail our spectroscopic followup campaign and report spectroscopic redshift measurements for 61 SPT clusters and velocity dispersions for 48 of these clusters. Here we report an additional 34 cluster redshifts using newly obtained data from the Gemini Survey Program. As described below in §6, we also search the literature for spectroscopic counterparts of SPT clusters; in total 141 of the clusters in this work have spectroscopically measured redshifts.

4.3. *Other Datasets*

In addition to dedicated optical/NIR observations of SPT cluster candidates, we use imaging from three surveys that overlap the SPT footprint: the BCS, the *Spitzer*-South Pole Telescope Deep Field (SSDF; Ashby et al. 2013), and the WISE all-sky survey. The BCS is a $\sim$80 deg^2 4-band (g,r,i,z) survey (NOAO large survey program 2005B-0043) with imaging sufficient for cluster confirmation to $z \sim 1$. It is composed of two fields roughly centered at (R.A.,DEC) = (23h,−55d) and (5h30m,−53d). These fields roughly overlap with the RA5H30DEC−55 and RA23H30DEC−55 fields, the first fields surveyed by the SPT (See Table 1). We use the reductions presented in Bleem et al. (2014) in this work.

The SSDF, a 94 deg^2 survey at 3.6 and 4.5 μm, is centered at (R.A.,DEC)= (23h30,−55d). It encompasses a large fraction of the RA23H30DEC−55 field. This survey, one of the largest extragalactic surveys ever conducted with *Spitzer*/IRAC, has imaging sufficient for cluster confirmation and redshift estimation to $z \gtrsim 1.5$.

The WISE all-sky survey provides catalogs and images of the entire sky in the W1-W4 bands (3.4–22 μm)[9]; the shorter-wavelength NIR data from WISE are sensitive to cluster galaxies out to $z \sim 1.3$ (Gettings et al. 2012; Stanford et al. 2014). As discussed in §4.1, we use WISE data to prioritize the follow-up of lower significance candidates.

5. CLUSTER CONFIRMATION & REDSHIFT ESTIMATION

As in previous SPT publications, we deem a candidate to be "confirmed" if we identify an excess of clustered red-sequence galaxies at the SPT location. In this section, we describe our model for the optical and NIR properties of red-sequence galaxies, the process by which we identify excesses of such galaxies at candidate locations, and the estimation of redshifts for confirmed clusters using optical and/or NIR data. Finally, for unconfirmed candidates, we describe our procedure for determining

[7] The stellar envelope of the LMC extends well beyond regions of significant thermal dust emission; we see no evidence of contamination in the SPT mm-wave maps.

[8] Archival observations with varying wavelength coverage and exposure times are available for an additional 16 (typically low-redshift) SPT systems.

[9] http://wise2.ipac.caltech.edu/docs/release/allsky/

the redshift to which our imaging is sufficient to confirm the candidate as a cluster.

5.1. *Red-Sequence Model*

We create our model for the color-magnitude relation of red-sequence galaxies using the `GALAXEV` package (Bruzual & Charlot 2003). We model the galaxies as passively evolving, instantaneous-burst stellar populations with a formation redshift of $z = 3$; the stellar populations are generated using the Salpeter initial mass function (Salpeter 1955) and follow the Padova 1994 evolutionary tracks (Fagotto et al. 1994). Metallicites are chosen based upon analytical fits to RCS2 cluster data (Koester, private comm.), and cubic splines are used to interpolate the discrete output of the code to arbitrary redshifts. We compare our stellar-synthesis $m^*(z)$ model to the Rykoff et al. (2012) model for the maxBCG cluster sample over the redshift range for which that model is valid ($0.05 < z < 0.35$). We find a small ($\sim$0.2 mag) offset, and we correct our model for this offset. Our red-sequence model is further calibrated to real data using the SPT spectroscopic subsample as described below.

5.2. *Identifying Red-Sequence Overdensities and Estimating Optical Redshifts*

For each cluster candidate, we search for a redshift at which there is a clear excess of galaxies near the candidate position that are consistent with the expected red sequence at that redshift. We typically search for overdensities out to $z \sim 0.7$ ($z \sim 1$) for systems with first-pass (second-pass) optical imaging. At a series of discrete redshifts in this range, we compute the background-subtracted, weighted red-sequence galaxy count in a $2'$ ($3'$ at $z < 0.3$) region around the SPT position. The contribution of each galaxy to the weighted sum is based upon the consistency of the galaxy's color and magnitude with the red-sequence model at the redshift in question.

To confirm a cluster, we require a significant peak in background-subtracted weighted counts. The preliminary redshift is identified as the location of this peak. In a few instances where this peak is marginally significant (for example, when the cluster is well-detected in one imaging band but poorly in the second owing to incomplete follow-up), we confirm clusters based solely on visual identification of member galaxies and manually select cluster galaxies for redshift estimation.

To further refine the preliminary redshift and to estimate a statistical uncertainty, we next bootstrap resample the galaxies that contribute to the peak. For each bootstrap sample, the estimated redshift is the redshift at which the χ^2 statistic:

$$\chi^2 = \sum_{\text{galaxies}} \frac{[\text{Model(magnitude, color, z)} - \mathbf{g}]^2}{\text{color error}^2 + \sigma_{\text{rs}}{}^2} \quad (8)$$

is minimized. Here $\mathbf{g}$ encodes the color and magnitude of the galaxies, and $\sigma_{rs} = 0.05$ (Koester et al. 2007; Mei et al. 2009) is the intrinsic spread of the red sequence. The reported redshift is the median redshift of 100 bootstrap resamples. The final redshift uncertainties are reported as the statistical error estimated from this bootstrap resampling process (typically small as most estimates are derived from tens of galaxies) added in quadrature with a redshift-dependent scatter determined during the spectroscopic tuning of the red-sequence model, which we now describe.

We first estimate "raw" redshifts using the uncalibrated red-sequence model for 103 clusters with good follow-up data and spectroscopic redshifts in the SPT sample. As follow-up observations span different instruments with different combinations of filters (e.g., subsets of *griz* on IMACS, LDSS3, Megacam, MOSAIC-II and EFOSC2 and *BVRI* on the SITe3 and WFI), we separately calibrate models for each color-magnitude combination used in this analysis. We also calibrate models for the Swope/SITe3 and MPG/ESO WFI data separately, as we have not transformed the natural Swope photometry to standard *BVRI* passbands. The large number of clusters with spectroscopic redshifts[10] enables these independent calibrations.

We find a linear remapping of model redshifts, z_{model}, to spectroscopic redshifts, z_{spec},

$$z_{\text{spec}} = A\ z_{\text{model}} + B \quad (9)$$

is sufficient for tuning the $g - r$ vs. i (or z) relation over the redshift range $z < 0.35$ as well as for tuning the Johnson color-magnitude combinations ($B - V$ vs. R, $V - R$ vs R, $R - I$ vs. R).

However, as noted in Bleem et al. (2014), we observe large residuals when applying such a first order correction over the broad redshift range sampled by the *r,i,z* filters. As we expect the remapping from raw to calibrated redshifts to be smoothly varying and monotonic, we use non-linear least squares minimization to fit the z_{model} and z_{spec} relation to a monotonic function. This function is generated using the methodology of Ramsay (1998) where we have chosen sines and cosines as the basis functions and include these functions to the 4th order. As in S12, we estimate the uncertainty in our model calibration by determining the quantity σ_z such that the reduced chi-squared statistic, χ^2_{red} :

$$\chi^2_{\text{red}} = \frac{1}{\nu} \sum \frac{(z_{\text{est}} - z_{\text{spec}})^2}{(\delta_z(1+z))^2} = 1 \quad (10)$$

where z_{est} is our calibrated redshift and ν is the number of degrees of freedom. Here the total degrees of freedom are reduced by 2 by the linear rescaling and by 10 for higher order rescaling. We find $\delta_z \sim$0.025 for Swope/SITe3 , $\delta_z \sim$0.021 for WFI and $\delta_z \sim$0.013 – 0.018 for the *griz*-based redshift models. We plot the results of the redshift tuning in Figure 3.

5.3. *Near-Infrared Redshifts*

We analyze the NIR data as in "Method 1" from S12 (see §3.1 in that work) by supplementing the optical with the JHK_s and IRAC imaging. The IRAC imaging is only used in the cases where the optical imaging is not deep enough to confirm a cluster and measure the redshift. The JHK_s data are used as additional filters to measure at least one color across the 4000Å break. It

[10] Spectroscopic redshifts were measured or identified from the literature for 24 clusters observed with the MPG/ESO telescope, 56 clusters imaged with the Swope telescope, and 100 clusters observed with the larger aperture telescopes. Some clusters with spectroscopic redshifts were observed with multiple instruments to facilitate calibration of red-sequence models.

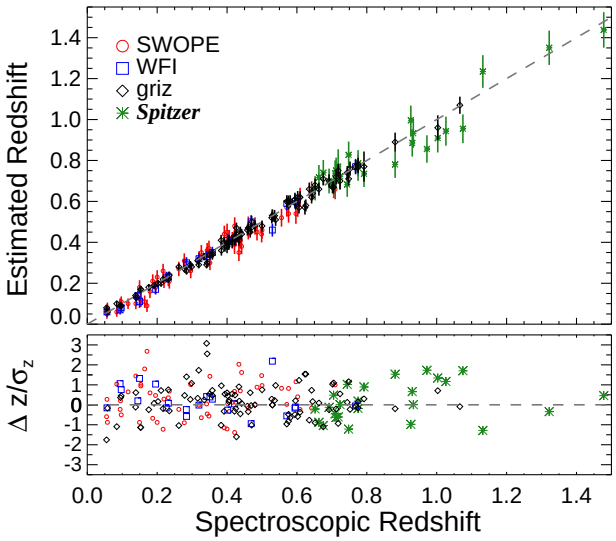

FIG. 3.— Results of red-sequence model calibration. (Top) Photometric redshift, $z_{\rm est}$, versus spectroscopic redshift, $z_{\rm spec}$, for 129 spectroscopically confirmed SPT clusters. We plot the aggregate model tunings for Swope/SITe3, MPG/ESO WFI, the larger class telescopes (for which the model was calibrated across instruments as all clusters were observed in the *griz* system), and *Spitzer*/IRAC. Some clusters are plotted multiple times (at most once per model) as they were observed with multiple telescopes to calibrate the various redshift models. (Bottom) Distribution of redshift residuals $\Delta z/\sigma_z = (z_{\rm spec} - z_{\rm est})/\sigma_{z_{\rm est}}$. The typical redshift uncertainty, σ_z, scales as $\sim 0.013 - 0.018(1+z)$ for redshifts estimated using combinations of *griz* filters, $\sim 0.021(1+z)$ for clusters imaged with the MPG/ESO WFI, $\sim 0.025(1+z)$ for Swope/SITe3, and as $\sim 0.035(1+z)$ for redshifts determined using *Spitzer*/IRAC.

should be noted that the *Spitzer*-only $[3.6]-[4.5]$ colors are probing near the peak in the stellar emission, rather than the Balmer break; as such, they are less sensitive to the effects of recent star formation or AGN activity which may be more prevalent at high redshift (Brodwin et al. 2013). We have demonstrated with spectroscopic follow-up that this measurement is reliable in the redshift range relevant for confirmation of high-z clusters (Stalder et al. 2013; Bayliss et al. 2013, and see Figure 3). There are three clusters with [3.6]–[4.5] galaxy colors consistent with redshifts greater than 1.5; as our models have not been tested with spectroscopic data in this redshift range, we report a lower limit of $z = 1.5$ for the redshifts of these systems (see Figure 4).

5.4. *Redshift limits*

As all of our optical/NIR observations have finite depth, it is not possible to definitively rule out the existence of undiscovered, high-redshift counterparts for our unconfirmed cluster candidates. We instead report for each unconfirmed candidate the highest redshift for which we would have detected the overdensity of red galaxies we require to confirm a cluster. The depth of our follow-up imaging varies among candidates, so this limit is computed individually for each candidate. For every candidate, we determine the redshift for which a $0.4L_*$ red-sequence galaxy matches the measured 10σ magnitude limit of the imaging data. As we require two filters to measure a redshift, we obtain the "redshift limit" from the second deepest of the imaging bands used in the red-sequence overdensity search. A detailed description of this procedure is provided in S12.

6. CLUSTER CATALOG

In Table 4 we present the complete sample of galaxy cluster candidates detected at $\xi \geq 4.5$ in the 2500 deg^2 SPT-SZ survey. For each candidate we provide the position, integrated Comptonization within an $0\farcm75$-radius aperture (§3.2), the candidate detection significance ξ at the filter scale that maximizes detection significance, the value of the β-model core radius θ_c at which ξ is reported, the estimated mass and redshift (spectroscopic where available) for confirmed clusters and redshift limit for unconfirmed candidates. We discuss the estimation of these cluster masses in §6.1. In Figure 5 we plot the SZ detection significance versus redshift for each confirmed cluster as well as the redshift distribution of the confirmed cluster sample.

Simulations predict that this catalog should contain only a small number of false detections (see §3.3 for details of the simulations), and this prediction is borne out by our optical/NIR follow-up observations (§4). Our simulations predict 18.5 false detections above $\xi = 5$ for the full survey—corresponding to a predicted purity of 95% for the 402 $\xi \geq 5$ candidates in our catalog—and 172 false detections in the full $\xi \geq 4.5$ sample—corresponding to a predicted purity of 75% for the full sample of 677 cluster candidates. Under the assumption that there are no false associations between the identified optical/NIR galaxy overdensities and SPT detections (we estimate that $< 4\%$ of candidates will have such a false association—see discussion in §4.2 in S12), the measured cumulative purity of the sample is in excellent agreement with simulations: the purity is $\geq$95% at $\xi \geq 5$ and $\geq$76% for the entire sample at $\xi \geq 4.5$. Here we quote the purity as a lower limit, as unconfirmed candidates may be clusters at redshifts too high to be confirmed with our follow-up imaging (and some lower-significance candidates have not yet been imaged).

The SPT-SZ cluster sample contains massive galaxy clusters over a wide redshift range. The median mass of the sample is $M_{500c} \sim 3.5 \times 10^{14}\, M_\odot\, h_{70}^{-1}$, and the median redshift is $z = 0.55$. The sample extends from $0.047 \leq z \lesssim 1.7$, and the mass threshold of the catalog is nearly independent of redshift (see Figure 6). This implies that the catalog reported here contains all of the most massive clusters in the $\sim$1/16th of the sky imaged by the SPT.

In Figure 7, we show the estimated selection function of the cluster sample in three redshift bins. Because ξ is the selection variable, the selection function can simply be written as the Heaviside step function $\Theta(\xi - 4.5)$. Given the ξ-M relation discussed in §6.1, we transform this function to mass space, where it represents the probability of a cluster of a given mass to be included in the SPT-SZ sample. Note that at $M_{500c} > 7 \times 10^{14}\ h_{70}^{-1}\ M_\odot$ and $z > 0.25$, the SPT-SZ cluster catalog presented in this work is highly complete, meaning that nearly every such cluster in the surveyed area is present in the catalog. In Figure 6, we compare the mass and redshift distribution of the SPT sample to those from other large cluster catalogs selected via their ICM observables: namely the clusters detected in the all-sky *ROSAT* survey (Piffaretti et al. 2011), which includes the NORAS (Böhringer et al. 2000), REFLEX (Böhringer et al. 2004), and MACS (Ebeling et al. 2001) cluster catalogs; the

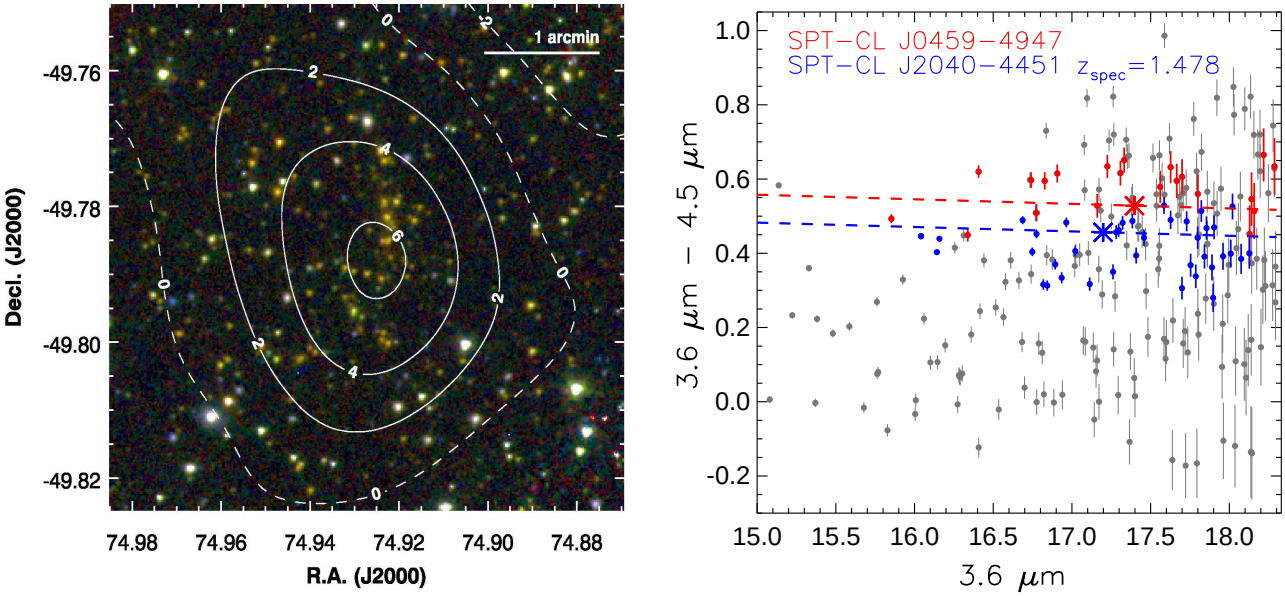

FIG. 4.— (Left) SPT-CL J0459−4947, one of three SPT clusters with an estimated redshift of $z > 1.5$ (*rgb*: *Spitzer*/IRAC 4.5, 3.6 μm, Magellan/IMACS z-band; over-plotted are the contours of the SZ detection). (Right) *Spitzer* color-magnitude diagram (with magnitudes relative to Vega): plotted in gray are all galaxies in the *Spitzer* field, over-plotted in red are the galaxies identified with the SZ detection. The galaxies of this massive system ($M_{500c} \sim 3 \times 10^{14} M_{\odot} h_{70}^{-1}$) have significantly redder *Spitzer* colors than spectroscopically confirmed SPT-CL J2040−4451 at $z = 1.478$ (blue), supporting that its redshift is greater than $z = 1.5$. The color-magnitude relations of the best-fit model redshifts are over-plotted as dashed lines and the locations of model L* galaxies are indicated via "∗". The best-fit redshift is $z = 1.7 \pm 0.2$, but the model is poorly calibrated at such high redshifts.

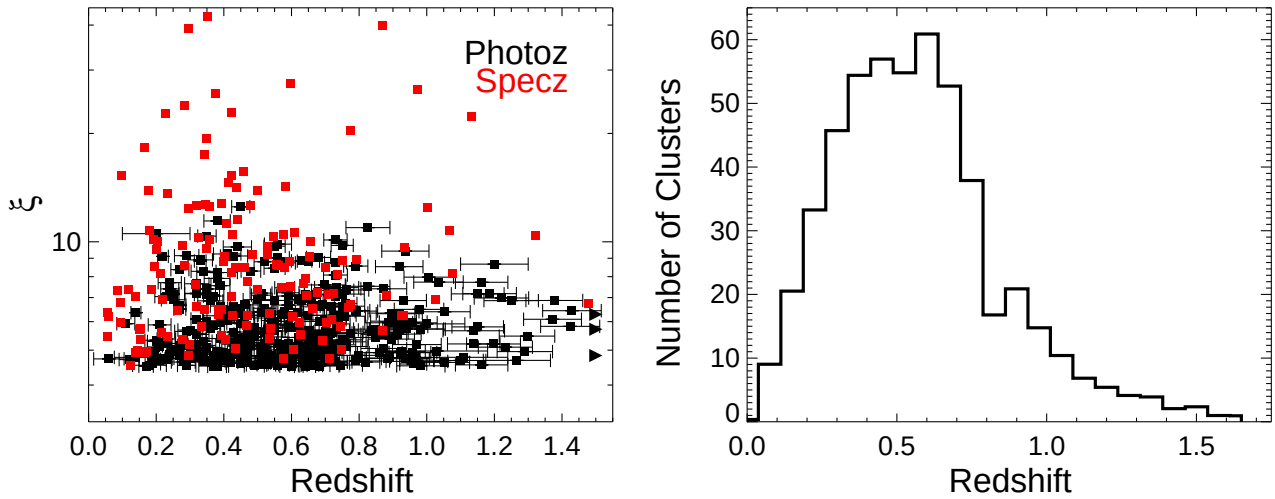

FIG. 5.— (Left) Plot of maximum detection significance, ξ, versus redshift for the confirmed SPT-SZ cluster sample; black points correspond to systems with photometrically estimated redshifts while red points represent spectroscopically confirmed clusters. We report lower limits for the redshifts of the three highest-redshift systems (see §5.3). (Right) The redshift distribution of the confirmed cluster sample; the median redshift of the sample is $z = 0.55$. The histogram does not have integer values as clusters with photometric redshift uncertainties were distributed amongst the appropriate bins.

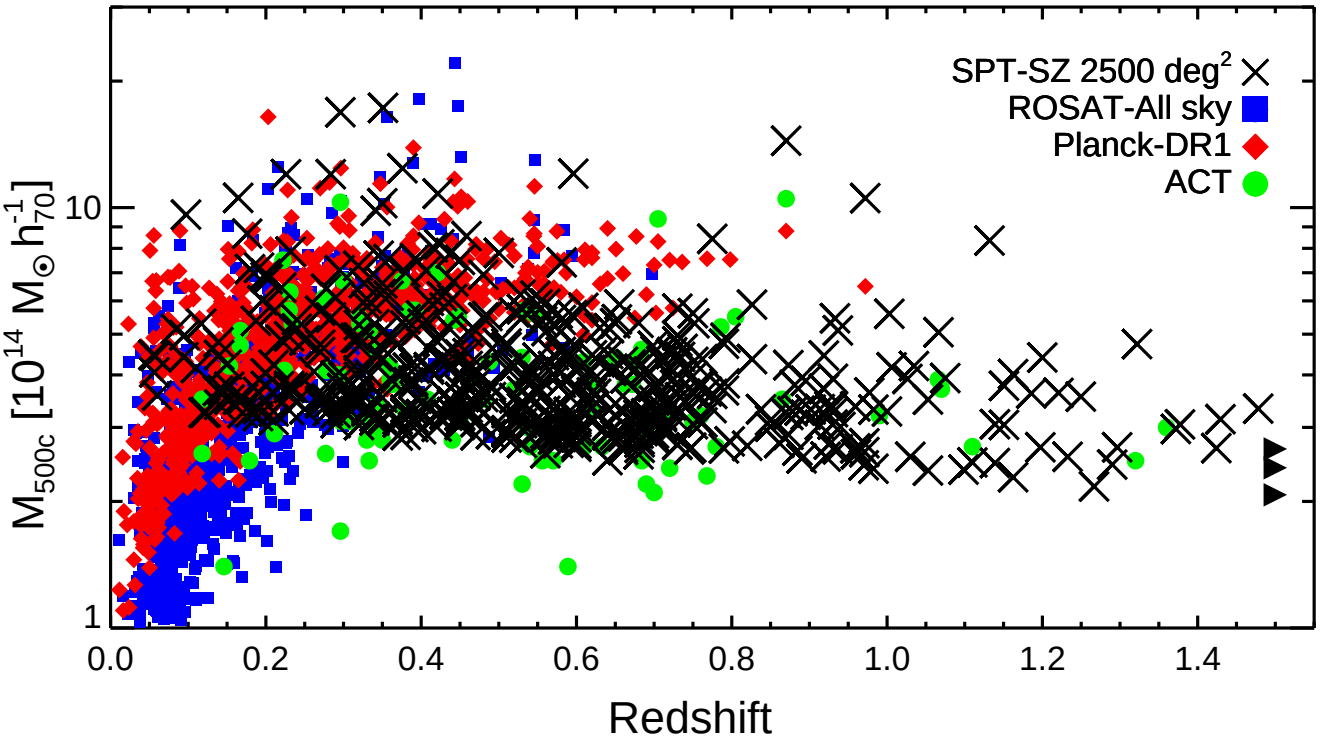

FIG. 6.— Comparison of the 2500 deg^2 SPT-SZ cluster catalog to other X-ray and SZ-selected cluster samples. Here we plot the estimated mass versus redshift for the 516 optically confirmed clusters from the SPT catalog, 91 clusters from the ACT survey (Marriage et al. 2011; Hasselfield et al. 2013), 809 SZ-selected clusters from the *Planck* survey (Planck Collaboration et al. 2013a), and 740 X-ray clusters selected from the *ROSAT* all-sky survey (Piffaretti et al. 2011) with $M_{500c} \geq 1 \times 10^{14}\ h_{70}^{-1}\ M_\odot$. We mark as lower limits the redshifts of the three high-redshift SPT systems for which the *Spitzer* redshift model is poorly constrained (black triangles). We plot clusters in common between the datasets (see e.g., Table 5) multiple times, using the masses and redshifts reported for each catalog. While the SPT data provides a nearly mass-limited sample, the cluster samples selected from *ROSAT* and *Planck* data are redshift-dependent owing to cosmological dimming of X-ray emission and the dilution of the SZ signal by the large *Planck* beams, respectively.

861 confirmed clusters from the all-sky *Planck* survey (Planck Collaboration et al. 2013a); and the 91 clusters that comprise the ACT cluster sample (Marriage et al. 2011; Hasselfield et al. 2013).

The mass threshold of the SPT sample declines slightly as a function of redshift owing to a combination of effects. At low redshifts ($z < 0.3$), increased power at large angular scales from primary CMB fluctuations and atmospheric noise raises the mass threshold for a fixed ξ cutoff (see e.g., Vanderlinde et al. 2010), while at higher redshifts the detectability of clusters is enhanced owing to increased temperatures for clusters of fixed mass. However, both of these trends are shallow, and the nearly redshift-independent selection function of the SPT catalog stands in contrast to the strong redshift dependence in X-ray catalogs and the *Planck* sample. The mass threshold for X-ray catalogs is redshift-dependent owing to cosmological dimming of the X-ray emission, while the redshift dependence of the *Planck* sample is driven by the dilution of the small angular-scale signal of high-redshift clusters by the large *Planck* beam ($7'$ at 143 GHz).

We search the literature for counterparts to SPT candidates. We query the SIMBAD[11] and NED[12] databases as well as the union catalog of SZ sources detected by *Planck* (Planck Collaboration et al. 2013a) for counterparts. For confirmed clusters with $z \leq 0.3$ we utilize a $5'$ association radius; otherwise we match candidates within a $2'$ radius. All matches are listed in Table 5; we discuss potential false associations in the footnotes of this table. Additionally, we associate the brightest cluster galaxies in two clusters (SPT-CL J0249−5658 and SPT-CL J2254−5805) with spectroscopic galaxies from the 2dF Galaxy Redshift Survey (Colless et al. 2003) and the 6dF Galaxy Survey (Jones et al. 2009), respectively. In total, 115 of the SPT candidates are found to have counterparts in the literature (14 of these clusters were first discovered in SPT data). We report the new discovery of 251 clusters here, increasing the number of clusters first discovered in SPT data to 415. We highlight particularly noteworthy systems below, and a subset of the SPT cluster catalog is shown in Figure 8.

6.1. *Cluster Mass Estimates*

We provide estimated masses for all confirmed clusters in Table 4. These estimates, determined from each cluster's ξ and redshift, are based upon the methodology presented in Benson et al. (2013) and R13 but are reported here for a fixed flat ΛCDM cosmology—with $\sigma_8 = 0.80$, $\Omega_b = 0.046$, $\Omega_m = 0.30$, $h = 0.70$, $\tau = 0.089$,

[11] http://simbad.u-strasbg.fr/simbad
[12] http://nedwww.ipac.caltech.edu/

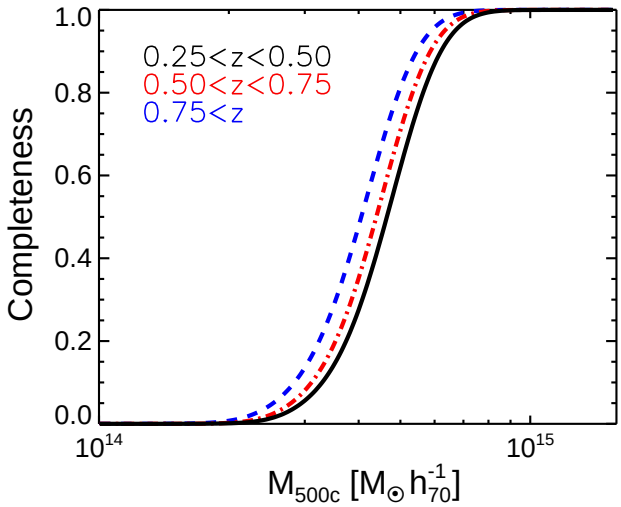

FIG. 7.— Completeness fraction as a function of mass for the SPT cluster sample in three different redshift bins: $0.25 < z < 0.5$ (solid black), $0.5 < z < 0.75$ (dot-dashed red), $z > 0.75$ (dashed blue). The SPT sample is expected to be nearly 100% complete for $M_{500c} > 7 \times 10^{14}\ h_{70}^{-1}\ M_\odot$ at $z > 0.25$. Masses are calculated for a fiducial flat ΛCDM cosmology with $\sigma_8 = 0.80$, $\Omega_b = 0.046$, $\Omega_c = 0.254$, $H_0 = 70$ km/s/Mpc, $\tau = 0.089$, and $n_s(0.002) = 0.972$. Adopting the best-fit *Planck* cosmology (Planck Collaboration et al. 2013b) shifts the mass thresholds up ∼17%.

and $n_s(0.002) = 0.972$—and a fixed ξ-mass scaling relation. In this section we provide a brief overview of the method; readers are referred to the earlier publications for additional details.

To estimate each cluster's mass, we compute the posterior probability density function:

$$P(M|\xi) \propto \left.\frac{dN}{dMdz}\right|_z P(\xi|M) \tag{11}$$

where $\frac{dN}{dMdz}$ is our assumed cluster mass function (Tinker et al. 2008), and $P(\xi|M)$ denotes the ξ-mass scaling relation. We assume an observable-mass scaling relation of the form

$$\zeta = A_{\rm SZ}\left(\frac{M_{500c}}{3\times10^{14}M_\odot h^{-1}}\right)^{B_{\rm SZ}}\left(\frac{H(z)}{H(0.6)}\right)^{C_{\rm SZ}}, \tag{12}$$

parameterized by the normalization $A_{\rm SZ}$ (corrected field-by-field for the different noise levels in each field, see Table 1 and R13), the slope $B_{\rm SZ}$, the redshift evolution $C_{\rm SZ}$ (where $H(z)$ is the Hubble parameter), and a log-normal scatter on ζ, $D_{\rm SZ}$, where ζ is the "unbiased SPT-SZ significance[13]"

$$\zeta = \sqrt{\langle\xi\rangle^2 - 3} \tag{13}$$

for $\zeta > 2$.

We fix the scaling relation parameters to $A_{\rm SZ} = 4.14$, $B_{\rm SZ} = 1.44$, $C_{\rm SZ} = 0.59$, and $D_{\rm SZ} = 0.22$. These values are the best-fit weighted averages as determined from a Monte Carlo Markov chain analysis of the R13 data set assuming a fixed scatter of 0.22 and the above canonical cosmology.[14] We caution that the masses for low-redshift clusters ($z < 0.25$) may be underestimated, and for low-significance clusters ($4.5 < \xi < 5$) the mass estimates should be considered only approximate. At low redshift the SZ signal becomes CMB-confused and therefore fails to obey the power-law form of the scaling relation (Vanderlinde et al. 2010). There is a more subtle complication for low-significance clusters. When we compute $P(M|\xi)$ in Equation 11, the theoretical halo mass function is used as the Bayesian prior. This choice implies a one-to-one mapping between halos and ξ values. However, this assumption breaks down for lower-mass halos, the total number of which approaches the number of independent resolution elements in the filtered SPT maps. Consequently, the contribution of these lower mass systems to $P(M|\xi)$ is overestimated. As we have already confirmed the existence of a massive system by requiring a significant red-sequence galaxy overdensity at the cluster location, we place a prior of $M_{500c} > 1\times10^{14}M_\odot h^{-1}$ when computing mass estimates. Decreasing this prior to $M_{500c} > 5\times10^{13}M_\odot h^{-1}$ typically shifts the mass of the lowest significance systems by less than 0.2σ.

Because we have used a fixed cosmology and scaling relation, the uncertainty reported on each cluster's mass estimate only includes the contributions from measurement noise and the intrinsic scatter in the mass-observable relation. We also expect a comparable level of systematic uncertainty due to uncertainties in cosmology and scaling-relation parameters. This systematic uncertainty will be largely correlated between clusters, and is dominated by the uncertainty in the $\xi-$mass relation and our choice of external cosmological datasets. Here we have intrinsically linked the cluster mass estimates to our chosen cosmology by requiring the measured R13 cluster abundance to be consistent with this model. Assuming different cosmologies can shift the cluster mass scale at a level comparable to the statistical uncertainty on the mass estimates. For example, adopting the best-fit ΛCDM model determined in R13 lowers the mass estimates by ∼8% on average, whereas assuming parameter values consistent with the CMB data from WMAP9 ($\sigma_8 = 0.83$, $\Omega_m = 0.28$, $h = 0.70$; Hinshaw et al. 2013) or *Planck* ($\sigma_8 = 0.84$, $\Omega_m = 0.32$, $h = 0.67$; Planck Collaboration et al. 2013b) typically increases the mass estimates by ∼4 and 17%, respectively.

We would prefer to observationally calibrate the cluster scaling relations and to independently constrain cosmological parameters using clusters. To achieve this goal, the SPT collaboration has undertaken a multi-wavelength campaign to obtain X-ray, galaxy velocity dispersion, and weak lensing measurements for ∼50-100 clusters per technique. Early results from this work have been presented in other SPT publications, including Benson et al. (2013), R13, and Bocquet et al. (2014). In dH14 we will present cosmological constraints from the full 2500 deg^2 SPT-SZ cluster sample. This analysis will combine SZ and X-ray observations (we have obtained *Chandra* data for a significant subset of clusters, see Table 4 and §6.4.1) to both constrain cosmological parameters and better quantify the systematic uncertainties in mass estimates for the cluster sample.

[13] See Appendix B in Vanderlinde et al. (2010)

[14] This scatter was chosen to be consistent with previous constraints from X-ray measurements (Benson et al. 2013; R13).

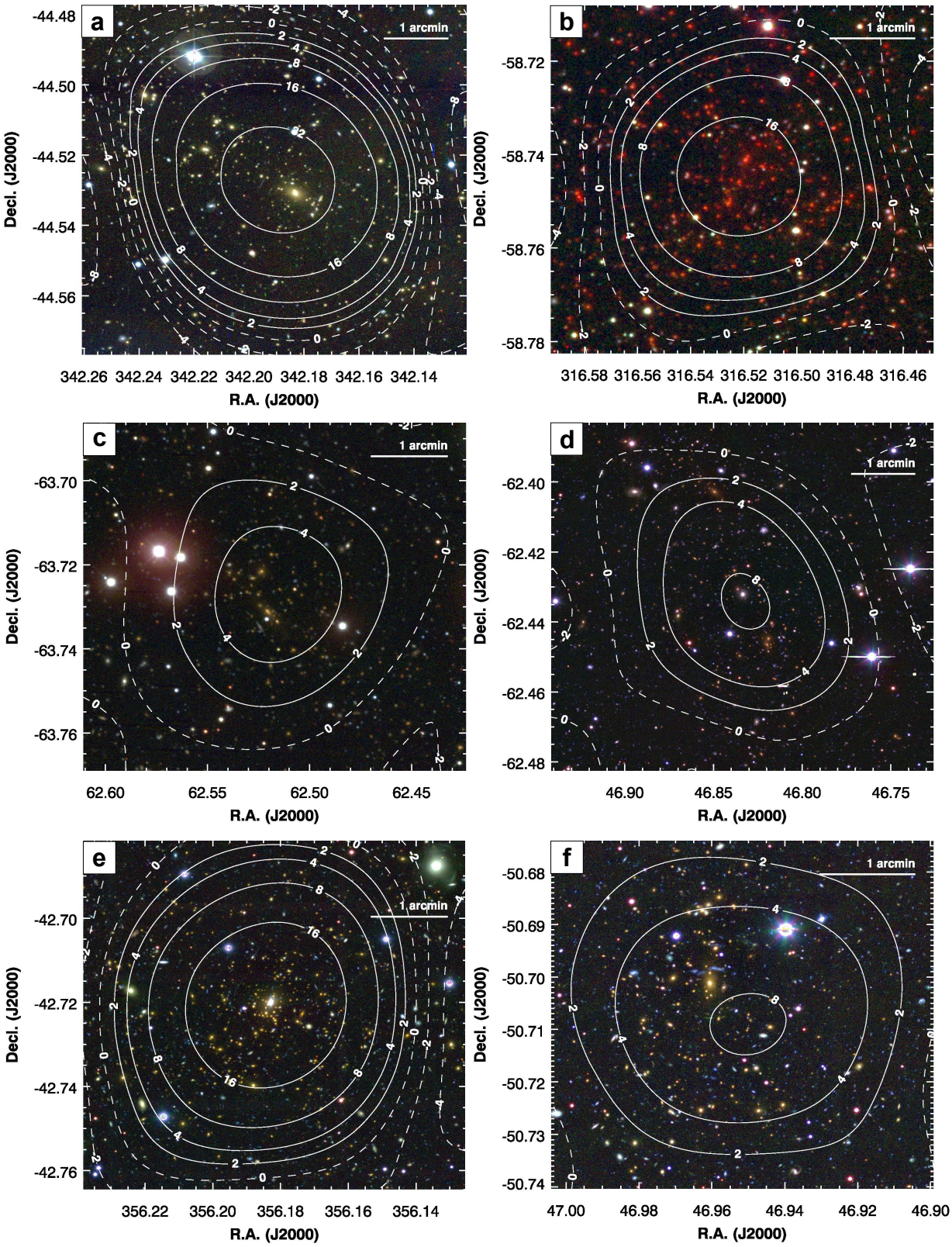

FIG. 8.— A sample of clusters from the 2500 deg^2 SPT-SZ cluster catalog. For each cluster we display an optical/NIR *rgb* image with the SZ detection contours over-plotted; see §6.4 for more details on particularly notable systems. (a) SPT-CL J2248−4431 (ACO S1063; $\xi = 42.4$, $z = 0.351$). This cluster is the most significant detection in the SPT sample (MPG/ESO WFI *IRV*-band image). (b) SPT-CL J2106−5844 ($\xi = 22.2$, $z = 1.132$)—also shown in SPT mm-wave data in Figure 1—is the most massive known cluster at $z > 1$. (*Spitzer*/IRAC 3.6 μm, Magellan/FourStar J-band, Magellan/IMACS i-band image) (c) SPT-CL J0410−6343 ($\xi = 5.6$, $z = 0.52$) is a "typical" SPT cluster at approximately the median redshift and ξ of the confirmed cluster sample. (Blanco/MOSAIC-II *gri*-band image). (d) SPT-CL J0307−6225 ($\xi = 8.5$, $z = 0.581$) is undergoing a major merger. As SZ selection is not greatly influenced by mergers or complicated astrophysics at the cores of clusters (e.g., Motl et al. 2005, Fabjan et al. 2011), the SPT sample is representative of the entire population of massive clusters (Magellan/Megacam *gri*-band image). (e) SPT-CL J2344−4243 (the "Phoenix Cluster"; $\xi = 27.4$, $z = 0.596$) is the most X-ray luminous cluster known. We confirm this cluster as a strong lens using newly-acquired Megacam imaging (Magellan/Megacam *gri*-band image). (f) SPT-CL J0307−5042 ($\xi = 8.4$, $z = 0.55$) is one of many strong-lensing clusters in the SPT sample (Magellan/Megacam *gri*-band image).

6.2. *Cluster Candidates in the Point-source-masked Regions*

The point-source veto discussed in §3 rejects any cluster detections within $8'$ of an emissive source detected above 5σ at 150 GHz in SPT-SZ data. A total area of 163 square degrees was excluded from cluster finding for this reason. While such a conservative approach is appropriate when the goal is a cluster catalog with a clean selection function and a mass-observable relation with minimal outliers, it will almost certainly result in some massive clusters being excluded from the catalog. Assuming no spatial correlation between emissive sources and clusters, we would expect roughly 25 missed clusters above $\xi = 5$.

As in R13, we re-ran the cluster-finding algorithm only masking sources above $S_{150\mathrm{GHz}} = 100$ mJy (as opposed to the normal threshold of $\sim$6 mJy). Each detection with $\xi \geq 5$ and with no counterpart in the original, conservatively masked catalog was visually inspected. The vast majority of these detections were rejected as obvious point-source-related artifacts, but some were clearly significant SZ decrements only minimally affected by the nearby source. These objects are listed in Table 3. We find 19 objects above $\xi = 5$, within roughly 1σ of the naive expectation, assuming purely Poisson statistics. All six candidates that were identified in the analogous procedure in R13 were also identified in this search.[15]

As in R13, these auxiliary candidates were not included in our optical/IR follow-up campaign, and they are not included in the cosmological analysis or in the total number of candidates quoted in the rest of the text. We have searched the literature for counterparts to these clusters in other catalogs, and any literature counterparts are listed in Table 3. We also searched the RASS bright- and faint-source catalogs (Voges et al. 1999, 2000) for X-ray counterparts, and we show in Table 3 whether we find a RASS counterpart within either a $2'$ or $5'$ radius.

6.3. *Comparison to Previous SPT Catalogs*

The SPT collaboration has published three previous samples of galaxy clusters (Vanderlinde et al. 2010, Williamson et al. 2011, R13). The catalog we present here encompasses all of the data used in these previous analyses, so it is a potentially useful cross-check of our new analysis to compare to these earlier samples. The R13 sample included all the clusters in Vanderlinde et al. (2010), using the exact same data and analysis, so we do not perform a separate comparison to Vanderlinde et al. (2010) here. The catalog published in R13 was constructed using an analysis nearly identical to that used here; some small differences were pointed out in §2.2 and we describe the remaining differences here.

First, there is a small difference in the area in each field's map over which clusters are extracted. This area is generally defined in SPT analyses as the set of pixels with total weight above a given fraction of the median weight in the map. To ensure full coverage of the 2500 deg^2 region (i.e., no gaps between fields), we use a slightly lower threshold in this work (70% of the median weight, as opposed to 80% in R13). This results in very slight differences in noise properties and, hence, ξ values for extracted cluster candidates.

For the three fields observed in 2009 (RA21HDEC−60, RA3H30DEC−60, and RA21HDEC−50), we use the same data as in R13, with the only significant analysis difference being the different field border definitions. Therefore, we expect the list of cluster candidates in those fields to be very similar to the corresponding list in R13. Indeed, above a signal-to-noise threshold of $\xi = 5.5$ in these fields, the cluster lists are identical between this work and R13, and the ratio of ξ values for these clusters between the two analyses is 1.00 ± 0.04. Two clusters between $\xi = 5$ and $\xi = 5.5$ from R13 (SPT-CL J0411−5751 and SPT-CL J2104−5224) are not included in the catalog presented here. This absence is due to an update in the point-source lists between the two analyses; both of the $\xi > 5$ R13 clusters missing from the current catalog are within $4'$ of newly identified point sources. There are two clusters in these fields at $5 \leq \xi \leq 5.5$ in the current list that are not in the R13 sample (SPT-CL J2158−5451 and SPT-CL J2143−5509); these are a result of the redefined field boundaries.

For the two fields originally observed in 2008 and re-observed in 2010 or 2011 (RA5H30DEC−55 and RA23H30DEC−55), the analysis in R13 used only the 2008 data, whereas we use both years' data here. We thus expect the cluster list from R13 in these fields to be a subset of the list from these fields in this work, and we expect the average ξ for those clusters to be higher in this work, by a factor related to the extra 150 GHz depth and added 95 GHz information. As expected, all clusters above $\xi = 6$ from R13 in these fields are also present in the sample from this work, and the mean ξ ratio between this work and R13 is 1.28 ± 0.10 for these objects. We note that this ratio should agree with the "field scaling factors" used in dH14 to rescale the normalization parameter in the ξ-mass relation. The average of the two fields' scaling factors in dH14 is 1.35; the ξ ratio we determine here is $\sim$5% lower than this value but consistent within 1σ.

There is one cluster above $\xi = 5$ from the RA5H30DEC−55 and RA23H30DEC−55 fields that drops out of the R13 catalog when we add the new data. The cluster candidate SPT-CL J2343−5521 (detected at $\xi = 5.74$ in R13) is detected at $\xi < 4$ in the full two-year, two-band data. This trend of significance with added data is strong evidence that this is a false detection in the single-year, single-frequency data. This was already the preliminary conclusion in Vanderlinde et al. (2010) and R13, based on null results from optical and X-ray follow-up observations of this candidate.

We also compare the best-fit positions for the clusters detected in common between R13 and this work. The mean difference in positions of clusters in the two catalogs is $0\farcs15 \pm 0\farcs59$ in right ascension and $-0\farcs04 \pm 0\farcs69$ in declination.

We also cross-check the cluster catalog presented in Williamson et al. (2011) with the catalog presented here. Williamson et al. (2011) used full-depth observations of 60% of the SPT-SZ survey area and "preview-depth" (roughly three times the nominal noise level) observa-

[15] There is a systematic $\sim 0\farcs75$ offset between the positions of the R13 clusters found in source-masked areas and their counterparts in Table 3. This is due to a small error in the position calculation in R13. That error was only present in the source-masked cluster positions; as noted in §6.3, the positions in the main catalog here and the main catalog in R13 are in excellent agreement.

tions of the rest of the survey to compile a catalog of the most massive clusters over the full 2500 deg^2 region. All clusters detected in that work are also detected here. One cluster from Williamson et al. (2011)—SPT-CL J0245−5302, also known as ACO S0295—is near a bright radio source and is thus not included in the official catalog in Table 4; it is, however, detected in the alternative analysis in §6.2 that avoids only the very brightest point sources, and it is included in Table 3. The values of ξ in this work for the clusters from full-depth data in Williamson et al. (2011) are consistent with the ξ values reported in that work; for clusters found in preview-depth data in Williamson et al. (2011), the ξ values reported here have increased by roughly a factor of two over that work.

Finally, we note that there may be small differences in redshifts/redshift limits and the confirmation status of cluster candidates. These changes are driven by a mixture (in varying degree per candidate) of additional follow-up data, improved optical data processing and re-estimated redshifts (§5) calibrated using the enlarged SPT spectroscopic sample (§4.2.3).

6.4. *Notable Clusters*

In this section we highlight particularly notable clusters and subsets of clusters from the SPT-SZ cluster catalog.

6.4.1. *The SPT-XVP Sample*

Eighty of the most significant SPT clusters discovered in the first 2000 deg^2 at $z > 0.4$ have been observed by *Chandra* as part of a large X-ray Visionary Project (XVP; PI Benson). As described in R13 and dH14, these observations, with ∼2000 X-ray counts/cluster, play a critical role in constraining the SZ-mass scaling relation and greatly strengthen the cosmological constraining power of the SPT cluster sample. The broad redshift range of this dataset has also enabled constraints on the redshift evolution of the X-ray properties of massive clusters, including measurements of their cooling properties (McDonald et al. 2013b) as well as the redshift evolution of the temperature, pressure and entropy profiles of clusters (McDonald et al. 2014a).

6.4.2. *Massive Clusters at $z > 1$*

The nearly redshift-independent selection of the SPT-SZ cluster sample has led to the discovery of a number of massive, high-redshift clusters. Thirty-seven clusters reported in this work have redshifts estimated at $z > 1$; three systems reported here for the first time: SPT-CL J0459−4947 ($\xi = 6.29$), SPT-CL J0446−4606 ($\xi = 5.71$) and SPT-CL J0334−4645 ($\xi = 4.83$) have redshifts estimated from *Spitzer* observations at $z > 1.5$. Several of the $z > 1$ systems have been the focus of more detailed study including: SPT-CL J0546−5345, the first $z > 1$ cluster detected by its SZ signature (Brodwin et al. 2010); SPT-CL J2106−5844, the most massive known cluster at $z > 1$ ($M_{500c} = 8.3 \times 10^{14}\ h_{70}^{-1} M_\odot$; Foley et al. 2011); SPT-CL J0205−5829 at $z = 1.32$ (Stalder et al. 2013), which features a red sequence whose bright galaxies are well-evolved by $z = 1.3$; and SPT-CL J2040−4451, which intriguingly shows signs of active star formation (Bayliss et al. 2013). At $z = 1.478$, SPT-CL J2040−4451 is the highest-redshift spectroscopically confirmed SPT cluster to date.

6.4.3. *Strong Lensing Clusters*

A number of SPT clusters can be identified from the literature and existing SPT follow-up observations as strong gravitational lenses. Previous SPT publications first identified SPT-CL J0509−5342, SPT-CL J0546−5345 (Staniszewski et al. 2009), SPT-CL J0540−5744, SPT-CL J2331−5051 (High et al. 2010), SPT-CL J2011−5228, and SPT-CL J2011−5725 (Song et al. 2012) as strong-lensing clusters using optical imaging data. SPT-CL J2332−5358 was identified as a lens by the presence of a multiply imaged, high-redshift ($z = 2.73$), dusty star-forming galaxy (Greve et al. 2012; Aravena et al. 2013). The ACT team first reported the discovery of several clusters in the SPT sample (see Table 5) and identified 3 of these systems as strong lenses: SPT-CL J0304−4921, SPT-CL J0330−5228 (Menanteau et al. 2010a), and SPT-CL J0102−4915 (Menanteau et al. 2012; Zitrin et al. 2013). Other previously identified strong-lensing systems include SPT-CL J0658−5556 (1E0657-56/Bullet Cluster; Mehlert et al. 2001), SPT-CL 2031−4037 (RXC J2031.8−4037; Christensen et al. 2012), SPT-CL J2248−4431 (ACO 1063S; Gómez et al. 2012), and SPT-CL J2351−5452 (SCSO J235055−530124; Menanteau et al. 2010b; Buckley-Geer et al. 2011).

In Table 4, we report 30 additional strong gravitational lenses. Optical images of two newly identified strong lenses (SPT-CL J2344−4243 and SPT-CL J2138−6008) are shown in Figure 8. While the majority of these lenses have been identified in ground-based imaging from the follow-up program described in §4, a subset has been identified via the presence of bright arcs in deeper, higher-quality imaging acquired as part of our weak-lensing mass calibration efforts (including 12 lensing clusters in data from the *Hubble Space Telescope*). We note that, given the heterogeneity in image quality in existing follow-up data, this list of strong lenses represents neither an exhaustive nor a uniformly selected sample of systems.

6.4.4. *Notable Individual Systems*

- SPT-CL J2248−4431: First reported as ACO S1063, it is the most significant detection ($\xi = 42.4$, $z = 0.351$, $M_{500c} = 17.3 \times 10^{14}\ h_{70}^{-1}\ M_\odot$) in the SPT-SZ sample. The cluster is the most massive cluster in the SPT-SZ sample, and is the second most X-ray luminous cluster in the REFLEX X-ray catalog (Böhringer et al. 2004). It is scheduled for ultra-deep *Hubble Space Telescope* observations, as one of its Frontier Fields.[16]

- SPT-CL J0102−4915: First reported in Marriage et al. (2011), this cluster is also known as "El Gordo" (Menanteau et al. 2012). Detected in the SPT-SZ survey at $\xi = 39.9$, this massive ($M_{500c} = 14.4 \times 10^{14}\ h_{70}^{-1}\ M_\odot$) merging cluster at $z = 0.870$ is the second most significant detection in the SPT-SZ sample. It has a very high X-ray temperature

[16] http://www.stsci.edu/hst/campaigns/frontier-fields/

TABLE 3
Cluster candidates above $\xi = 5$ in the source-masked area

SPT ID	R.A.	DEC	ξ	θ_c	X-ray counterpart? within 2′	within 5′	Literature name
SPT-CL J0003−5253	0.8237	−52.8970	5.37	2.75	N	N	-
SPT-CL J0115−5959	18.8096	−59.9887	5.91	0.25	Y	Y	-
SPT-CL J0205−4125	31.3274	−41.4224	7.05	1.50	N	N	-
SPT-CL J0222−5335	35.6926	−53.5970	5.16	0.25	N	N	-
SPT-CL J0245−5302	41.3805	−53.0359	15.95	0.50	Y	Y	ACO S0295[a]
SPT-CL J0321−4515	50.3200	−45.2556	5.88	1.50	N	N	-
SPT-CL J0334−6008	53.6899	−60.1497	7.11	1.25	N	Y	-
SPT-CL J0336−4037	54.0689	−40.6314	9.94	0.75	Y	Y	ACO 3140[a]
SPT-CL J0434−5727	68.6315	−57.4523	5.06	0.75	Y	Y	-
SPT-CL J0440−4744	70.2431	−47.7370	5.18	1.25	N	Y	-
SPT-CL J0442−5905	70.6496	−59.0929	6.27	0.25	N	N	-
SPT-CL J0616−5227	94.1430	−52.4546	7.81	0.75	Y	Y	ACT-CL J0616−5227[b]
SPT-CL J2104−4120	316.0754	−41.3475	8.97	2.25	Y	Y	ACO 3739[a]
SPT-CL J2142−6419	325.7063	−64.3224	9.44	0.25	N	N	-
SPT-CL J2154−5952	328.6973	−59.8821	7.10	0.50	N	N	-
SPT-CL J2154−5936	328.7003	−59.6068	6.31	0.50	Y	Y	-
SPT-CL J2246−5244	341.5844	−52.7430	5.67	3.00	Y	Y	ACO 3911[a]
SPT-CL J2300−5100	345.1034	−51.0126	5.22	2.50	N	N	-
SPT-CL J2347−6246	356.8065	−62.7693	6.63	0.25	N	N	ACO 4036[a]

Note. — Cluster candidates identified in a version of the analysis in which only the very brightest (> 100 mJy) point sources are masked (see text for details). Only candidates from the area masked in the standard analysis are listed here. These candidates are not included in cosmological analyses or in the candidate numbers quoted in the text. X-ray counterparts are searched for in the RASS bright- and faint-source catalogs. Literature name and reference are given for the first known identification of the cluster.

[a] Abell et al. (1989)

[b] Marriage et al. (2011)

(14.5 keV), and an X-ray luminosity that makes it the second most X-ray luminous cluster in the SPT-SZ sample (Menanteau et al. 2012).

- SPT-CL J0658−5556: This cluster is the well-known "Bullet" cluster (1ES 0657−558; $z = 0.296$, Tucker et al. (1998); Clowe et al. (2006)). Detected at $\xi = 39.0$, this cluster is the second most massive system ($M_{500c} = 16.9 \times 10^{14}\ h_{70}^{-1}\ M_\odot$) in the SPT-SZ cluster sample.

- SPT-CL J2344−4243: This system, first reported in Williamson et al. (2011), is also known as the "Phoenix Cluster" ($\xi = 27.4$, $z = 0.596$, $M_{500c} = 12.0 \times 10^{14}\ h_{70}^{-1}\ M_\odot$). It is the most X-ray luminous cluster known in the universe. The properties of this system, including those of its central galaxy which exhibits an exceptionally high rate of star formation, are explored in detail in McDonald et al. (2012, 2013a, 2014b). We use newly acquired Magellan/Megacam imaging to identify this system as a strong lens (see Figure 8).

- SPT-CL J0615−5746: This cluster ($\xi = 26.4$, $z = 0.972$, $M_{500c} = 10.5 \times 10^{14}\ h_{70}^{-1}\ M_\odot$) was first reported by SPT in Williamson et al. (2011), and also appears in the *Planck* cluster catalog (Planck Collaboration et al. 2011a). It has a measured X-ray luminosity equal to the Bullet cluster (Planck Collaboration et al. 2011b), but is at significantly higher redshift.

- SPT-CL J2106−5844: As mentioned above, this cluster ($\xi = 22.2$, $z = 1.132$, $M_{500c} = 8.3 \times 10^{14}\ h_{70}^{-1} M_\odot$) is the most massive known cluster at $z > 1$. It has a measured X-ray luminosity nearly equal to SPT-CL J0615−5746, and is described in more detail in Foley et al. (2011).

7. CONCLUSIONS

This work has documented the construction and properties of a catalog of galaxy cluster candidates, selected via their SZ signature in the 2500 deg^2 SPT-SZ survey. Using a spatial-spectral matched filter and a simple peak-finding algorithm, we have used the 95 and 150 GHz survey data to identify 677 cluster candidates above a signal-to-noise threshold of $\xi = 4.5$. From simulated data, we have estimated the purity of this sample to be 75%; above a threshold of $\xi = 5$, simulations have indicated that the sample should be 95% pure. In our optical/NIR follow-up data, we identified clear overdensities of similarly colored galaxies in the direction of 516 (76%) of the $\xi \geq 4.5$ cluster candidates and 387 (95%) of the $\xi \geq 5$ cluster candidates, confirming the predictions from simulations. Of these confirmed clusters, 415 were first identified in SPT data, including 250 new discoveries reported in this work.

We have also used the optical/NIR data to estimate photometric redshifts for all of our candidates with clear counterparts, and we have estimated lower redshift limits for the candidates without counterparts. We have combined these measurements with spectroscopic redshifts for 141 clusters in the sample to estimate the redshift distribution of the sample. The median redshift is $z_{\rm med} = 0.55$, 83 (16%) of the confirmed clusters lie at $z \geq 0.8$, and 37 (7%) lie at $z \geq 1$. Using the framework developed for R13, we report masses using the best-fit ξ-mass relation for a fixed flat ΛCDM cosmology with $\Omega_{\rm m} = 0.3$, $h = 0.7$ and $\sigma_8 = 0.8$. The typical mass of clusters in the sample is $M_{500c} \sim 3.5 \times 10^{14}\, M_\odot\, h_{70}^{-1}$,

nearly independent of redshift. Work is ongoing to improve the mass calibration of SPT clusters using X-ray, galaxy velocity dispersion, and optical weak lensing measurements. Selected data reported in this work, as well as future cluster masses estimated using these datasets, will be hosted at `http://pole.uchicago.edu/public/data/sptsz-clusters`.

SZ-selected samples of galaxy clusters from data with sufficient angular resolution are expected to have a nearly redshift-independent mass limit, and the distribution in mass and redshift of the sample presented here is fully consistent with this expectation. This combination of clean selection, large redshift extent, and high typical mass make this sample of particular interest for cosmological and cluster physics analyses.

The catalog presented in this work represents the complete sample of clusters detected at high significance in the 2500 deg^2 SPT-SZ survey. The program of galaxy cluster science with the SPT continues with the currently fielded SPTpol receiver (Austermann et al. 2012) and will expand further with the expected deployment of the SPT-3G receiver (Benson et al. 2014).

ACKNOWLEDGEMENTS

The South Pole Telescope is supported by the National Science Foundation through grant PLR-1248097. Partial support is also provided by the NSF Physics Frontier Center grant PHY-1125897 to the Kavli Institute of Cosmological Physics at the University of Chicago, the Kavli Foundation and the Gordon and Betty Moore Foundation grant GBMF 947. Galaxy cluster research at Harvard is supported by NSF grant AST-1009012 and at SAO in part by NSF grants AST-1009649 and MRI-0723073. The McGill group acknowledges funding from the National Sciences and Engineering Research Council of Canada, Canada Research Chairs program, and the Canadian Institute for Advanced Research. Argonne National Laboratory's work was supported under U.S. Department of Energy contract DE-AC02-06CH11357. This work was partially completed at Fermilab, operated by Fermi Research Alliance, LLC under Contract No. De-AC02-07CH11359 with the United States Department of Energy. The Munich group acknowledges the support by the DFG Cluster of Excellence "Origin and Structure of the Universe" and the Transregio program TR33 "The Dark Universe". MM acknowledges support by NASA through a Hubble Fellowship grant HST- HF51308.01-A awarded by the Space Telescope Science Institute. T.S. and D.A. acknowledge support from the German Federal Ministry of Economics and Technology (BMWi) provided through DLR under project 50 OR 1210.

Optical imaging data from the Blanco 4 m at Cerro Tololo Interamerican Observatories (programs 2005B-0043, 2009B-0400, 2010A-0441, 2010B-0598) and spectroscopic observations from VLT programs 086.A-0741, 087.A-0843, 088.A-0796(A), 088.A- 0889(A,B,C), and 286.A-5021 and Gemini programs GS-2009B-Q-16, GS-2011A-C-3, GS-2011B-C-6, GS-2012A-Q-4, GS-2012A-Q-37, GS-2012B-Q-29, GS-2012B-Q-59, GS-2013A-Q-5, GS-2013A-Q-45, GS-2013B-Q-25 and GS-2013B-Q-72 were included in this work. Additional data were obtained with the 6.5 m Magellan Telescopes and the Swope telescope, which are located at the Las Campanas Observatory in Chile and the MPG/ESO 2.2 m and ESO NTT located at La Silla Facility in Chile. This work is based in part on observations made with the Spitzer Space Telescope (PIDs 60099, 70053, 80012 and 10101), which is operated by the Jet Propulsion Laboratory, California Institute of Technology under a contract with NASA. Support for this work was provided by NASA through an award issued by JPL/Caltech. This work is also partly based on observations made with the NASA/ESA Hubble Space Telescope, obtained at the Space Telescope Science Institute, which is operated by the Association of Universities for Research in Astronomy, Inc., under NASA contract NAS 5-26555; these observations are associated with programs 12246, 12477, and 13412. The Digitized Sky Surveys were produced at the Space Telescope Science Institute under U.S. Government grant NAG W-2166. The images of these surveys are based on photographic data obtained using the Oschin Schmidt Telescope on Palomar Mountain and the UK Schmidt Telescope. The plates were processed into the present compressed digital form with the permission of these institutions.

Facilities: Blanco (MOSAIC, NEWFIRM), MPG/ESO 2.2m (WFI) Gemini-S (GMOS), HST (ACS), Magellan:Baade (IMACS, FourStar), Magellan:Clay (LDSS3,Megacam), NTT (EFOSC), Spitzer (IRAC), South Pole Telescope, Swope (SITe3), VLT:Antu (FORS2)

REFERENCES

Abate, A., Wittman, D., Margoniner, V. E., Bridle, S. L., Gee, P., Tyson, J. A., & Dell'Antonio, I. P. 2009, ApJ, 702, 603
Abell, G. O. 1958, ApJS, 3, 211
Abell, G. O., Corwin, Jr., H. G., & Olowin, R. P. 1989, ApJS, 70, 1
Allen, S. W., Evrard, A. E., & Mantz, A. B. 2011, ARA&A, 49, 409
Andersson, K., et al. 2011, ApJ, 738, 48
Appenzeller, I., et al. 1998, The Messenger, 94, 1
Aravena, M., et al. 2013, MNRAS, 433, 498
Arnaud, M., Pratt, G. W., Piffaretti, R., Böhringer, H., Croston, J. H., & Pointecouteau, E. 2010, A&A, 517, A92+
Arp, H. C., & Madore, B. F. 1996, VizieR Online Data Catalog, 7170, 0
Ashby, M. L. N., et al. 2013, ApJS, 209, 22
——. 2009, ApJ,, 701, 428
Austermann, J. E., et al. 2012, in Society of Photo-Optical Instrumentation Engineers (SPIE) Conference Series, Vol. 8452, Society of Photo-Optical Instrumentation Engineers (SPIE) Conference Series
Autry, R. G., et al. 2003, in Society of Photo-Optical Instrumentation Engineers (SPIE) Conference Series, Vol. 4841, Society of Photo-Optical Instrumentation Engineers (SPIE) Conference Series, ed. M. Iye & A. F. M. Moorwood, 525–539
Baade, D., et al. 1999, The Messenger, 95, 15
Batuski, D. J., Miller, C. J., Slinglend, K. A., Balkowski, C., Maurogordato, S., Cayatte, V., Felenbok, P., & Olowin, R. 1999, ApJ, 520, 491
Bayliss, M. B., et al. 2013, ArXiv e-prints, 1307.2903
Benson, B. A., et al. 2014, in Society of Photo-Optical Instrumentation Engineers (SPIE) Conference Series, Vol. 9153, Society of Photo-Optical Instrumentation Engineers (SPIE) Conference Series
Benson, B. A., et al. 2013, ApJ, 763, 147

Bertin, E., & Arnouts, S. 1996, A&AS, 117, 393
Bertin, E., Mellier, Y., Radovich, M., Missonnier, G., Didelon, P., & Morin, B. 2002, in Astronomical Society of the Pacific Conference Series, Vol. 281, Astronomical Data Analysis Software and Systems XI, ed. D. A. Bohlender, D. Durand, & T. H. Handley, 228–+
Bleem, L. E., Stalder, B., Brodwin, M., Busha, M. T., Gladders, M. D., High, F. W., Rest, A., & Wechsler, R. H. 2014, ArXiv e-prints, 1403.7186
Bocquet, S., et al. 2014, ArXiv e-prints, 1407.2942
Böhringer, H., et al. 2004, A&A, 425, 367
——. 2000, ApJS, 129, 435
Braid, M. K., & MacGillivray, H. T. 1978, MNRAS, 182, 241
Brodwin, M., et al. 2010, ApJ, 721, 90
——. 2013, ApJ, 779, 138
Bruzual, G., & Charlot, S. 2003, MNRAS, 344, 1000
Buckley-Geer, E. J., et al. 2011, ApJ, 742, 48
Burenin, R. A., Vikhlinin, A., Hornstrup, A., Ebeling, H., Quintana, H., & Mescheryakov, A. 2007, ApJS, 172, 561
Buzzoni, B., et al. 1984, The Messenger, 38, 9
Calabretta, M. R., & Greisen, E. W. 2002, A&A, 395, 1077
Carlstrom, J. E., et al. 2011, PASP, 123, 568
Carlstrom, J. E., Holder, G. P., & Reese, E. D. 2002, ARA&A, 40, 643
Cavaliere, A., & Fusco-Femiano, R. 1976, A&A, 49, 137
Chon, G., & Böhringer, H. 2012, A&A, 538, A35
Christensen, L., et al. 2012, MNRAS, 427, 1953
Clowe, D., Bradač, M., Gonzalez, A. H., Markevitch, M., Randall, S. W., Jones, C., & Zaritsky, D. 2006, ApJ, 648, L109
Colless, M., et al. 2003, VizieR Online Data Catalog, 7226, 0
Coziol, R., Andernach, H., Caretta, C. A., Alamo-Martínez, K. A., & Tago, E. 2009, AJ, 137, 4795
Cruddace, R., et al. 2002, ApJS, 140, 239
Dalton, G. B., Efstathiou, G., Maddox, S. J., & Sutherland, W. J. 1994, MNRAS, 269, 151
Dalton, G. B., Maddox, S. J., Sutherland, W. J., & Efstathiou, G. 1997, MNRAS, 289, 263
de Grandi, S., et al. 1999, ApJ, 514, 148
De Zotti, G., Ricci, R., Mesa, D., Silva, L., Mazzotta, P., Toffolatti, L., & González-Nuevo, J. 2005, A&A, 431, 893
Desai, S., et al. 2012, ApJ, 757, 83
Dressler, A., Hare, T., Bigelow, B. C., & Osip, D. J. 2006, in Society of Photo-Optical Instrumentation Engineers (SPIE) Conference Series, Vol. 6269, Society of Photo-Optical Instrumentation Engineers (SPIE) Conference Series, 62690F
Duus, A., & Newell, B. 1977, ApJS, 35, 209
Ebeling, H., Edge, A. C., & Henry, J. P. 2001, ApJ, 553, 668
Ebeling, H., Voges, W., Bohringer, H., Edge, A. C., Huchra, J. P., & Briel, U. G. 1996, MNRAS, 281, 799
Edge, A. C., Stewart, G. C., Fabian, A. C., & Arnaud, K. A. 1990, MNRAS, 245, 559
Einasto, M., Tago, E., Jaaniste, J., Einasto, J., & Andernach, H. 1997, A&AS, 123, 119
Eisenhardt, P. R. M., et al. 2008, ApJ, 684, 905
Fabjan, D., Borgani, S., Rasia, E., Bonafede, A., Dolag, K., Murante, G., & Tornatore, L. 2011, MNRAS, 416, 801
Fagotto, F., Bressan, A., Bertelli, G., & Chiosi, C. 1994, A&AS, 104, 365
Fazio, G. G., et al. 2004, ApJS, 154, 10
Feitsova, T. S. 1981, Soviet Ast., 25, 647
Foley, R. J., et al. 2011, ApJ, 731, 86
Garg, A., et al. 2007, AJ, 133, 403
Gettings, D. P., et al. 2012, ApJ, 759, L23
Gioia, I. M., Maccacaro, T., Schild, R. E., Wolter, A., Stocke, J. T., Morris, S. L., & Henry, J. P. 1990, ApJS, 72, 567
Gladders, M. D., & Yee, H. K. C. 2000, AJ, 120, 2148
Gómez, P. L., et al. 2012, AJ, 144, 79
Gonzalez, A. H., et al. 2010, in American Astronomical Society Meeting Abstracts, Vol. 216, American Astronomical Society Meeting Abstracts #216, 415.13
Greve, T. R., et al. 2012, ApJ, 756, 101
Guzzo, L., et al. 2009, A&A, 499, 357
Haiman, Z., Mohr, J. J., & Holder, G. P. 2001, ApJ, 553, 545
Hasselfield, M., et al. 2013, JCAP , 7, 8
High, F. W., et al. 2012, ApJ, 758, 68
——. 2010, ApJ, 723, 1736
High, F. W., Stubbs, C. W., Rest, A., Stalder, B., & Challis, P. 2009, AJ, 138, 110
Hinshaw, G., et al. 2013, ApJS, 208, 19
Hook, I. M., Jørgensen, I., Allington-Smith, J. R., Davies, R. L., Metcalfe, N., Murowinski, R. G., & Crampton, D. 2004, PASP, 116, 425
Horesh, A., Maoz, D., Ebeling, H., Seidel, G., & Bartelmann, M. 2010, MNRAS, 406, 1318
Jones, D. H., et al. 2009, MNRAS, 399, 683
Katgert, P., et al. 1996, A&A, 310, 8
Keisler, R., et al. 2011, ApJ, 743, 28
Koester, B. P., et al. 2007, ApJ, 660, 221
Komatsu, E., et al. 2011, ApJS, 192, 18
Kravtsov, A. V., & Borgani, S. 2012, ARA&A, 50, 353
Lesgourgues, J., & Pastor, S. 2006, Phys. Rep., 429, 307
Lidman, C. E., & Peterson, B. A. 1996, AJ, 112, 2454
Lobo, C., Iovino, A., Lazzati, D., & Chincarini, G. 2000, A&A, 360, 896
Lugger, P. M. 1978, ApJ, 221, 745
Lumsden, S. L., Nichol, R. C., Collins, C. A., & Guzzo, L. 1992, MNRAS, 258, 1
Mandelbaum, R., Seljak, U., & Hirata, C. M. 2008, Journal of Cosmology and Astro-Particle Physics, 8, 6
Mantz, A., Allen, S. W., Rapetti, D., & Ebeling, H. 2010, MNRAS, 406, 1759
Marriage, T. A., et al. 2011, ApJ, 737, 61
McDonald, M., et al. 2012, Nature, 488, 349
McDonald, M., Benson, B., Veilleux, S., Bautz, M. W., & Reichardt, C. L. 2013a, ApJ, 765, L37
McDonald, M., et al. 2014a, ArXiv e-prints, 1404.6250
——. 2013b, ApJ, 774, 23
——. 2014b, ApJ, 784, 18
McLeod, B., Geary, J., Ordway, M., Amato, S., Conroy, M., & Gauron, T. 2006, in Scientific Detectors for Astronomy 2005, ed. J. E. Beletic, J. W. Beletic, & P. Amico, 337
Mehlert, D., et al. 2001, A&A, 379, 96
Mei, S., et al. 2009, ApJ, 690, 42
Melin, J.-B., Bartlett, J. G., & Delabrouille, J. 2006, A&A, 459, 341
Menanteau, F., et al. 2010a, ApJ, 723, 1523
——. 2010b, ApJS, 191, 340
——. 2012, ApJ, 748, 7
Miknaitis, G., et al. 2007, ApJ, 666, 674
Motl, P. M., Hallman, E. J., Burns, J. O., & Norman, M. L. 2005, ApJ, 623, L63
Muzzin, A., et al. 2012, ApJ, 746, 188
Nagai, D., Kravtsov, A. V., & Vikhlinin, A. 2007, ApJ, 668, 1
Nozawa, S., Itoh, N., Kawana, Y., & Kohyama, Y. 2000, ApJ, 536, 31
Olsen, L. F., et al. 1999, A&A, 345, 681
Panko, E., & Flin, P. 2006, Journal of Astronomical Data, 12, 1
Persson, S. E., et al. 2013, PASP, 125, 654
Piffaretti, R., Arnaud, M., Pratt, G. W., Pointecouteau, E., & Melin, J.-B. 2011, A&A, 534, A109
Planck Collaboration, et al. 2013a, ArXiv e-prints, 1303.5089
——. 2013b, ArXiv e-prints, 1303.5076, paper XVI
——. 2011a, A&A, 536, A8
——. 2011b, A&A, 536, A26
——. 2012, A&A, 543, A102
Quintana, H., & White, R. A. 1990, Ap&SS, 173, 265
Ramsay, J. O. 1998, Journal of the Royal Statistical Society: Series B (Statistical Methodology), 60, 365
Reichardt, C. L., et al. 2012, ApJ, 755, 70
——. 2013, ApJ, 763, 127
Rest, A., et al. 2005, ApJ, 634, 1103
Rose, J. A. 1976, A&AS, 23, 109
Ruel, J., et al. 2013, ArXiv e-prints, 1311.4953, apJ accepted
Rykoff, E. S., et al. 2012, ApJ, 746, 178
——. 2014, ApJ, 785, 104
Saliwanchik, B. R., et al. 2013, ArXiv e-prints, 1312.3015, submitted to ApJ
Salpeter, E. E. 1955, ApJ, 121, 161
Sayers, J., et al. 2009, ApJ, 690, 1597
Schaffer, K. K., et al. 2011, ApJ, 743, 90
Schwope, A., et al. 2000, Astronomische Nachrichten, 321, 1
Sérsic, J. L. 1974, Ap&SS, 28, 365
Shirokoff, E., et al. 2011, ApJ, 736, 61

Sifón, C., et al. 2013, ApJ, 772, 25
Skrutskie, M. F., et al. 2006, AJ, 131, 1163
Song, J., et al. 2012, ApJ, 761, 22
Stalder, B., et al. 2013, ApJ, 763, 93
Stanford, S. A., Gonzalez, A. H., Brodwin, M., Gettings, D. P., Eisenhardt, P. R. M., Stern, D., & Wylezalek, D. 2014, ArXiv e-prints, 1403.3361, ApJ accepted
Staniszewski, Z., et al. 2009, ApJ, 701, 32
Story, K. T., et al. 2013, ApJ, 779, 86
Struble, M. F., & Rood, H. J. 1999, ApJS, 125, 35
Sunyaev, R., & Zel'dovich, Y. 1980, ARAA, 18, 537
Sunyaev, R. A., & Zel'dovich, Y. B. 1972, Comments on Astrophysics and Space Physics, 4, 173
Tinker, J., Kravtsov, A. V., Klypin, A., Abazajian, K., Warren, M., Yepes, G., Gottlöber, S., & Holz, D. E. 2008, ApJ, 688, 709
Tozzi, P., Rosati, P., Ettori, S., Borgani, S., Mainieri, V., & Norman, C. 2003, ApJ, 593, 705
Tucker, W., et al. 1998, ApJ, 496, L5
Šuhada, R., et al. 2012, A&A, 537, A39
Vanderlinde, K., et al. 2010, ApJ, 722, 1180
Vieira, J. D., et al. 2010, ApJ, 719, 763
Vikhlinin, A., et al. 2009, ApJ, 692, 1060
Voges, W., et al. 1999, A&A, 349, 389
——. 2000, VizieR Online Data Catalog, 9029, 0
Voit, G. M. 2005, Reviews of Modern Physics, 77, 207
Wang, L., & Steinhardt, P. J. 1998, ApJ, 508, 483
Wang, S., Haiman, Z., Hu, W., Khoury, J., & May, M. 2005, Physical Review Letters, 95, 011302
Webb, T. M. A., et al. 2013, AJ, 146, 84
Weinberg, D. H., Mortonson, M. J., Eisenstein, D. J., Hirata, C., Riess, A. G., & Rozo, E. 2013, Phys. Rep., 530, 87
Wen, Z. L., Han, J. L., & Liu, F. S. 2012, ApJS, 199, 34
West, R. M., & Frandsen, S. 1981, A&AS, 44, 329
Williamson, R., et al. 2011, ApJ, 738, 139
Wittman, D., Dell'Antonio, I. P., Hughes, J. P., Margoniner, V. E., Tyson, J. A., Cohen, J. G., & Norman, D. 2006, ApJ, 643, 128
Wright, E. L., et al. 2010, AJ, 140, 1868
Zenteno, A., et al. 2011, ApJ, 734, 3
Zitrin, A., Menanteau, F., Hughes, J. P., Coe, D., Barrientos, L. F., Infante, L., & Mandelbaum, R. 2013, ApJ, 770, L15

APPENDIX

THE CLUSTER CATALOG

TABLE 4
Galaxy clusters above $\xi = 4.5$ in 2500 square degrees observed by the SPT.

SPT ID	R.A. (J2000)	Decl. (J2000)	Best ξ	Best θ_c	$Y_{SZ} \times 10^6$ (arcmin^2)	Redshift	M_{500c} ($10^{14} h_{70}^{-1} M_\odot$)	Imaging	Notes
SPT-CL J0000−4356	0.0663	−43.9494	5.92	0.25	76 ± 21	1.00 ± 0.11	3.27 ± 0.71	2	
SPT-CL J0000−5748*	0.2499	−57.8064	8.49	0.50	82 ± 12	0.702^+	4.56 ± 0.80	2	a
SPT-CL J0001−4842	0.2768	−48.7132	5.69	1.25	77 ± 12	0.30 ± 0.04	3.96 ± 0.87	5	
SPT-CL J0001−4024	0.3610	−40.4108	5.42	0.75	59 ± 12	0.85 ± 0.07	3.12 ± 0.75	2, 10	
SPT-CL J0001−6258	0.4029	−62.9808	4.69	1.50	51 ± 16	0.21 ± 0.02	3.27 ± 0.91	3	b,c
SPT-CL J0001−5440	0.4059	−54.6697	5.69	1.00	60 ± 12	0.73 ± 0.06	3.54 ± 0.79	1, 10	
SPT-CL J0002−5557	0.5138	−55.9621	5.20	0.25	54 ± 18	1.14 ± 0.08	2.47 ± 0.60	3, 10	
SPT-CL J0002−5224	0.6433	−52.4092	4.67	1.00	48 ± 12	> 0.71	···	2	
SPT-CL J0003−4155	0.7842	−41.9307	4.75	0.25	58 ± 20	> 0.76	···	3	
SPT-CL J0007−4706	1.7514	−47.1159	4.55	0.75	58 ± 13	0.51 ± 0.04	2.95 ± 0.85	5	b
SPT-CL J0010−5112	2.7408	−51.2077	4.51	0.25	54 ± 12	0.17 ± 0.02	3.25 ± 0.94	7	b,c
SPT-CL J0011−4614	2.9779	−46.2351	5.12	0.75	63 ± 17	0.57 ± 0.04	3.30 ± 0.85	5	a
SPT-CL J0012−5352	3.0649	−53.8736	4.80	0.25	51 ± 14	0.33 ± 0.04	3.31 ± 0.91	5	b
SPT-CL J0013−5714	3.3029	−57.2373	5.11	1.50	59 ± 13	> 0.86	···	1	
SPT-CL J0013−4906*	3.3290	−49.1151	11.22	0.75	135 ± 12	0.406^+	7.08 ± 1.15	1	
SPT-CL J0013−5310	3.4111	−53.1718	4.66	0.25	56 ± 19	> 0.82	···	3	
SPT-CL J0013−4621	3.4715	−46.3563	4.54	1.75	63 ± 17	0.18 ± 0.05	3.26 ± 0.94	7	b,c
SPT-CL J0014−4952*	3.6969	−49.8772	8.87	0.25	123 ± 26	0.752^+	5.31 ± 0.92	1	
SPT-CL J0014−4036	3.7433	−40.6031	9.72	0.25	112 ± 15	0.55 ± 0.03	5.89 ± 0.99	2	
SPT-CL J0015−6000	3.8824	−60.0001	5.11	0.25	67 ± 19	0.68 ± 0.04	3.11 ± 0.80	6	
SPT-CL J0019−4051	4.7600	−40.8596	9.67	0.50	114 ± 14	0.44 ± 0.04	6.06 ± 1.02	5	
SPT-CL J0019−5527	4.8313	−55.4528	6.21	0.25	90 ± 20	0.76 ± 0.06	3.77 ± 0.78	6, 10	
SPT-CL J0021−4902	5.3811	−49.0360	5.32	0.50	68 ± 12	0.70 ± 0.06	3.30 ± 0.81	2, 10	
SPT-CL J0022−4144	5.5489	−41.7366	5.14	0.50	64 ± 11	0.27 ± 0.05	3.55 ± 0.88	7	
SPT-CL J0022−4258	5.6672	−42.9808	4.77	0.25	63 ± 21	> 0.75	···	2	
SPT-CL J0025−5034	6.3671	−50.5716	4.77	1.00	54 ± 12	0.38 ± 0.04	3.24 ± 0.90	5	b
SPT-CL J0025−4133	6.4915	−41.5540	6.59	0.50	83 ± 15	0.43 ± 0.05	4.38 ± 0.88	7	
SPT-CL J0027−5015	6.8228	−50.2524	5.00	0.50	25 ± 9	0.145	3.68 ± 0.95	6	c
SPT-CL J0027−4742	6.9158	−47.7151	6.40	0.50	84 ± 15	0.75 ± 0.04	3.97 ± 0.81	6	
SPT-CL J0027−6325	6.9435	−63.4301	4.95	0.25	54 ± 12	0.38 ± 0.03	3.30 ± 0.88	2	b
SPT-CL J0028−4126	7.0184	−41.4451	4.77	0.25	62 ± 20	> 0.65	···	2	
SPT-CL J0030−4457	7.5150	−44.9640	4.68	2.50	42 ± 14	> 0.69	···	2	
SPT-CL J0030−5213	7.5338	−52.2240	4.65	0.25	51 ± 12	0.55 ± 0.03	2.98 ± 0.84	2	b
SPT-CL J0033−6326*	8.4767	−63.4463	7.50	0.75	82 ± 13	0.597^+	4.72 ± 0.88	5	
SPT-CL J0034−5554	8.5906	−55.9013	4.54	1.00	55 ± 20	> 0.67	···	2	
SPT-CL J0036−4411	9.1758	−44.1849	5.66	0.75	74 ± 21	0.869	3.25 ± 0.74	5	
SPT-CL J0037−5047*	9.4441	−50.7971	6.93	0.25	87 ± 14	1.026^+	3.91 ± 0.76	1, 10	
SPT-CL J0038−5244	9.7204	−52.7390	4.83	0.75	68 ± 13	0.42 ± 0.04	3.24 ± 0.89	5	b
SPT-CL J0040−4407*	10.2048	−44.1329	19.34	0.50	219 ± 13	0.350^+	10.24 ± 1.56	1	a
SPT-CL J0041−4428	10.2513	−44.4785	8.84	0.50	101 ± 12	0.33 ± 0.02	5.83 ± 1.01	1	
SPT-CL J0041−5107	10.2932	−51.1286	4.60	0.25	61 ± 15	0.45 ± 0.04	3.04 ± 0.87	5	b
SPT-CL J0043−4843	10.9696	−48.7235	5.17	0.75	60 ± 12	0.73 ± 0.06	3.16 ± 0.81	7, 10	
SPT-CL J0044−4037	11.1232	−40.6282	4.92	0.25	62 ± 12	0.96 ± 0.07	2.68 ± 0.72	2, 10	b
SPT-CL J0044−4100	11.1921	−41.0016	4.57	2.00	53 ± 12	> 0.78	···	6	
SPT-CL J0047−4506	11.8207	−45.1131	7.55	0.50	88 ± 14	0.39 ± 0.03	5.02 ± 0.93	1	
SPT-CL J0048−5244	12.0901	−52.7487	6.31	0.25	82 ± 23	0.92 ± 0.07	3.70 ± 0.76	1, 10	a
SPT-CL J0048−4450	12.1743	−44.8475	4.82	0.50	53 ± 12	> 0.57	···	2	
SPT-CL J0048−6416	12.2372	−64.2690	5.57	0.25	67 ± 14	0.77 ± 0.06	3.33 ± 0.77	2, 10	a
SPT-CL J0048−4548	12.2483	−45.8018	4.83	0.75	59 ± 13	0.46 ± 0.04	3.20 ± 0.88	5	b
SPT-CL J0049−4542	12.3693	−45.7099	4.63	0.75	61 ± 12	0.82 ± 0.04	2.71 ± 0.76	3	b
SPT-CL J0049−5315	12.3825	−53.2505	6.35	0.25	76 ± 13	0.62 ± 0.06	4.12 ± 0.84	1, 10	
SPT-CL J0051−4834	12.7905	−48.5776	7.39	1.25	81 ± 12	0.187	5.38 ± 1.01	5	c
SPT-CL J0052−5657	13.1621	−56.9606	4.92	0.25	60 ± 14	0.33 ± 0.04	3.34 ± 0.89	5	b
SPT-CL J0052−4551	13.1930	−45.8605	5.09	0.25	68 ± 15	0.35 ± 0.04	3.53 ± 0.90	5	
SPT-CL J0054−4046	13.5908	−40.7759	5.44	0.75	63 ± 12	0.49 ± 0.10	3.54 ± 0.82	7	
SPT-CL J0058−6145*	14.5799	−61.7635	7.52	0.25	98 ± 24	0.83 ± 0.07	4.36 ± 0.81	1, 10	
SPT-CL J0059−5105	14.7774	−51.0934	4.88	1.25	65 ± 18	0.60 ± 0.03	3.09 ± 0.84	1	b
SPT-CL J0100−5359	15.0163	−53.9848	4.74	0.25	63 ± 20	0.94 ± 0.07	2.66 ± 0.74	3, 10	b
SPT-CL J0102−4603*	15.6690	−46.0647	7.33	0.25	100 ± 23	0.72 ± 0.06	4.49 ± 0.85	1, 10	
SPT-CL J0102−4915*	15.7294	−49.2611	39.91	0.75	486 ± 12	0.870	14.43 ± 2.10	1	a

TABLE 4 — *Continued*

SPT ID	R.A. (J2000)	Decl. (J2000)	Best ξ	Best θ_c	Y_{SZ} $\times 10^6$ (arcmin^2)	Redshift	M_{500c} ($10^{14} h_{70}^{-1} M_\odot$)	Imaging	Notes
SPT-CL J0103−4250	15.9144	−42.8334	6.60	0.25	86 ± 21	0.72 ± 0.06	4.00 ± 0.80	5, 10	
SPT-CL J0104−4351	16.1290	−43.8640	7.35	0.25	96 ± 24	0.76 ± 0.07	4.36 ± 0.82	2, 10	
SPT-CL J0105−5358	16.3908	−53.9717	4.53	0.25	62 ± 21	···	···	···	
SPT-CL J0106−5355	16.5705	−53.9281	4.88	0.50	54 ± 16	0.44 ± 0.04	3.26 ± 0.89	5	a,b
SPT-CL J0106−5943*	16.6152	−59.7214	9.57	0.50	115 ± 15	0.348^+	6.23 ± 1.05	5	
SPT-CL J0107−4855	16.8857	−48.9171	4.51	0.25	58 ± 18	0.60 ± 0.03	2.84 ± 0.81	6	b
SPT-CL J0107−5833	16.9102	−58.5520	5.10	0.25	70 ± 22	1.23 ± 0.08	2.55 ± 0.67	1, 10	
SPT-CL J0108−4341	17.1286	−43.6923	4.59	0.50	51 ± 14	0.19 ± 0.02	3.19 ± 0.90	7	b,c
SPT-CL J0108−4659	17.1387	−46.9955	5.20	0.25	72 ± 22	1.20 ± 0.08	2.69 ± 0.70	1, 10	
SPT-CL J0109−4045	17.4772	−40.7659	4.73	0.25	60 ± 16	0.55 ± 0.03	2.95 ± 0.82	2	b
SPT-CL J0110−4445	17.5861	−44.7596	7.91	1.50	82 ± 12	0.38 ± 0.04	5.24 ± 0.95	5	
SPT-CL J0111−5424	17.7686	−54.4151	5.31	1.25	54 ± 13	0.47 ± 0.03	3.57 ± 0.86	1	
SPT-CL J0111−5818	17.8404	−58.3004	4.62	0.25	70 ± 22	> 0.65	···	5	
SPT-CL J0111−5518	17.8446	−55.3138	4.54	1.25	47 ± 17	0.56 ± 0.03	2.84 ± 0.81	6	b
SPT-CL J0112−4056	18.0257	−40.9456	4.90	0.50	54 ± 13	> 0.83	···	3	
SPT-CL J0112−5030	18.0354	−50.5074	4.50	3.00	57 ± 14	···	···	···	
SPT-CL J0113−6105	18.3980	−61.0941	4.64	1.00	41 ± 12	0.34 ± 0.04	3.12 ± 0.88	7	b
SPT-CL J0114−4123	18.6812	−41.3968	11.43	1.50	127 ± 12	0.38 ± 0.04	7.00 ± 1.14	5	
SPT-CL J0117−6032	19.3645	−60.5403	6.87	0.75	77 ± 16	0.93 ± 0.07	3.92 ± 0.76	1, 10	
SPT-CL J0117−4617	19.4942	−46.2940	4.61	0.25	71 ± 22	> 0.58	···	1	
SPT-CL J0118−5638	19.5385	−56.6339	5.10	1.25	53 ± 12	0.21 ± 0.04	3.62 ± 0.90	5	c
SPT-CL J0118−5156	19.5990	−51.9434	5.97	0.25	81 ± 21	0.705^+	3.76 ± 0.80	1	
SPT-CL J0118−4457	19.7203	−44.9662	4.94	0.25	64 ± 21	> 0.73	···	2	
SPT-CL J0119−5919	19.9065	−59.3293	5.01	1.00	60 ± 17	0.62 ± 0.03	3.09 ± 0.82	2	
SPT-CL J0123−4821*	20.7923	−48.3588	6.92	0.25	91 ± 14	0.62 ± 0.03	4.46 ± 0.87	1	
SPT-CL J0124−4301	21.1454	−43.0208	5.25	1.25	61 ± 13	0.47 ± 0.04	3.42 ± 0.84	5	
SPT-CL J0124−5937	21.1988	−59.6255	5.88	0.50	63 ± 14	0.21 ± 0.03	4.23 ± 0.90	5	c
SPT-CL J0129−6432	22.4347	−64.5449	10.25	1.25	100 ± 12	0.326	6.61 ± 1.10	5	
SPT-CL J0131−5921	22.8565	−59.3617	5.95	0.25	89 ± 18	0.96 ± 0.07	3.36 ± 0.73	1, 10	
SPT-CL J0131−5604	22.9331	−56.0821	6.60	0.75	82 ± 12	0.69 ± 0.06	4.08 ± 0.81	1, 10	
SPT-CL J0133−6434	23.4103	−64.5668	9.15	2.00	109 ± 12	0.29 ± 0.04	6.11 ± 1.05	5	
SPT-CL J0135−5902	23.7918	−59.0361	5.05	0.25	65 ± 16	0.51 ± 0.03	3.25 ± 0.84	2	
SPT-CL J0135−5904	23.9753	−59.0814	4.52	0.25	64 ± 16	0.49 ± 0.03	2.89 ± 0.83	2	b
SPT-CL J0139−5204	24.8989	−52.0825	5.12	0.25	72 ± 21	0.76 ± 0.06	3.08 ± 0.81	2, 10	
SPT-CL J0139−5508	24.9353	−55.1490	4.52	0.75	54 ± 16	> 0.76	···	2	1
SPT-CL J0140−4833	25.1676	−48.5631	4.74	0.50	56 ± 15	0.88 ± 0.07	2.64 ± 0.73	2, 10	b
SPT-CL J0142−5032*	25.5452	−50.5438	10.12	0.75	117 ± 12	0.73 ± 0.03	5.75 ± 0.95	2	a
SPT-CL J0143−4452	25.8853	−44.8741	5.03	1.50	56 ± 12	0.27 ± 0.03	3.46 ± 0.89	6	2
SPT-CL J0144−4157	26.1463	−41.9601	5.16	0.50	54 ± 13	> 0.79	···	7	
SPT-CL J0144−4807	26.1795	−48.1281	4.84	2.50	57 ± 15	0.31 ± 0.04	3.27 ± 0.89	5	b
SPT-CL J0145−5301	26.2645	−53.0295	7.37	2.50	84 ± 17	0.117	5.30 ± 1.00	5	c
SPT-CL J0145−4426	26.2824	−44.4390	4.83	0.50	58 ± 14	0.59 ± 0.03	2.97 ± 0.82	2	b
SPT-CL J0145−6033	26.2958	−60.5594	10.76	0.50	118 ± 17	0.179	7.14 ± 1.17	5	c
SPT-CL J0145−5040	26.4397	−50.6812	4.78	0.50	56 ± 13	> 0.90	···	2	
SPT-CL J0146−6126	26.6503	−61.4365	4.87	0.25	66 ± 22	> 0.72	···	2	
SPT-CL J0147−5622	26.9652	−56.3779	4.96	0.25	62 ± 14	0.64 ± 0.03	3.03 ± 0.81	1	3,b
SPT-CL J0148−4518	27.0985	−45.3023	5.12	0.50	58 ± 19	0.62 ± 0.03	3.16 ± 0.81	2	
SPT-CL J0148−4700	27.2414	−47.0048	4.55	1.50	45 ± 13	0.75 ± 0.06	2.66 ± 0.75	1, 10	b
SPT-CL J0150−4511	27.6483	−45.1894	7.19	1.25	81 ± 12	0.32 ± 0.04	4.91 ± 0.94	5	
SPT-CL J0151−5654	27.7898	−56.9110	4.74	0.50	60 ± 12	0.29 ± 0.04	3.24 ± 0.90	5	b
SPT-CL J0151−4300	27.8277	−43.0004	4.56	0.25	63 ± 19	> 0.85	···	3	
SPT-CL J0151−5954*	27.8597	−59.9059	7.73	0.25	104 ± 26	1.03 ± 0.07	4.20 ± 0.77	1, 10	
SPT-CL J0152−5303	28.2342	−53.0540	6.87	0.75	78 ± 13	0.55 ± 0.04	4.39 ± 0.86	5	
SPT-CL J0154−4824	28.5911	−48.4068	5.47	0.25	78 ± 20	1.30 ± 0.08	2.69 ± 0.66	2, 10	
SPT-CL J0156−5541*	29.0449	−55.6980	6.98	0.25	96 ± 24	1.22 ± 0.08	3.63 ± 0.70	1, 10	
SPT-CL J0157−4007	29.4494	−40.1263	5.75	1.50	63 ± 12	0.55 ± 0.03	3.69 ± 0.81	2	
SPT-CL J0157−6442	29.4831	−64.7060	5.65	0.25	74 ± 22	0.84 ± 0.07	3.31 ± 0.75	1, 10	
SPT-CL J0200−4852*	30.1436	−48.8757	7.38	0.75	83 ± 12	0.498^+	4.76 ± 0.90	5	
SPT-CL J0201−6051	30.3953	−60.8586	5.06	0.25	66 ± 18	> 1.50	···	1, 10	
SPT-CL J0202−5401	30.5756	−54.0242	5.65	1.00	59 ± 12	0.55 ± 0.03	3.63 ± 0.81	3	
SPT-CL J0202−4309	30.6744	−43.1648	4.62	2.75	47 ± 15	> 1.50	···	10	
SPT-CL J0202−4437	30.6870	−44.6234	4.85	2.50	52 ± 14	> 1.50	···	6, 10	
SPT-CL J0203−5651	30.8313	−56.8613	4.88	0.25	61 ± 18	> 1.50	···	1, 10	4
SPT-CL J0205−4937	31.2681	−49.6245	4.64	3.00	47 ± 13	> 0.76	···	2	
SPT-CL J0205−6432	31.2794	−64.5457	5.83	0.50	66 ± 14	0.744^+	3.40 ± 0.74	1	

TABLE 4 — *Continued*

SPT ID	R.A. (J2000)	Decl. (J2000)	Best ξ	Best θ_c	Y_{SZ} $\times 10^6$ (arcmin^2)	Redshift	M_{500c} ($10^{14} h_{70}^{-1} M_\odot$)	Imaging	Notes
SPT-CL J0205−5829	31.4428	−58.4852	10.40	0.25	131 ± 28	1.322^+	4.74 ± 0.77	3, 10	a
SPT-CL J0206−4206	31.5747	−42.1100	4.63	0.50	55 ± 16	···	···	···	
SPT-CL J0208−4425	32.2069	−44.4223	4.86	1.00	54 ± 13	> 0.77	···	2	
SPT-CL J0211−5712	32.8232	−57.2160	4.51	0.25	59 ± 19	> 1.00	···	1, 8	
SPT-CL J0212−4657*	33.1061	−46.9502	10.05	0.75	114 ± 14	0.655^+	5.88 ± 0.98	6	5
SPT-CL J0214−4638	33.7017	−46.6483	6.50	1.75	63 ± 11	0.27 ± 0.02	4.54 ± 0.91	1	
SPT-CL J0216−4219	34.0628	−42.3281	5.82	0.75	59 ± 13	0.62 ± 0.03	3.63 ± 0.79	6	
SPT-CL J0216−4816	34.0658	−48.2765	4.97	0.50	66 ± 14	0.171	3.51 ± 0.91	5	b,c
SPT-CL J0216−4830	34.0723	−48.5147	6.23	0.50	70 ± 15	0.47 ± 0.03	4.11 ± 0.85	3	
SPT-CL J0216−4627	34.1101	−46.4604	4.82	0.75	65 ± 18	0.54 ± 0.04	3.02 ± 0.83	7	b
SPT-CL J0216−5730	34.1384	−57.5095	5.05	0.50	57 ± 12	> 0.80	···	2	
SPT-CL J0216−6409	34.1743	−64.1559	5.35	0.25	58 ± 15	0.65 ± 0.03	3.20 ± 0.77	1	
SPT-CL J0217−5014	34.2653	−50.2380	4.65	0.75	54 ± 12	0.57 ± 0.05	2.88 ± 0.81	5	b
SPT-CL J0217−5245*	34.3035	−52.7560	6.46	0.50	77 ± 13	0.343	4.42 ± 0.89	5	
SPT-CL J0217−4310	34.4138	−43.1819	6.54	1.75	68 ± 11	0.52 ± 0.03	4.21 ± 0.85	7	
SPT-CL J0218−4233	34.5520	−42.5555	4.52	0.25	58 ± 19	0.68 ± 0.06	2.68 ± 0.76	10	b
SPT-CL J0218−4315	34.5775	−43.2606	9.85	0.75	109 ± 12	0.56 ± 0.04	5.91 ± 0.99	7	
SPT-CL J0219−4934	34.8102	−49.5762	6.38	0.25	80 ± 17	0.58 ± 0.03	4.06 ± 0.83	3	
SPT-CL J0220−5445	35.1200	−54.7511	4.57	0.50	53 ± 13	> 0.81	···	2	
SPT-CL J0221−4446	35.4173	−44.7792	5.23	0.25	69 ± 18	0.56 ± 0.03	3.29 ± 0.81	6	
SPT-CL J0225−4327	36.2951	−43.4567	5.37	0.25	58 ± 12	0.23 ± 0.03	3.77 ± 0.88	6	c
SPT-CL J0225−4155	36.4770	−41.9177	6.92	1.75	93 ± 12	0.220	4.85 ± 0.94	5	c
SPT-CL J0230−6028	37.6418	−60.4689	6.01	0.25	73 ± 17	0.68 ± 0.06	3.59 ± 0.76	3, 10	
SPT-CL J0231−4427	37.7508	−44.4640	5.42	0.50	62 ± 14	0.62 ± 0.05	3.36 ± 0.79	6	
SPT-CL J0231−5403	37.7768	−54.0563	5.22	0.50	60 ± 13	0.59 ± 0.03	3.26 ± 0.81	6	
SPT-CL J0232−4421*	38.0701	−44.3541	23.96	1.00	254 ± 12	0.284	12.01 ± 1.80	6	
SPT-CL J0232−5257*	38.1876	−52.9578	8.65	0.75	96 ± 12	0.556	5.36 ± 0.94	5	
SPT-CL J0233−5819	38.2552	−58.3274	6.55	1.25	73 ± 11	0.663^+	3.93 ± 0.79	1	
SPT-CL J0234−5831*	38.6786	−58.5214	14.66	0.50	168 ± 14	0.415^+	8.05 ± 1.25	5	
SPT-CL J0235−5121*	38.9468	−51.3516	9.78	2.00	116 ± 18	0.278	6.41 ± 1.08	5	
SPT-CL J0236−4938	39.2477	−49.6356	5.80	1.00	67 ± 12	0.334	3.99 ± 0.86	1	
SPT-CL J0237−4151	39.4184	−41.8563	4.92	1.00	53 ± 12	0.40 ± 0.04	3.22 ± 0.86	5	b
SPT-CL J0238−4904	39.6994	−49.0710	5.77	1.00	62 ± 12	0.49 ± 0.04	3.78 ± 0.83	5	
SPT-CL J0240−5946	40.1606	−59.7697	8.84	0.75	100 ± 12	0.400^+	5.54 ± 0.96	3	
SPT-CL J0240−5952	40.1988	−59.8786	4.61	0.25	54 ± 17	0.59 ± 0.05	2.76 ± 0.77	5	b
SPT-CL J0242−4150	40.5347	−41.8360	5.04	0.50	60 ± 13	0.71 ± 0.03	2.99 ± 0.79	2	
SPT-CL J0242−4944	40.5470	−49.7376	6.25	0.25	83 ± 21	0.73 ± 0.06	3.79 ± 0.78	7, 10	
SPT-CL J0242−6039	40.6536	−60.6526	4.88	1.00	55 ± 12	> 1.50	···	2, 10	
SPT-CL J0243−5930*	40.8615	−59.5124	7.67	0.25	94 ± 20	0.635^+	4.58 ± 0.85	3	
SPT-CL J0243−4833	40.9139	−48.5602	13.90	0.75	153 ± 12	0.500^+	7.80 ± 1.22	1	a
SPT-CL J0244−4755	41.0159	−47.9274	4.79	0.25	68 ± 20	> 0.75	···	2	
SPT-CL J0244−4857	41.0310	−48.9606	5.93	1.75	72 ± 13	0.45 ± 0.04	3.93 ± 0.84	5	
SPT-CL J0249−5658	42.4065	−56.9770	5.45	1.00	60 ± 12	0.235	3.73 ± 0.85	1	c
SPT-CL J0250−4714	42.6656	−47.2385	4.50	1.25	60 ± 14	···	···	···	
SPT-CL J0252−4824*	43.1881	−48.4124	7.03	0.25	86 ± 14	0.421^+	4.79 ± 0.93	1	
SPT-CL J0253−6046	43.4619	−60.7725	4.93	1.25	50 ± 11	0.45 ± 0.03	3.11 ± 0.82	1	b
SPT-CL J0254−5857	43.5729	−58.9526	14.13	1.50	150 ± 12	0.438^+	7.79 ± 1.22	3	
SPT-CL J0254−6051	43.6007	−60.8641	6.55	1.00	70 ± 12	0.44 ± 0.03	4.21 ± 0.85	1	
SPT-CL J0256−4243	44.0543	−42.7329	5.09	0.75	63 ± 12	0.59 ± 0.03	3.15 ± 0.81	6	5
SPT-CL J0256−4221	44.0827	−42.3589	4.54	0.75	62 ± 19	> 0.85	···	3	
SPT-CL J0256−5617*	44.0997	−56.2980	7.45	0.50	87 ± 14	0.58 ± 0.03	4.54 ± 0.85	3	
SPT-CL J0256−4736	44.2405	−47.6110	7.04	0.75	77 ± 12	0.23 ± 0.03	4.94 ± 0.95	5	c
SPT-CL J0257−6050	44.3358	−60.8450	4.74	1.25	78 ± 16	0.51 ± 0.03	2.92 ± 0.80	2	b
SPT-CL J0257−5732	44.3506	−57.5426	5.04	0.25	60 ± 13	0.434^+	3.20 ± 0.82	1	
SPT-CL J0257−5842	44.3934	−58.7107	5.33	1.00	60 ± 12	0.44 ± 0.03	3.41 ± 0.81	1	
SPT-CL J0257−4817	44.4463	−48.2970	5.13	0.25	66 ± 14	0.46 ± 0.04	3.34 ± 0.84	5	
SPT-CL J0258−5355	44.5227	−53.9233	4.96	1.25	49 ± 12	0.93 ± 0.07	2.73 ± 0.74	2, 10	b
SPT-CL J0259−4556	44.9007	−45.9352	5.74	0.50	73 ± 13	0.36 ± 0.03	3.92 ± 0.85	1	
SPT-CL J0300−6315	45.1443	−63.2637	4.74	2.75	55 ± 15	> 1.50	···	1, 10	
SPT-CL J0301−4852	45.2509	−48.8687	4.53	0.25	67 ± 21	···	···	···	
SPT-CL J0301−6456	45.4770	−64.9473	4.93	0.25	60 ± 16	0.70 ± 0.03	2.85 ± 0.76	1	b
SPT-CL J0304−4921*	46.0619	−49.3612	12.75	1.25	134 ± 12	0.392	7.57 ± 1.20	5	a
SPT-CL J0304−4401*	46.0702	−44.0314	15.69	1.00	173 ± 15	0.458^+	8.55 ± 1.32	1	
SPT-CL J0304−4748	46.1503	−47.8115	6.38	0.25	76 ± 18	0.51 ± 0.03	4.15 ± 0.85	1	
SPT-CL J0304−5404	46.2161	−54.0750	4.84	0.25	60 ± 20	0.80 ± 0.06	2.78 ± 0.76	1, 10	b

TABLE 4 — *Continued*

SPT ID	R.A. (J2000)	Decl. (J2000)	Best ξ	Best θ_c	Y_{SZ} $\times 10^6$ (arcmin^2)	Redshift	M_{500c} ($10^{14} h_{70}^{-1} M_\odot$)	Imaging	Notes
SPT-CL J0306−4749	46.7450	−47.8179	4.74	0.50	60 ± 15	0.37 ± 0.03	3.13 ± 0.87	1	b
SPT-CL J0307−6225*	46.8336	−62.4327	8.46	0.75	91 ± 12	0.579^+	5.06 ± 0.90	4	a
SPT-CL J0307−4123	46.8782	−41.3903	5.22	1.00	55 ± 17	0.67 ± 0.04	3.15 ± 0.79	2	
SPT-CL J0307−5042*	46.9516	−50.7071	8.44	0.50	95 ± 13	0.55 ± 0.03	5.26 ± 0.93	1	a
SPT-CL J0309−4958	47.2623	−49.9741	5.66	0.50	64 ± 17	0.53 ± 0.04	3.66 ± 0.81	5	
SPT-CL J0310−4647	47.6291	−46.7834	7.12	0.50	80 ± 12	0.709^+	4.31 ± 0.83	5	a
SPT-CL J0311−6354	47.8289	−63.9073	7.16	1.00	74 ± 11	0.25 ± 0.02	4.83 ± 0.92	1	
SPT-CL J0313−5645	48.2620	−56.7548	4.53	0.75	51 ± 12	0.66 ± 0.03	2.65 ± 0.74	1	b
SPT-CL J0313−5334	48.4809	−53.5781	6.09	0.25	77 ± 21	1.37 ± 0.09	2.97 ± 0.64	2, 10	
SPT-CL J0314−6130	48.6096	−61.5104	4.63	0.25	52 ± 16	0.47 ± 0.03	2.88 ± 0.80	2	b
SPT-CL J0314−4019	48.6962	−40.3218	4.87	1.00	49 ± 11	0.68 ± 0.04	2.90 ± 0.79	6	b
SPT-CL J0315−4359	48.8267	−43.9974	4.80	0.25	69 ± 21	> 0.93	···	2	
SPT-CL J0317−5935	49.3216	−59.5851	6.26	0.25	70 ± 16	0.469^+	4.00 ± 0.82	1	
SPT-CL J0317−4849	49.4530	−48.8267	4.94	1.50	58 ± 15	0.164	3.50 ± 0.91	5	b,c
SPT-CL J0319−5212	49.8478	−52.2027	4.76	0.50	56 ± 20	> 1.50	···	3, 10	
SPT-CL J0319−5417	49.9524	−54.2939	4.58	3.00	46 ± 14	> 0.72	···	6	
SPT-CL J0320−5800	50.0310	−58.0098	4.72	2.25	44 ± 12	> 0.77	···	2	
SPT-CL J0321−4846	50.3243	−48.7743	4.66	0.25	59 ± 15	···	···	···	
SPT-CL J0322−4335	50.6604	−43.5917	4.97	1.50	53 ± 12	> 0.85	···	2	6
SPT-CL J0323−4913	50.9166	−49.2215	4.54	0.50	46 ± 12	> 1.50	···	2, 10	7
SPT-CL J0324−6236*	51.0530	−62.6021	8.75	0.50	96 ± 12	0.73 ± 0.03	4.97 ± 0.86	3	
SPT-CL J0325−5132	51.3391	−51.5435	4.54	0.25	56 ± 17	> 0.74	···	2	
SPT-CL J0326−5054	51.7198	−50.9102	4.62	0.50	52 ± 19	···	···	···	
SPT-CL J0327−4633	51.7651	−46.5600	4.67	0.25	66 ± 19	> 1.50	···	2, 10	
SPT-CL J0328−5541	52.1675	−55.6957	7.32	1.25	81 ± 12	0.084	5.14 ± 0.97	1	c
SPT-CL J0329−4029	52.2594	−40.4867	4.85	0.25	66 ± 21	> 0.87	···	2	
SPT-CL J0330−5228	52.7287	−52.4698	11.57	1.50	120 ± 11	0.442	6.67 ± 1.08	1	5,a
SPT-CL J0332−4100	53.0340	−41.0113	4.54	0.50	61 ± 21	···	···	···	
SPT-CL J0332−5304	53.1652	−53.0758	4.66	0.50	42 ± 13	0.51 ± 0.03	2.84 ± 0.79	7	b
SPT-CL J0333−5842	53.3185	−58.7025	4.67	1.50	52 ± 11	0.40 ± 0.04	2.97 ± 0.83	5	b
SPT-CL J0334−4659*	53.5464	−46.9932	9.20	1.00	96 ± 11	0.485^+	5.52 ± 0.95	5	
SPT-CL J0334−4645	53.6800	−46.7629	4.83	1.00	49 ± 11	≥ 1.50	2.07 ± 0.47	2, 10	b,d
SPT-CL J0334−4815	53.7097	−48.2638	7.22	0.25	86 ± 16	0.59 ± 0.03	4.36 ± 0.83	1	
SPT-CL J0336−4704	54.1214	−47.0692	5.96	0.75	63 ± 11	0.89 ± 0.07	3.29 ± 0.70	2, 9	
SPT-CL J0336−4005	54.1568	−40.0972	5.10	1.75	50 ± 12	0.52 ± 0.04	3.24 ± 0.83	5	
SPT-CL J0337−4442	54.2698	−44.7105	4.84	1.50	60 ± 14	> 0.88	···	2	
SPT-CL J0337−4928	54.4573	−49.4738	5.57	1.50	60 ± 12	0.53 ± 0.03	3.45 ± 0.78	1	
SPT-CL J0337−6300	54.4692	−63.0103	5.16	0.25	55 ± 16	0.48 ± 0.03	3.24 ± 0.81	1	
SPT-CL J0337−6207	54.4708	−62.1175	5.03	1.75	56 ± 14	> 1.30	···	1, 8	
SPT-CL J0338−4013	54.5310	−40.2286	4.69	0.25	60 ± 21	> 1.50	···	2, 10	
SPT-CL J0338−4711	54.6938	−47.1882	4.62	1.25	49 ± 12	···	···	···	
SPT-CL J0339−3952	54.7862	−39.8734	5.45	0.25	14 ± 3	> 0.59	···	6	8
SPT-CL J0339−4545	54.8908	−45.7535	5.34	0.75	58 ± 11	0.75 ± 0.06	3.05 ± 0.74	7	
SPT-CL J0341−5027	55.2802	−50.4611	4.75	1.25	49 ± 11	0.39 ± 0.04	3.00 ± 0.82	5	b
SPT-CL J0341−6143	55.3487	−61.7193	5.68	3.00	88 ± 16	0.65 ± 0.03	3.42 ± 0.76	1	
SPT-CL J0341−5731	55.3981	−57.5238	5.27	0.25	67 ± 17	0.67 ± 0.03	3.11 ± 0.76	1	
SPT-CL J0342−5354	55.5220	−53.9118	5.54	1.00	56 ± 11	0.53 ± 0.03	3.43 ± 0.78	1	
SPT-CL J0342−4028	55.5604	−40.4785	6.91	0.50	79 ± 11	0.50 ± 0.04	4.46 ± 0.87	5	
SPT-CL J0343−5518	55.7617	−55.3032	6.01	0.25	71 ± 17	0.55 ± 0.03	3.75 ± 0.79	1	
SPT-CL J0344−5452	56.0922	−54.8794	7.98	0.25	97 ± 23	1.01 ± 0.07	4.17 ± 0.75	1, 10	
SPT-CL J0344−5518	56.2068	−55.3018	5.18	0.75	85 ± 36	0.32 ± 0.03	3.43 ± 0.84	1	
SPT-CL J0345−6419	56.2510	−64.3326	5.54	0.25	60 ± 15	0.91 ± 0.07	3.04 ± 0.71	1, 10	
SPT-CL J0346−5839	56.5733	−58.6531	4.83	0.25	55 ± 11	0.68 ± 0.06	2.81 ± 0.76	1, 10	b
SPT-CL J0346−5439*	56.7247	−54.6505	9.25	0.75	95 ± 11	0.530	5.47 ± 0.94	1	
SPT-CL J0348−4515*	57.0737	−45.2510	10.12	0.75	105 ± 12	0.358^+	6.17 ± 1.03	1	a
SPT-CL J0350−4620	57.7216	−46.3342	6.44	0.25	72 ± 11	0.79 ± 0.04	3.67 ± 0.75	7	
SPT-CL J0351−4109	57.7545	−41.1566	9.05	1.25	101 ± 11	0.68 ± 0.04	5.32 ± 0.91	6	
SPT-CL J0351−5636	57.9324	−56.6132	4.51	0.75	55 ± 11	0.38 ± 0.03	2.88 ± 0.82	1	b
SPT-CL J0352−5647*	58.2367	−56.7996	7.13	0.75	78 ± 12	0.67 ± 0.03	4.24 ± 0.81	3	
SPT-CL J0353−4818	58.2639	−48.3160	4.90	1.75	47 ± 11	> 0.96	···	3	
SPT-CL J0353−5312	58.3058	−53.2095	4.54	0.25	51 ± 15	···	···	···	
SPT-CL J0353−5043	58.3853	−50.7278	5.35	0.25	65 ± 19	> 0.82	···	7	
SPT-CL J0354−5904	58.5612	−59.0733	6.42	1.25	71 ± 11	0.41 ± 0.03	4.17 ± 0.85	1	
SPT-CL J0354−5151	58.6584	−51.8589	5.82	0.25	67 ± 17	0.62 ± 0.04	3.51 ± 0.76	7	
SPT-CL J0354−4058	58.6720	−40.9805	4.92	0.25	68 ± 20	0.86 ± 0.07	2.75 ± 0.75	2, 10	b

TABLE 4 — *Continued*

SPT ID	R.A. (J2000)	Decl. (J2000)	Best ξ	Best θ_c	Y_{SZ} $\times 10^6$ (arcmin^2)	Redshift	M_{500c} ($10^{14} h_{70}^{-1} M_\odot$)	Imaging	Notes
SPT-CL J0354−6032	58.6727	−60.5380	4.68	0.25	59 ± 20	1.10 ± 0.08	2.38 ± 0.63	2, 10	b
SPT-CL J0356−5337	59.0855	−53.6331	6.02	0.25	77 ± 17	0.90 ± 0.07	3.31 ± 0.70	7, 10	a
SPT-CL J0357−4521	59.3670	−45.3502	4.97	1.00	48 ± 11	1.03 ± 0.15	2.55 ± 0.67	2	b
SPT-CL J0359−5218	59.8362	−52.3157	6.27	0.75	65 ± 14	0.58 ± 0.06	3.83 ± 0.79	7	
SPT-CL J0402−4611	60.5770	−46.1891	5.53	1.25	61 ± 11	0.32 ± 0.04	3.66 ± 0.83	5	
SPT-CL J0402−6130	60.7065	−61.5002	4.79	0.50	59 ± 11	0.51 ± 0.04	2.95 ± 0.80	5	b
SPT-CL J0403−5535	60.9467	−55.5838	4.86	1.75	66 ± 13	> 1.50	···	1, 10	
SPT-CL J0403−5719	60.9681	−57.3237	5.86	0.25	64 ± 16	0.466^+	3.75 ± 0.81	1	a
SPT-CL J0404−6510	61.0547	−65.1820	4.71	2.25	56 ± 31	0.12 ± 0.03	3.25 ± 0.90	5	b,c
SPT-CL J0404−4418	61.1978	−44.3044	7.40	0.25	98 ± 25	0.87 ± 0.07	4.22 ± 0.79	2, 10	
SPT-CL J0405−4648	61.2861	−46.8111	6.63	1.00	72 ± 11	0.39 ± 0.03	4.29 ± 0.85	1	
SPT-CL J0405−4916	61.4917	−49.2709	7.17	0.75	76 ± 12	0.32 ± 0.04	4.70 ± 0.90	5	
SPT-CL J0406−5118	61.6755	−51.3053	4.54	0.25	57 ± 18	···	···	···	
SPT-CL J0406−5455	61.6906	−54.9210	5.91	0.25	73 ± 19	0.74 ± 0.03	3.46 ± 0.75	1	
SPT-CL J0406−4805*	61.7275	−48.0866	8.13	1.00	86 ± 12	0.737^+	4.61 ± 0.83	7	
SPT-CL J0408−4456	62.0918	−44.9388	4.60	0.50	56 ± 12	0.57 ± 0.20	2.83 ± 0.80	10	b
SPT-CL J0410−6343	62.5170	−63.7275	5.61	0.50	62 ± 13	0.52 ± 0.03	3.52 ± 0.79	1	
SPT-CL J0410−5454	62.6148	−54.9010	4.79	0.25	69 ± 21	> 1.50	···	1, 10	
SPT-CL J0411−4819*	62.8154	−48.3218	15.26	1.00	159 ± 12	0.424^+	8.18 ± 1.27	5	a
SPT-CL J0411−6340	62.8597	−63.6804	6.35	0.25	69 ± 12	0.14 ± 0.01	4.46 ± 0.91	1	c
SPT-CL J0412−5743	63.0248	−57.7201	5.30	1.25	58 ± 11	0.34 ± 0.03	3.50 ± 0.84	1	
SPT-CL J0412−5106	63.2297	−51.1098	5.15	0.25	56 ± 13	0.28 ± 0.04	3.42 ± 0.84	5	
SPT-CL J0415−4621	63.9239	−46.3562	4.85	0.50	60 ± 20	> 0.83	···	2	
SPT-CL J0416−4938	64.1380	−49.6358	4.71	2.75	43 ± 14	> 0.92	···	2	
SPT-CL J0416−6359	64.1630	−63.9964	6.10	0.50	64 ± 12	0.32 ± 0.02	4.08 ± 0.85	1	
SPT-CL J0417−4748*	64.3451	−47.8139	14.24	0.25	172 ± 26	0.581^+	7.41 ± 1.15	1	
SPT-CL J0417−4427	64.4097	−44.4640	9.13	0.50	105 ± 14	0.43 ± 0.04	5.78 ± 0.99	7	
SPT-CL J0418−4552	64.6693	−45.8820	5.51	0.75	59 ± 11	0.71 ± 0.06	3.20 ± 0.74	7, 10	
SPT-CL J0420−5245	65.0007	−52.7512	4.54	0.25	60 ± 20	···	···	···	
SPT-CL J0421−4845	65.3206	−48.7612	5.82	0.25	77 ± 20	1.42 ± 0.09	2.68 ± 0.60	3, 10	
SPT-CL J0422−5140	65.5923	−51.6755	5.86	1.00	59 ± 13	0.59 ± 0.03	3.57 ± 0.77	2	
SPT-CL J0422−4608	65.7490	−46.1436	5.05	0.50	56 ± 15	0.70 ± 0.03	2.90 ± 0.75	2	
SPT-CL J0423−6143	65.9352	−61.7177	4.63	0.25	59 ± 15	0.52 ± 0.04	2.84 ± 0.79	5	b
SPT-CL J0424−4406	66.0045	−44.1107	6.39	0.75	68 ± 12	0.43 ± 0.04	4.24 ± 0.86	5	
SPT-CL J0426−5455*	66.5199	−54.9197	8.85	0.50	108 ± 12	0.63 ± 0.03	5.17 ± 0.90	4	
SPT-CL J0426−5416	66.6764	−54.2763	4.62	0.25	57 ± 19	1.05 ± 0.07	2.37 ± 0.63	2, 10	b
SPT-CL J0428−6049	67.0305	−60.8292	5.11	1.25	54 ± 12	0.64 ± 0.03	3.04 ± 0.78	1	
SPT-CL J0429−4355	67.3073	−43.9300	4.94	1.25	66 ± 16	0.38 ± 0.04	3.26 ± 0.86	5	b
SPT-CL J0429−5233	67.4315	−52.5609	4.56	0.75	46 ± 11	0.53 ± 0.03	2.75 ± 0.77	2	b
SPT-CL J0430−6251	67.7094	−62.8548	5.29	0.25	59 ± 12	> 1.50	···	1, 10	9
SPT-CL J0431−6126	67.8417	−61.4350	6.19	2.50	176 ± 26	0.058	4.44 ± 0.92	1	c
SPT-CL J0432−6150	68.0525	−61.8497	4.52	0.25	54 ± 19	0.98 ± 0.07	2.39 ± 0.65	2, 10	b
SPT-CL J0433−5630	68.2541	−56.5025	5.32	1.75	58 ± 12	0.692^+	3.13 ± 0.76	1	
SPT-CL J0437−5307	69.2599	−53.1206	4.52	0.25	54 ± 19	> 0.44	···	7	
SPT-CL J0438−5419*	69.5749	−54.3212	22.88	0.50	237 ± 11	0.421	10.80 ± 1.62	1	
SPT-CL J0439−4600	69.8087	−46.0142	8.28	0.25	97 ± 13	0.34 ± 0.04	5.29 ± 0.94	5	
SPT-CL J0439−5330	69.9290	−53.5038	5.61	0.75	60 ± 13	0.43 ± 0.04	3.59 ± 0.80	5	
SPT-CL J0440−4657	70.2307	−46.9654	7.13	1.25	79 ± 11	0.35 ± 0.04	4.63 ± 0.89	5	
SPT-CL J0441−4855*	70.4511	−48.9190	8.56	0.50	92 ± 13	0.79 ± 0.04	4.74 ± 0.83	1	a
SPT-CL J0442−4309	70.6940	−43.1528	4.63	1.50	43 ± 12	> 0.74	···	3	
SPT-CL J0442−6138	70.7489	−61.6418	4.55	0.25	55 ± 19	1.16 ± 0.08	2.28 ± 0.60	2, 10	b
SPT-CL J0444−5603	71.1136	−56.0576	5.18	0.25	71 ± 21	0.97 ± 0.07	2.75 ± 0.70	1, 10	
SPT-CL J0444−4352	71.1683	−43.8735	5.01	1.50	57 ± 18	0.57 ± 0.03	3.11 ± 0.82	6	
SPT-CL J0445−4926	71.2663	−49.4336	4.65	0.50	45 ± 18	···	···	···	
SPT-CL J0445−4230	71.2775	−42.5087	7.07	0.75	79 ± 12	0.37 ± 0.03	4.74 ± 0.91	7	
SPT-CL J0446−5849	71.5156	−58.8228	7.18	0.25	90 ± 13	1.19 ± 0.08	3.61 ± 0.69	1, 10	
SPT-CL J0446−4606	71.7325	−46.1012	5.71	0.25	77 ± 21	≥ 1.50	2.40 ± 0.54	2, 10	d
SPT-CL J0447−5041	71.7821	−50.6991	4.62	2.00	51 ± 18	> 0.87	···	3	
SPT-CL J0447−5055	71.8445	−50.9227	5.96	0.25	65 ± 12	0.39 ± 0.05	3.87 ± 0.82	5	
SPT-CL J0448−4036	72.0160	−40.6031	4.66	0.25	59 ± 21	> 0.88	···	3	
SPT-CL J0448−4332	72.1315	−43.5387	4.67	0.25	57 ± 18	0.79 ± 0.10	2.67 ± 0.75	7	b
SPT-CL J0449−4901*	72.2742	−49.0246	8.91	0.50	96 ± 12	0.792^+	4.90 ± 0.85	1	
SPT-CL J0451−4952	72.9661	−49.8796	4.90	0.25	56 ± 12	0.39 ± 0.04	3.12 ± 0.83	5	10,b
SPT-CL J0452−4806	73.0034	−48.1102	4.52	0.50	49 ± 12	0.37 ± 0.04	2.87 ± 0.81	5	b
SPT-CL J0452−4002	73.0950	−40.0394	4.66	0.25	67 ± 22	···	···	···	

TABLE 4 — *Continued*

SPT ID	R.A. (J2000)	Decl. (J2000)	Best ξ	Best θ_c	Y_{SZ} $\times 10^6$ (arcmin^2)	Redshift	M_{500c} ($10^{14} h_{70}^{-1} M_\odot$)	Imaging	Notes
SPT-CL J0454−4211	73.7352	−42.1839	6.69	0.25	87 ± 20	0.69 ± 0.06	4.07 ± 0.81	7, 10	
SPT-CL J0455−4159	73.9973	−41.9931	5.09	0.75	55 ± 14	0.31 ± 0.04	3.46 ± 0.87	5	
SPT-CL J0456−5116*	74.1163	−51.2768	8.58	1.00	90 ± 11	0.562^+	5.09 ± 0.89	1	
SPT-CL J0456−4906	74.1212	−49.1056	5.99	0.25	63 ± 12	0.93 ± 0.07	3.26 ± 0.70	7, 10	
SPT-CL J0456−6141	74.1475	−61.6838	4.80	0.25	56 ± 13	0.37 ± 0.04	3.08 ± 0.84	5	b
SPT-CL J0456−5623	74.1753	−56.3855	4.60	0.25	56 ± 17	0.66 ± 0.03	2.69 ± 0.75	2	b
SPT-CL J0458−5741	74.6033	−57.6959	4.87	2.50	60 ± 13	0.19 ± 0.02	3.32 ± 0.88	2	b,c
SPT-CL J0459−4947	74.9269	−49.7872	6.29	0.25	73 ± 16	≥ 1.50	2.67 ± 0.55	2, 10	d
SPT-CL J0500−4713	75.1198	−47.2293	4.92	0.75	52 ± 12	> 0.69	···	2	
SPT-CL J0500−4551	75.2108	−45.8564	4.51	0.75	58 ± 13	···	···	···	
SPT-CL J0500−5116	75.2425	−51.2709	5.92	1.50	58 ± 12	0.11 ± 0.03	4.16 ± 0.88	5	c
SPT-CL J0501−4455	75.2932	−44.9270	4.59	0.25	63 ± 22	···	···	···	
SPT-CL J0502−6113	75.5450	−61.2321	5.11	0.50	57 ± 12	0.68 ± 0.04	2.99 ± 0.77	1, 8	
SPT-CL J0502−6048	75.7229	−60.8112	4.69	0.25	70 ± 20	> 0.90	···	2	
SPT-CL J0504−4929	76.0069	−49.4854	5.33	0.75	59 ± 13	0.20 ± 0.03	4.03 ± 0.95	5	c
SPT-CL J0505−4204	76.3681	−42.0811	4.67	1.50	57 ± 15	0.38 ± 0.03	3.26 ± 0.93	2	b
SPT-CL J0505−6145	76.3966	−61.7505	6.90	1.25	80 ± 12	0.25 ± 0.03	4.84 ± 0.94	5	
SPT-CL J0508−6149	77.1637	−61.8188	4.86	1.00	54 ± 12	0.33 ± 0.04	3.28 ± 0.89	7	b
SPT-CL J0509−5342*	77.3374	−53.7053	8.50	0.75	92 ± 12	0.461	5.06 ± 0.89	2	a
SPT-CL J0509−6118	77.4741	−61.3067	10.37	1.00	118 ± 12	0.35 ± 0.03	6.60 ± 1.09	1	
SPT-CL J0510−4519	77.5805	−45.3270	9.50	1.00	116 ± 12	0.20	6.83 ± 1.16	5	c
SPT-CL J0511−5154	77.9209	−51.9044	7.09	0.25	79 ± 16	0.645^+	4.09 ± 0.79	2	
SPT-CL J0512−5139	78.1587	−51.6621	6.21	1.00	64 ± 11	0.60 ± 0.03	3.66 ± 0.76	1	
SPT-CL J0516−6312	79.0861	−63.2083	4.77	0.50	15 ± 5	0.14 ± 0.06	3.40 ± 0.93	6	11,b,c
SPT-CL J0516−5430*	79.1513	−54.5108	12.41	1.50	153 ± 12	0.295^+	7.10 ± 1.14	2	
SPT-CL J0516−5755	79.2398	−57.9167	5.73	0.75	59 ± 12	0.94 ± 0.11	3.01 ± 0.67	2	
SPT-CL J0517−6119	79.2844	−61.3181	7.16	0.25	99 ± 23	0.75 ± 0.06	4.30 ± 0.82	2, 10	
SPT-CL J0517−6311	79.4094	−63.1989	5.15	0.50	65 ± 12	0.32 ± 0.06	3.53 ± 0.88	6	11
SPT-CL J0519−4248	79.8535	−42.8066	4.69	0.50	64 ± 14	0.59 ± 0.03	3.05 ± 0.87	3	b
SPT-CL J0521−5104	80.3012	−51.0766	7.22	1.00	76 ± 11	0.675	4.12 ± 0.78	1	
SPT-CL J0522−5026	80.5159	−50.4394	5.20	1.75	53 ± 13	0.52 ± 0.03	3.11 ± 0.76	2	
SPT-CL J0522−4818	80.5667	−48.3025	4.82	0.50	54 ± 15	0.296	3.48 ± 0.95	5	b
SPT-CL J0524−4037	81.2091	−40.6238	4.65	1.50	58 ± 22	> 0.89	···	2	
SPT-CL J0525−4715	81.4555	−47.2556	10.14	1.00	115 ± 12	0.191	7.20 ± 1.20	1	c
SPT-CL J0526−5018	81.5087	−50.3147	4.90	0.50	47 ± 11	0.58 ± 0.03	2.85 ± 0.75	2	b
SPT-CL J0528−5300*	82.0196	−53.0024	6.55	0.50	74 ± 12	0.768	3.65 ± 0.73	2	
SPT-CL J0528−4417	82.0610	−44.2922	5.09	1.75	54 ± 13	0.69 ± 0.03	3.24 ± 0.85	2	
SPT-CL J0529−6051	82.3493	−60.8578	5.58	0.50	71 ± 18	0.72 ± 0.06	3.39 ± 0.78	7, 10	
SPT-CL J0529−5322	82.4732	−53.3741	4.71	0.25	57 ± 18	> 0.93	···	1	
SPT-CL J0529−4138	82.4857	−41.6365	6.24	0.50	78 ± 13	0.65 ± 0.06	4.14 ± 0.86	2, 10	
SPT-CL J0530−4139	82.6754	−41.6502	6.19	0.25	83 ± 22	0.73 ± 0.03	4.00 ± 0.83	2	
SPT-CL J0532−5450	83.0307	−54.8445	5.24	0.25	57 ± 15	0.43 ± 0.03	3.23 ± 0.78	1	
SPT-CL J0533−5005*	83.4009	−50.0901	7.08	0.25	84 ± 20	0.881^+	3.79 ± 0.73	2	
SPT-CL J0534−5937	83.6082	−59.6257	4.74	0.25	53 ± 15	0.576^+	2.75 ± 0.75	2	b
SPT-CL J0534−4847	83.6655	−48.7965	4.59	0.25	69 ± 21	···	···	···	
SPT-CL J0535−5956	83.7934	−59.9394	5.20	0.25	59 ± 17	0.58 ± 0.03	3.05 ± 0.75	3	
SPT-CL J0535−4801	83.9464	−48.0229	6.34	0.25	85 ± 22	0.90 ± 0.07	3.87 ± 0.80	2, 10	
SPT-CL J0536−6109	84.1630	−61.1543	6.39	0.25	88 ± 22	1.05 ± 0.08	3.50 ± 0.71	2, 10	
SPT-CL J0537−6504	84.3548	−65.0695	10.54	0.75	121 ± 12	0.20 ± 0.10	6.96 ± 1.15	1	11,c
SPT-CL J0539−6013	84.9561	−60.2272	5.05	1.75	54 ± 15	> 0.74	···	1	
SPT-CL J0540−5744	85.0043	−57.7405	6.74	0.25	78 ± 18	0.76 ± 0.03	3.76 ± 0.74	3	a
SPT-CL J0542−4100*	85.7167	−41.0044	7.92	0.75	97 ± 12	0.642	5.16 ± 0.94	2	
SPT-CL J0543−6219	85.7564	−62.3252	8.21	0.75	94 ± 13	0.38 ± 0.06	5.43 ± 0.97	1	11
SPT-CL J0543−4250	85.9447	−42.8379	6.67	1.50	83 ± 15	0.59 ± 0.05	4.50 ± 0.89	5	
SPT-CL J0544−3950	86.2456	−39.8453	6.32	0.75	104 ± 13	0.45 ± 0.04	4.47 ± 0.91	7	
SPT-CL J0545−5052	86.4957	−50.8814	4.60	0.50	53 ± 15	> 0.68	···	3	
SPT-CL J0546−4752	86.5513	−47.8819	4.82	0.50	62 ± 12	0.46 ± 0.03	3.30 ± 0.91	2	b
SPT-CL J0546−3952	86.5974	−39.8687	4.70	0.25	69 ± 20	> 0.72	···	2	
SPT-CL J0546−5345*	86.6525	−53.7625	10.76	0.50	120 ± 14	1.066	5.05 ± 0.82	1	a
SPT-CL J0546−6040	86.7342	−60.6723	4.72	0.75	61 ± 17	> 0.85	···	3	
SPT-CL J0547−5026	86.7782	−50.4400	4.76	1.25	56 ± 11	0.60 ± 0.03	2.74 ± 0.75	1	b
SPT-CL J0548−4340	87.2419	−43.6819	4.59	2.75	59 ± 15	···	···	···	
SPT-CL J0549−6205	87.3344	−62.0858	25.81	0.25	301 ± 15	0.376^+	12.40 ± 1.85	1	
SPT-CL J0550−5019	87.5504	−50.3236	4.91	0.25	55 ± 11	0.65 ± 0.03	2.79 ± 0.74	1	b
SPT-CL J0550−6358	87.6825	−63.9746	5.53	0.25	68 ± 19	0.67 ± 0.03	3.41 ± 0.79	2	11

TABLE 4 — *Continued*

SPT ID	R.A. (J2000)	Decl. (J2000)	Best ξ	Best θ_c	Y_{SZ} $\times 10^6$ (arcmin^2)	Redshift	M_{500c} ($10^{14} h_{70}^{-1} M_\odot$)	Imaging	Notes
SPT-CL J0551−4940	87.8615	−49.6736	4.54	0.25	59 ± 21	···	···	···	
SPT-CL J0551−4339	87.8798	−43.6596	6.00	0.75	71 ± 13	0.35 ± 0.03	4.37 ± 0.93	2	
SPT-CL J0551−5709	87.9041	−57.1557	8.21	0.50	83 ± 11	0.423^+	4.97 ± 0.89	2	
SPT-CL J0552−4937	88.1783	−49.6208	5.05	0.25	65 ± 22	> 1.50	···	2, 10	
SPT-CL J0555−6406*	88.8662	−64.1032	12.72	1.25	142 ± 12	0.345^+	7.69 ± 1.22	1	11
SPT-CL J0556−5403	89.2026	−54.0609	5.77	0.25	70 ± 18	0.93 ± 0.06	3.05 ± 0.67	2	
SPT-CL J0557−5116	89.3385	−51.2695	4.93	0.50	57 ± 12	0.92 ± 0.09	2.56 ± 0.67	3, 9	b
SPT-CL J0557−4113	89.4557	−41.2310	5.37	0.75	64 ± 14	0.90 ± 0.07	3.21 ± 0.80	2, 10	
SPT-CL J0559−5249*	89.9251	−52.8260	10.64	1.00	105 ± 11	0.609^+	5.78 ± 0.95	2	
SPT-CL J0559−6022	89.9419	−60.3832	5.67	0.25	80 ± 23	> 1.50	···	2, 10	
SPT-CL J0600−4104	90.0348	−41.0701	4.70	0.25	56 ± 19	> 0.85	···	2	
SPT-CL J0600−4353	90.0614	−43.8879	6.85	0.75	77 ± 14	0.36 ± 0.04	4.95 ± 0.97	5	
SPT-CL J0601−5204	90.2515	−52.0797	4.54	1.50	41 ± 12	···	···	···	
SPT-CL J0601−4122	90.4988	−41.3699	4.71	1.00	48 ± 14	0.23 ± 0.02	3.30 ± 0.92	3	b,c
SPT-CL J0603−4714	90.9883	−47.2379	7.65	1.75	84 ± 12	0.32 ± 0.04	5.26 ± 0.97	5	5
SPT-CL J0604−4317	91.0007	−43.2853	4.56	2.75	52 ± 13	···	···	···	
SPT-CL J0604−4144	91.0115	−41.7445	4.69	0.25	66 ± 19	> 0.87	···	3	
SPT-CL J0607−4448	91.8984	−44.8033	6.44	0.25	91 ± 24	1.43 ± 0.09	3.14 ± 0.64	7, 10	
SPT-CL J0611−6000	92.7794	−60.0087	4.68	1.00	50 ± 12	> 0.60	···	3	
SPT-CL J0611−5938	92.8068	−59.6412	4.74	2.00	54 ± 12	0.39 ± 0.03	3.16 ± 0.88	6	b
SPT-CL J0611−4724	92.9212	−47.4111	5.61	0.25	65 ± 16	0.49 ± 0.03	3.73 ± 0.84	2	
SPT-CL J0612−4317	93.0249	−43.2992	6.14	1.75	74 ± 13	0.54 ± 0.05	4.02 ± 0.84	7	
SPT-CL J0613−5627	93.4558	−56.4597	7.04	0.25	100 ± 14	0.73 ± 0.03	4.31 ± 0.83	2	12
SPT-CL J0615−5746	93.9650	−57.7763	26.42	0.25	310 ± 15	0.972^+	10.53 ± 1.55	2	a
SPT-CL J0616−4407	94.0685	−44.1223	5.62	0.25	73 ± 20	0.70 ± 0.03	3.47 ± 0.79	2	
SPT-CL J0617−5507	94.2808	−55.1321	5.53	0.25	80 ± 14	0.87 ± 0.07	3.21 ± 0.75	2, 10	
SPT-CL J0619−5802	94.9221	−58.0382	6.29	0.25	76 ± 17	0.54 ± 0.03	4.11 ± 0.84	2	
SPT-CL J0620−4715	95.0965	−47.2591	5.22	0.75	62 ± 13	0.23 ± 0.03	3.72 ± 0.90	6	c
SPT-CL J0622−4645	95.7104	−46.7658	5.18	0.25	68 ± 19	0.65 ± 0.03	3.21 ± 0.81	2	
SPT-CL J0623−5035	95.8754	−50.5998	4.53	1.25	45 ± 12	···	···	···	
SPT-CL J0625−6335	96.2651	−63.5892	4.65	1.75	57 ± 12	> 1.50	···	10	
SPT-CL J0625−4728	96.4341	−47.4819	4.52	0.50	53 ± 18	···	···	···	
SPT-CL J0625−4330	96.4382	−43.5003	5.18	0.25	75 ± 18	0.57 ± 0.04	3.30 ± 0.83	7	
SPT-CL J0626−4446	96.7411	−44.7748	6.03	1.75	69 ± 13	0.41 ± 0.06	4.12 ± 0.86	7	
SPT-CL J0628−4143	97.2049	−41.7250	13.89	0.75	166 ± 12	0.176	8.67 ± 1.36	1	c
SPT-CL J0630−4521	97.5640	−45.3665	4.52	0.50	57 ± 21	···	···	···	
SPT-CL J0633−4854	98.3623	−48.9001	4.67	0.75	53 ± 16	> 0.68	···	2	
SPT-CL J0633−4413	98.4084	−44.2232	4.54	0.25	62 ± 22	···	···	···	
SPT-CL J0636−4942	99.1686	−49.7034	7.40	1.00	79 ± 12	0.35 ± 0.03	5.06 ± 0.95	2	
SPT-CL J0637−6112	99.2600	−61.2064	5.10	0.25	66 ± 21	> 1.50	···	7, 10	
SPT-CL J0637−4327	99.2774	−43.4513	5.10	3.00	63 ± 14	> 1.50	···	2, 10	
SPT-CL J0637−4829	99.3467	−48.4877	10.00	2.75	128 ± 19	0.203	6.76 ± 1.13	1	c
SPT-CL J0637−4750	99.4368	−47.8415	4.53	0.25	67 ± 21	···	···	···	
SPT-CL J0638−4243	99.5705	−42.7183	4.67	0.50	54 ± 13	0.35 ± 0.06	3.15 ± 0.89	7	b
SPT-CL J0638−5358	99.6978	−53.9749	22.69	0.75	261 ± 13	0.226	12.01 ± 1.81	6	c
SPT-CL J0640−5113	100.0645	−51.2204	6.86	0.50	83 ± 13	1.25 ± 0.08	3.55 ± 0.70	2, 10	
SPT-CL J0641−4733	100.2895	−47.5657	7.13	0.25	86 ± 21	0.64 ± 0.06	4.48 ± 0.86	1, 10	
SPT-CL J0641−5950	100.3788	−59.8490	7.11	0.75	79 ± 12	0.51 ± 0.03	4.66 ± 0.89	2	
SPT-CL J0641−5001	100.4587	−50.0171	4.53	0.50	59 ± 13	0.123	3.26 ± 0.93	7	b,c
SPT-CL J0642−6310	100.6961	−63.1750	4.89	0.50	58 ± 13	> 0.88	···	2	
SPT-CL J0643−4535	100.9332	−45.5978	5.05	0.25	71 ± 19	0.87 ± 0.07	2.88 ± 0.77	2, 10	
SPT-CL J0643−5056	100.9550	−50.9486	5.03	0.75	66 ± 21	> 1.50	···	3, 10	
SPT-CL J0645−5413	101.3735	−54.2214	18.32	1.25	218 ± 12	0.164	10.55 ± 1.61	···	c
SPT-CL J0646−6236	101.6391	−62.6136	8.67	0.25	110 ± 16	1.20 ± 0.10	4.40 ± 0.77	2	12
SPT-CL J0647−5828	101.9843	−58.4801	6.26	1.00	64 ± 12	0.46 ± 0.04	4.20 ± 0.86	5	
SPT-CL J0648−4622	102.1254	−46.3754	4.95	0.25	63 ± 22	1.29 ± 0.08	2.45 ± 0.65	2, 10	b
SPT-CL J0649−4510	102.4473	−45.1685	5.19	1.50	52 ± 13	0.44 ± 0.05	3.46 ± 0.86	7	
SPT-CL J0650−4503	102.6815	−45.0641	9.25	0.25	112 ± 15	0.41 ± 0.04	6.00 ± 1.03	5	
SPT-CL J0651−4037	102.8193	−40.6273	6.67	1.50	75 ± 12	0.27 ± 0.02	4.72 ± 0.94	2	
SPT-CL J0652−4133	103.1063	−41.5651	4.73	0.25	61 ± 21	> 0.64	···	2	
SPT-CL J0653−5744	103.3316	−57.7490	7.70	1.25	83 ± 12	0.24 ± 0.03	5.41 ± 1.00	5	c
SPT-CL J0655−4429	103.7630	−44.4837	4.71	0.25	62 ± 16	0.34 ± 0.05	3.18 ± 0.89	7	b
SPT-CL J0655−4135	103.7824	−41.5956	4.68	3.00	51 ± 14	> 0.67	···	2	
SPT-CL J0655−5541	103.9137	−55.6931	5.64	1.00	76 ± 12	0.29 ± 0.04	3.98 ± 0.88	5	
SPT-CL J0655−5234*	103.9626	−52.5677	7.76	0.50	90 ± 15	0.470^+	5.10 ± 0.93	3	

TABLE 4 — *Continued*

SPT ID	R.A. (J2000)	Decl. (J2000)	Best ξ	Best θ_c	Y_{SZ} $\times 10^6$ (arcmin^2)	Redshift	M_{500c} ($10^{14} h_{70}^{-1} M_\odot$)	Imaging	Notes
SPT-CL J0658−4601	104.5208	−46.0274	4.61	0.25	65 ± 22	···	···	···	
SPT-CL J0658−5556*	104.6317	−55.9465	39.05	1.25	490 ± 11	0.296	16.86 ± 2.49	···	a
SPT-CL J0659−5300	104.7763	−53.0114	5.13	0.75	60 ± 12	0.47 ± 0.04	3.38 ± 0.86	5	
SPT-CL J2005−5635	301.3391	−56.5896	4.73	0.50	75 ± 14	0.21 ± 0.02	3.12 ± 0.85	1	b,c
SPT-CL J2006−5325	301.6622	−53.4303	5.38	1.00	55 ± 12	> 1.50	···	1, 10	
SPT-CL J2009−5756	302.4260	−57.9488	4.67	0.75	55 ± 12	> 0.77	···	1	
SPT-CL J2009−4518	302.4496	−45.3116	4.73	2.50	64 ± 13	0.06 ± 0.05	3.57 ± 0.99	7	b,c
SPT-CL J2011−5340	302.7776	−53.6726	4.62	2.50	62 ± 13	> 0.71	···	7	
SPT-CL J2011−5228	302.7786	−52.4725	4.58	0.75	52 ± 19	0.96 ± 0.04	2.59 ± 0.73	1	a,b
SPT-CL J2011−5725	302.8527	−57.4217	5.34	0.75	60 ± 11	0.279	3.52 ± 0.83	1	a
SPT-CL J2011−4900	302.9658	−49.0027	4.71	0.50	62 ± 16	> 0.67	···	2	
SPT-CL J2012−4130	303.0008	−41.5011	5.71	1.25	64 ± 12	0.150	4.23 ± 0.92	6	c
SPT-CL J2012−5649	303.1128	−56.8298	6.38	2.50	73 ± 48	0.055	4.46 ± 0.90	2	c
SPT-CL J2013−5432	303.4944	−54.5441	4.66	0.25	69 ± 19	> 0.88	···	1	
SPT-CL J2015−5504	303.9841	−55.0725	4.62	0.50	59 ± 13	> 0.60	···	2, 8	
SPT-CL J2016−4517	304.0050	−45.2978	4.75	0.75	52 ± 15	0.45 ± 0.03	3.19 ± 0.89	2	b
SPT-CL J2016−4954	304.0129	−49.9144	4.64	0.50	55 ± 15	0.28 ± 0.04	3.28 ± 0.93	5	b
SPT-CL J2017−6258	304.4836	−62.9782	6.32	1.50	67 ± 11	0.535^+	3.87 ± 0.79	3	
SPT-CL J2019−5642	304.7698	−56.7101	5.36	0.75	59 ± 12	0.23 ± 0.02	3.58 ± 0.83	2	c
SPT-CL J2020−6314	305.0273	−63.2434	5.38	0.25	59 ± 14	0.536^+	3.27 ± 0.77	2	13
SPT-CL J2020−4646	305.1900	−46.7697	4.95	1.50	56 ± 20	0.19 ± 0.02	3.64 ± 0.96	1	b,c
SPT-CL J2021−5257	305.4794	−52.9542	4.92	2.50	134 ± 32	0.138	3.67 ± 0.97	1	b,c
SPT-CL J2022−6323	305.5261	−63.3989	6.51	0.25	74 ± 13	0.383^+	4.16 ± 0.84	2	
SPT-CL J2023−5535	305.8376	−55.5906	13.63	1.75	158 ± 14	0.232	7.86 ± 1.24	2	c
SPT-CL J2024−4751	306.0268	−47.8589	4.50	3.00	48 ± 13	> 0.72	···	2	
SPT-CL J2024−4435	306.2465	−44.5881	4.84	3.00	55 ± 13	> 0.71	···	1	
SPT-CL J2025−5117	306.4837	−51.2901	9.11	0.75	106 ± 14	0.22 ± 0.02	6.45 ± 1.11	1	c
SPT-CL J2026−4513	306.6145	−45.2268	5.24	0.50	65 ± 20	0.70 ± 0.05	3.29 ± 0.83	1	
SPT-CL J2027−4240	306.9265	−42.6720	4.75	0.25	59 ± 15	0.30 ± 0.04	3.29 ± 0.91	5	b
SPT-CL J2030−5638	307.7036	−56.6362	5.50	1.00	59 ± 12	0.394^+	3.51 ± 0.80	2	
SPT-CL J2031−4037*	307.9669	−40.6197	17.52	0.75	203 ± 12	0.342	9.83 ± 1.50	6	a
SPT-CL J2032−5627	308.0807	−56.4580	8.61	1.25	93 ± 11	0.284^+	5.48 ± 0.96	6	
SPT-CL J2034−4305	308.5194	−43.0935	4.65	0.50	58 ± 17	0.70 ± 0.03	2.81 ± 0.79	2	b
SPT-CL J2034−5936*	308.5401	−59.6017	8.53	0.25	101 ± 20	0.92 ± 0.07	4.45 ± 0.78	2, 10	a
SPT-CL J2034−6518	308.6587	−65.3103	4.86	0.75	51 ± 18	> 0.69	···	7	
SPT-CL J2035−5251*	308.8012	−52.8519	9.71	0.75	102 ± 13	0.528^+	6.21 ± 1.04	1	
SPT-CL J2035−4813	308.8438	−48.2174	4.52	2.50	63 ± 13	> 0.70	···	2	
SPT-CL J2035−5614	308.9018	−56.2402	4.62	0.25	61 ± 18	> 0.86	···	1	
SPT-CL J2039−5723	309.8237	−57.3866	4.85	0.50	52 ± 12	> 0.86	···	1	
SPT-CL J2039−4143	309.8451	−41.7273	4.66	0.50	55 ± 15	0.66 ± 0.03	2.86 ± 0.80	2	b
SPT-CL J2040−5725	310.0573	−57.4295	6.24	0.50	67 ± 11	0.930^+	3.36 ± 0.70	1, 10	
SPT-CL J2040−5342	310.2194	−53.7116	5.91	0.50	69 ± 18	0.55 ± 0.03	3.97 ± 0.85	1	
SPT-CL J2040−4451	310.2483	−44.8602	6.72	0.25	94 ± 25	1.478^+	3.33 ± 0.66	1, 10	
SPT-CL J2042−4310	310.6008	−43.1683	4.88	0.25	63 ± 20	0.72 ± 0.03	2.94 ± 0.80	3	b
SPT-CL J2043−5614	310.7932	−56.2363	4.54	0.25	56 ± 13	0.68 ± 0.03	2.59 ± 0.72	1	b
SPT-CL J2043−5035*	310.8284	−50.5938	7.18	0.50	87 ± 16	0.723^+	4.53 ± 0.86	1	
SPT-CL J2045−6026	311.3674	−60.4488	4.69	0.25	64 ± 19	> 0.70	···	2	
SPT-CL J2049−3953	312.2651	−39.8905	4.59	0.25	64 ± 23	> 0.72	···	2	
SPT-CL J2049−6144	312.4205	−61.7368	4.50	0.25	57 ± 18	> 0.73	···	2	
SPT-CL J2050−4213	312.5706	−42.2173	7.20	0.75	91 ± 17	0.51 ± 0.03	4.75 ± 0.90	6	
SPT-CL J2051−6256	312.8000	−62.9344	5.03	1.25	47 ± 11	0.47 ± 0.03	3.09 ± 0.80	1	
SPT-CL J2055−5456	313.9957	−54.9368	7.04	0.50	80 ± 12	0.139	4.79 ± 0.92	2	c
SPT-CL J2056−4405	314.1867	−44.0959	4.54	0.25	58 ± 14	0.68 ± 0.06	2.76 ± 0.79	1, 10	b
SPT-CL J2056−5459	314.2174	−54.9937	6.07	0.50	74 ± 13	0.718^+	3.50 ± 0.74	2	
SPT-CL J2058−5608	314.5879	−56.1453	5.01	0.25	65 ± 16	0.606^+	2.94 ± 0.76	1	
SPT-CL J2058−4027	314.7042	−40.4500	4.53	1.25	52 ± 12	> 0.82	···	3	
SPT-CL J2059−5018	314.9322	−50.3057	4.92	0.25	59 ± 14	0.32 ± 0.02	3.48 ± 0.93	1	b
SPT-CL J2100−4548	315.0933	−45.8051	4.75	0.25	63 ± 19	0.712^+	2.92 ± 0.82	1	b
SPT-CL J2100−5708	315.1500	−57.1359	4.76	0.25	57 ± 15	0.57 ± 0.03	2.81 ± 0.77	1	b
SPT-CL J2101−5542	315.3077	−55.7038	5.03	1.00	63 ± 13	0.25 ± 0.02	3.31 ± 0.84	1	
SPT-CL J2101−6123	315.4579	−61.3981	5.53	0.50	61 ± 12	0.68 ± 0.03	3.21 ± 0.74	1	
SPT-CL J2106−5820	316.5130	−58.3467	4.65	0.25	64 ± 19	> 1.50	···	1, 10	
SPT-CL J2106−5844*	316.5206	−58.7451	22.22	0.25	270 ± 42	1.132^+	8.35 ± 1.24	2, 10	
SPT-CL J2106−4421	316.5711	−44.3537	7.59	0.25	104 ± 24	0.70 ± 0.06	4.69 ± 0.87	2, 10	
SPT-CL J2106−6302	316.6540	−63.0491	4.69	1.00	47 ± 11	> 1.50	···	1, 10	

TABLE 4 — *Continued*

SPT ID	R.A. (J2000)	Decl. (J2000)	Best ξ	Best θ_c	Y_{SZ} $\times 10^6$ (arcmin^2)	Redshift	M_{500c} ($10^{14} h_{70}^{-1} M_\odot$)	Imaging	Notes
SPT-CL J2106−6019	316.6640	−60.3299	4.69	0.25	58 ± 19	0.97 ± 0.05	2.44 ± 0.65	1, 8	b
SPT-CL J2108−4445	317.1911	−44.7646	5.60	0.50	65 ± 13	0.88 ± 0.07	3.28 ± 0.76	2, 10	
SPT-CL J2109−5040	317.3825	−50.6765	5.55	2.00	61 ± 12	0.47 ± 0.04	3.81 ± 0.87	1	
SPT-CL J2109−4626	317.4488	−46.4366	4.65	0.25	66 ± 19	0.97 ± 0.09	2.62 ± 0.74	1, 10	b
SPT-CL J2110−5244	317.5514	−52.7492	6.28	0.50	70 ± 14	0.57 ± 0.04	4.20 ± 0.86	1	
SPT-CL J2111−5339	317.9226	−53.6503	5.37	1.00	59 ± 12	0.45 ± 0.03	3.69 ± 0.88	1	
SPT-CL J2112−4434	318.2129	−44.5807	8.80	0.75	104 ± 12	0.52 ± 0.03	5.63 ± 0.98	1	
SPT-CL J2115−4659	318.8011	−46.9910	5.18	3.00	63 ± 13	0.298^+	3.72 ± 0.92	1	
SPT-CL J2118−5055	319.7317	−50.9325	5.54	0.50	68 ± 19	0.625^+	3.61 ± 0.83	1	
SPT-CL J2120−4016	320.1371	−40.2730	5.16	0.75	61 ± 14	0.31 ± 0.04	3.61 ± 0.90	5	
SPT-CL J2120−6518	320.1508	−65.3072	4.53	0.25	58 ± 16	> 0.75	···	2	
SPT-CL J2120−4728	320.1597	−47.4782	5.72	0.25	76 ± 22	0.98 ± 0.07	3.31 ± 0.75	1, 10	14
SPT-CL J2121−5546	320.2690	−55.7782	4.57	0.75	51 ± 11	> 0.51	···	2	
SPT-CL J2121−6335	320.4272	−63.5840	5.58	2.75	76 ± 22	0.217	3.76 ± 0.84	1	c
SPT-CL J2122−4100	320.7089	−41.0058	4.56	1.00	51 ± 12	> 0.71	···	2	
SPT-CL J2124−6124	321.1462	−61.4102	8.50	0.50	90 ± 12	0.435^+	5.19 ± 0.91	2	a
SPT-CL J2125−6113	321.2906	−61.2326	4.91	0.50	51 ± 16	> 1.50	···	1, 10	
SPT-CL J2127−6443	321.9932	−64.7280	4.74	1.75	49 ± 14	> 0.79	···	1	
SPT-CL J2130−4847	322.7081	−48.7996	4.58	3.00	65 ± 13	> 0.73	···	2	
SPT-CL J2130−6238	322.7232	−62.6384	4.62	2.25	53 ± 15	> 0.68	···	2	
SPT-CL J2130−6458	322.7280	−64.9767	7.63	1.00	80 ± 12	0.316^+	4.90 ± 0.91	2	
SPT-CL J2131−4019	322.7659	−40.3216	12.51	0.50	152 ± 12	0.45 ± 0.03	7.51 ± 1.20	1	
SPT-CL J2131−5003	322.9730	−50.0638	4.77	0.50	61 ± 13	0.45 ± 0.03	3.21 ± 0.90	1	b
SPT-CL J2132−4349	323.1698	−43.8288	6.68	1.00	77 ± 12	0.46 ± 0.04	4.50 ± 0.89	5	
SPT-CL J2134−4238	323.5020	−42.6438	8.52	0.75	99 ± 13	0.196	6.01 ± 1.06	6	c
SPT-CL J2134−4109	323.5288	−41.1593	6.80	0.25	88 ± 21	0.66 ± 0.03	4.30 ± 0.85	3	
SPT-CL J2135−5726*	323.9164	−57.4409	10.51	0.50	119 ± 18	0.427^+	6.15 ± 1.02	2	
SPT-CL J2136−6245	324.0354	−62.7534	4.54	0.25	58 ± 18	> 0.83	···	1	
SPT-CL J2136−4704	324.1191	−47.0818	6.24	0.25	79 ± 18	0.425^+	4.37 ± 0.90	1	
SPT-CL J2136−5723	324.1203	−57.3968	4.72	1.00	50 ± 11	> 0.67	···	2	15
SPT-CL J2136−6307	324.2346	−63.1244	6.24	0.75	66 ± 12	0.926^+	3.36 ± 0.70	1, 10	
SPT-CL J2136−5519	324.2393	−55.3196	4.74	0.50	59 ± 20	> 1.50	···	1, 10	
SPT-CL J2137−6437	324.4196	−64.6241	4.76	0.75	52 ± 12	0.89 ± 0.07	2.53 ± 0.68	1, 10	b
SPT-CL J2138−6008	324.5052	−60.1333	12.64	0.75	135 ± 12	0.319^+	7.27 ± 1.16	4	a
SPT-CL J2139−6430	324.9603	−64.5095	4.53	0.25	59 ± 20	> 0.77	···	1	
SPT-CL J2140−5331	325.0330	−53.5178	4.72	0.25	57 ± 16	0.56 ± 0.03	3.06 ± 0.86	1	b
SPT-CL J2140−5727	325.1391	−57.4576	5.35	0.25	62 ± 13	0.405^+	3.39 ± 0.80	2	
SPT-CL J2143−5509	325.8481	−55.1603	5.10	0.25	61 ± 13	> 1.50	···	1, 10	
SPT-CL J2143−4629	325.9576	−46.4998	4.76	2.75	70 ± 15	> 0.70	···	2	
SPT-CL J2145−4348	326.3640	−43.8029	5.32	0.25	69 ± 17	0.48 ± 0.04	3.54 ± 0.85	5	
SPT-CL J2145−5644*	326.4682	−56.7476	12.60	0.50	141 ± 17	0.480^+	6.92 ± 1.10	2	a
SPT-CL J2146−4846	326.5310	−48.7800	5.96	1.00	82 ± 14	0.623^+	3.91 ± 0.84	1	
SPT-CL J2146−4633*	326.6462	−46.5500	9.67	0.50	121 ± 13	0.933^+	5.45 ± 0.91	1, 10	
SPT-CL J2146−5736	326.6957	−57.6148	6.19	0.50	70 ± 13	0.602^+	3.71 ± 0.77	2	
SPT-CL J2148−4843	327.0985	−48.7293	4.77	0.25	75 ± 20	0.97 ± 0.07	2.69 ± 0.75	1, 10	b
SPT-CL J2148−6116*	327.1812	−61.2780	7.47	0.75	79 ± 11	0.571^+	4.46 ± 0.83	2	
SPT-CL J2149−5330	327.3758	−53.5011	4.61	0.50	50 ± 18	0.60 ± 0.03	2.94 ± 0.84	1	b
SPT-CL J2152−5633	328.1450	−56.5632	5.47	1.75	70 ± 13	> 1.50	···	2, 10	
SPT-CL J2152−4629	328.1926	−46.4954	4.83	0.25	64 ± 20	> 1.50	···	1, 10	
SPT-CL J2155−5224	328.8871	−52.4116	5.17	1.75	74 ± 19	0.62 ± 0.03	3.33 ± 0.85	1	
SPT-CL J2155−6048	328.9850	−60.8078	5.74	1.00	60 ± 11	0.539^+	3.51 ± 0.77	1	
SPT-CL J2158−5451	329.5415	−54.8501	5.17	1.25	54 ± 13	> 0.95	···	3	
SPT-CL J2158−4851	329.5692	−48.8533	4.64	0.25	59 ± 19	> 0.65	···	2	
SPT-CL J2159−6244	329.9910	−62.7414	6.49	1.00	71 ± 12	0.392^+	4.14 ± 0.84	2	
SPT-CL J2200−4128	330.1776	−41.4678	4.86	0.75	59 ± 12	0.53 ± 0.03	3.07 ± 0.84	3	a,b
SPT-CL J2200−4741	330.2110	−47.6918	4.67	0.25	67 ± 22	> 0.49	···	5	
SPT-CL J2200−4249	330.2305	−42.8236	4.61	2.50	55 ± 13	> 0.70	···	2	
SPT-CL J2201−5956	330.4734	−59.9437	15.26	1.75	183 ± 13	0.097	9.62 ± 1.50	2	c
SPT-CL J2203−5047	330.7988	−50.7899	5.66	1.25	67 ± 15	1.14 ± 0.09	3.05 ± 0.71	2, 9	
SPT-CL J2203−4953	330.8529	−49.8882	4.69	0.25	61 ± 15	> 0.66	···	2	
SPT-CL J2203−5817	330.9185	−58.2994	4.67	0.75	51 ± 13	> 0.82	···	7	
SPT-CL J2205−5927	331.2665	−59.4564	5.55	1.00	63 ± 12	0.32 ± 0.03	3.95 ± 0.89	6	
SPT-CL J2206−4217	331.5243	−42.2917	4.57	0.75	47 ± 18	> 0.93	···	2	
SPT-CL J2206−4057	331.6183	−40.9525	4.63	0.50	56 ± 13	0.42 ± 0.04	3.01 ± 0.85	5	b
SPT-CL J2206−5807	331.6558	−58.1290	6.24	0.75	71 ± 13	0.60 ± 0.03	4.08 ± 0.84	6	

TABLE 4 — *Continued*

SPT ID	R.A. (J2000)	Decl. (J2000)	Best ξ	Best θ_c	Y_{SZ} $\times 10^6$ (arcmin^2)	Redshift	M_{500c} ($10^{14} h_{70}^{-1} M_\odot$)	Imaging	Notes
SPT-CL J2207−4752	331.9363	−47.8725	4.59	2.00	55 ± 14	> 0.67	···	2	
SPT-CL J2211−4833	332.8260	−48.5603	7.40	1.75	87 ± 13	0.24 ± 0.03	5.16 ± 0.97	6	c
SPT-CL J2214−4642	333.7184	−46.7050	7.17	0.25	90 ± 25	1.15 ± 0.08	3.77 ± 0.72	1, 10	3
SPT-CL J2217−6509	334.4895	−65.1506	6.77	3.00	117 ± 26	0.095	4.97 ± 0.98	2	16,c
SPT-CL J2218−5532	334.5420	−55.5468	4.94	0.25	71 ± 18	0.69 ± 0.06	3.04 ± 0.83	2, 10	b
SPT-CL J2218−4519*	334.7486	−45.3205	8.84	0.75	101 ± 12	0.65 ± 0.03	5.31 ± 0.92	2	
SPT-CL J2219−5708	334.9614	−57.1384	8.91	0.75	105 ± 13	0.33 ± 0.04	6.07 ± 1.05	5	
SPT-CL J2220−4534	335.0809	−45.5824	7.07	0.75	77 ± 12	0.59 ± 0.03	4.46 ± 0.86	6	
SPT-CL J2222−4834*	335.7122	−48.5735	9.08	0.50	99 ± 14	0.652^+	5.42 ± 0.93	1	
SPT-CL J2223−5015	335.8144	−50.2664	4.86	0.25	4 ± 73	0.24 ± 0.04	3.46 ± 0.94	5	b,c
SPT-CL J2223−5227	335.8669	−52.4651	4.85	0.75	57 ± 13	0.27 ± 0.03	3.42 ± 0.93	6	b
SPT-CL J2228−5828	337.2153	−58.4686	5.15	1.50	57 ± 12	0.71 ± 0.06	3.17 ± 0.82	2, 10	
SPT-CL J2229−4320	337.3891	−43.3411	4.66	0.25	71 ± 16	0.56 ± 0.03	2.90 ± 0.81	3	b
SPT-CL J2231−5247	337.9800	−52.7906	4.51	0.25	71 ± 19	> 0.76	···	2	
SPT-CL J2232−5959*	338.1487	−59.9903	8.80	0.25	112 ± 22	0.594^+	5.55 ± 0.97	2	a
SPT-CL J2232−6151	338.2319	−61.8558	5.04	2.25	58 ± 16	0.71 ± 0.06	3.02 ± 0.80	2, 10	
SPT-CL J2233−5339*	338.3295	−53.6502	8.29	1.00	97 ± 13	0.48 ± 0.03	5.48 ± 0.98	2	
SPT-CL J2233−4729	338.3648	−47.4912	4.59	0.25	62 ± 21	> 0.68	···	6	
SPT-CL J2235−4416	338.8637	−44.2694	5.38	1.00	65 ± 12	0.45 ± 0.03	3.55 ± 0.84	2	
SPT-CL J2236−4555*	339.2186	−45.9279	7.72	0.25	110 ± 25	1.16 ± 0.08	4.02 ± 0.74	2, 10	
SPT-CL J2241−4001	340.3170	−40.0182	4.78	0.50	51 ± 13	0.64 ± 0.03	2.90 ± 0.80	6	b
SPT-CL J2241−4558	340.4365	−45.9685	6.49	0.25	95 ± 22	0.98 ± 0.07	3.63 ± 0.74	1, 10	
SPT-CL J2241−4236	340.4749	−42.6004	5.29	1.25	56 ± 11	0.20 ± 0.03	3.76 ± 0.90	6	c
SPT-CL J2242−4435	340.5195	−44.5897	4.65	0.25	52 ± 13	0.73 ± 0.04	2.73 ± 0.77	2	b
SPT-CL J2245−6206*	341.2604	−62.1136	8.74	1.00	101 ± 12	0.58 ± 0.03	5.40 ± 0.94	2	
SPT-CL J2248−4431*	342.1907	−44.5269	42.36	0.75	475 ± 12	0.351^+	17.27 ± 2.54	6	a
SPT-CL J2249−4442	342.4069	−44.7158	5.11	0.25	67 ± 19	0.60 ± 0.03	3.18 ± 0.81	6	
SPT-CL J2249−6426	342.4296	−64.4342	5.96	2.25	82 ± 35	0.094	4.41 ± 0.93	5	c
SPT-CL J2250−4808	342.6823	−48.1447	5.82	0.25	72 ± 16	0.91 ± 0.09	3.32 ± 0.73	7, 10	
SPT-CL J2251−4848	342.7891	−48.8032	6.42	0.25	86 ± 20	0.79 ± 0.06	3.82 ± 0.78	2, 10	
SPT-CL J2254−6314	343.5145	−63.2450	8.18	1.25	92 ± 14	0.211	5.70 ± 1.02	3	c
SPT-CL J2254−4907	343.5870	−49.1274	4.78	0.50	57 ± 18	1.11 ± 0.13	2.48 ± 0.67	2	b
SPT-CL J2254−4620	343.5880	−46.3436	8.37	1.25	90 ± 14	0.27 ± 0.03	5.68 ± 1.01	6	
SPT-CL J2254−5805	343.5895	−58.0851	5.36	2.25	95 ± 24	0.153	3.50 ± 0.81	5	c
SPT-CL J2255−5256	343.8763	−52.9463	4.60	0.25	54 ± 18	> 0.69	···	2	
SPT-CL J2256−5414	344.0024	−54.2436	4.65	0.50	47 ± 12	> 0.69	···	2	
SPT-CL J2258−4044*	344.7051	−40.7386	10.95	0.25	152 ± 29	0.83 ± 0.07	5.88 ± 0.95	2, 10	
SPT-CL J2259−6057*	344.7528	−60.9546	9.77	0.50	113 ± 14	0.75 ± 0.03	5.61 ± 0.94	2	
SPT-CL J2259−3952	344.8138	−39.8740	9.02	0.75	105 ± 12	0.56 ± 0.03	5.55 ± 0.96	6	16
SPT-CL J2259−5431	344.9818	−54.5294	5.39	0.25	54 ± 14	0.39 ± 0.04	3.28 ± 0.76	3	
SPT-CL J2259−5617	344.9955	−56.2859	5.73	0.75	55 ± 11	0.153	3.75 ± 0.81	1	c
SPT-CL J2300−5148	345.0615	−51.8003	4.92	2.00	50 ± 13	> 0.91	···	2	
SPT-CL J2300−4500	345.1038	−45.0115	4.74	0.25	61 ± 19	0.64 ± 0.03	2.88 ± 0.80	6	b
SPT-CL J2300−5331	345.1761	−53.5190	6.44	1.00	62 ± 11	0.262^+	4.07 ± 0.82	2	
SPT-CL J2300−5233	345.2343	−52.5507	4.64	0.25	53 ± 17	> 0.64	···	1	
SPT-CL J2301−5546	345.4669	−55.7768	5.01	0.50	51 ± 16	0.748^+	2.69 ± 0.69	1	
SPT-CL J2301−4023*	345.4687	−40.3912	8.09	0.50	107 ± 19	0.73 ± 0.04	4.81 ± 0.86	2	
SPT-CL J2302−4435	345.5851	−44.5850	4.67	0.25	57 ± 15	0.35 ± 0.05	3.10 ± 0.87	7	b
SPT-CL J2306−5120	346.6121	−51.3370	4.68	0.25	50 ± 12	1.27 ± 0.10	2.17 ± 0.52	2, 10	b
SPT-CL J2306−6505*	346.7298	−65.0910	9.22	0.75	99 ± 12	0.530^+	5.73 ± 0.98	2	
SPT-CL J2308−4834	347.2351	−48.5679	5.14	0.25	65 ± 19	> 1.50	···	2, 10	
SPT-CL J2309−4130	347.3891	−41.5159	4.57	0.75	58 ± 13	> 0.70	···	2	
SPT-CL J2311−4203	347.8447	−42.0637	5.80	1.00	62 ± 13	1.15 ± 0.08	3.04 ± 0.68	2, 10	
SPT-CL J2311−5820	347.9924	−58.3452	5.72	0.25	64 ± 18	0.85 ± 0.07	3.01 ± 0.67	1, 10	
SPT-CL J2312−4621	348.0560	−46.3523	6.86	1.25	74 ± 12	0.63 ± 0.04	4.28 ± 0.84	6	
SPT-CL J2313−4243	348.4995	−42.7256	5.47	1.75	39 ± 26	0.056	4.06 ± 0.92	6	c
SPT-CL J2316−4500	349.1950	−45.0035	4.64	0.50	61 ± 16	0.73 ± 0.04	2.73 ± 0.76	2	b
SPT-CL J2316−5453	349.2082	−54.8978	6.23	1.00	56 ± 11	0.39 ± 0.05	3.80 ± 0.79	1	
SPT-CL J2317−4707	349.2757	−47.1213	4.76	0.25	63 ± 19	0.65 ± 0.04	2.88 ± 0.80	6	b
SPT-CL J2319−4716	349.9828	−47.2787	6.17	1.50	62 ± 12	0.46 ± 0.03	4.09 ± 0.85	2	
SPT-CL J2321−5419	350.4022	−54.3231	5.27	0.25	57 ± 11	> 0.97	···	1	1
SPT-CL J2325−4111*	351.3043	−41.1959	12.50	1.50	134 ± 11	0.358^+	7.55 ± 1.20	1	a
SPT-CL J2327−5137	351.7818	−51.6189	4.94	0.25	49 ± 12	0.32 ± 0.02	3.04 ± 0.79	1	b
SPT-CL J2328−4616	352.0576	−46.2802	4.84	2.75	52 ± 18	> 0.77	···	6	
SPT-CL J2329−5831	352.4733	−58.5245	6.62	0.25	67 ± 12	0.75 ± 0.07	3.60 ± 0.72	1, 10	

TABLE 4 — *Continued*

SPT ID	R.A. (J2000)	Decl. (J2000)	Best ξ	Best θ_c	Y_{SZ} $\times 10^6$ (arcmin^2)	Redshift	M_{500c} ($10^{14} h_{70}^{-1} M_\odot$)	Imaging	Notes
SPT-CL J2330−4502	352.5708	−45.0344	5.18	1.50	61 ± 12	0.31 ± 0.03	3.55 ± 0.88	6	
SPT-CL J2331−5051*	352.9608	−50.8639	10.47	0.25	106 ± 14	0.576^+	5.60 ± 0.92	2	a
SPT-CL J2332−5053	353.0273	−50.8895	4.58	0.25	86 ± 16	0.56 ± 0.03	2.60 ± 0.71	2	a,b
SPT-CL J2332−5358	353.1057	−53.9675	9.12	1.50	106 ± 15	0.402^+	5.29 ± 0.91	2	17,a
SPT-CL J2335−4544*	353.7861	−45.7389	10.37	1.00	112 ± 12	0.547^+	6.17 ± 1.02	2	
SPT-CL J2335−4243	353.9710	−42.7328	5.59	0.75	62 ± 12	0.72 ± 0.06	3.38 ± 0.77	7, 10	
SPT-CL J2337−5942*	354.3523	−59.7049	20.35	0.25	197 ± 14	0.775^+	8.43 ± 1.27	2	a
SPT-CL J2337−5912	354.3989	−59.2046	4.81	0.50	49 ± 12	0.60 ± 0.03	2.70 ± 0.72	1	b
SPT-CL J2339−4058	354.7996	−40.9697	4.75	0.25	68 ± 21	> 0.89	···	3	
SPT-CL J2341−5119*	355.2991	−51.3281	12.49	0.75	127 ± 11	1.003^+	5.59 ± 0.89	2	
SPT-CL J2341−5724	355.3568	−57.4158	6.87	1.00	63 ± 11	1.38 ± 0.08	3.05 ± 0.60	1, 10	
SPT-CL J2342−5411*	355.6892	−54.1856	8.18	0.25	92 ± 20	1.075^+	3.93 ± 0.70	1, 10	a
SPT-CL J2342−4714	355.7453	−47.2412	4.89	0.25	61 ± 15	0.42 ± 0.03	3.20 ± 0.86	6	b
SPT-CL J2344−4224	356.1481	−42.4100	4.54	1.25	50 ± 13	0.29 ± 0.03	3.07 ± 0.88	6	b
SPT-CL J2344−4243*	356.1847	−42.7209	27.44	0.50	330 ± 20	0.596^+	12.05 ± 1.79	1	a
SPT-CL J2345−6405*	356.2555	−64.0959	9.42	0.50	108 ± 15	0.94 ± 0.07	5.10 ± 0.86	2, 10	
SPT-CL J2350−5301	357.7272	−53.0212	6.05	0.25	64 ± 15	0.54 ± 0.03	3.53 ± 0.74	1	
SPT-CL J2351−5452	357.8978	−54.8829	6.28	0.75	63 ± 11	0.384	3.84 ± 0.79	1	a
SPT-CL J2352−5846	358.0510	−58.7758	5.18	0.75	47 ± 11	> 0.67	···	2	18
SPT-CL J2352−4657*	358.0631	−46.9569	7.46	0.25	89 ± 12	0.73 ± 0.07	4.42 ± 0.83	2, 10	
SPT-CL J2352−6134	358.1939	−61.5671	6.07	0.25	84 ± 20	0.70 ± 0.06	3.75 ± 0.79	7, 10	
SPT-CL J2353−5512	358.2559	−55.2050	5.10	0.50	51 ± 11	> 1.50	···	2, 10	
SPT-CL J2354−5633	358.7122	−56.5545	5.70	0.75	56 ± 11	0.53 ± 0.03	3.34 ± 0.73	1	
SPT-CL J2355−5055*	358.9498	−50.9320	6.60	0.75	68 ± 11	0.320^+	4.10 ± 0.82	6	
SPT-CL J2356−4220	359.0127	−42.3496	5.28	0.25	74 ± 20	0.76 ± 0.06	3.12 ± 0.78	2, 10	
SPT-CL J2356−6014	359.0821	−60.2448	4.62	1.25	46 ± 11	> 0.70	···	2	
SPT-CL J2358−5229	359.5314	−52.4840	4.51	0.25	45 ± 15	0.64 ± 0.03	2.51 ± 0.68	1	b
SPT-CL J2358−4143	359.6421	−41.7173	4.74	1.50	58 ± 12	> 0.67	···	6	
SPT-CL J2358−6129	359.7075	−61.4862	5.85	1.25	69 ± 12	0.37 ± 0.03	4.00 ± 0.86	6	
SPT-CL J2358−4354	359.7306	−43.9026	5.80	1.00	67 ± 12	0.60 ± 0.04	3.67 ± 0.80	7	
SPT-CL J2359−5727	359.8859	−57.4579	4.51	0.25	47 ± 15	···	···	···	
SPT-CL J2359−5009*	359.9230	−50.1649	6.68	1.00	70 ± 11	0.775^+	3.60 ± 0.71	2	a

NOTE. — Galaxy cluster candidates selected above a significance of 4.5 in the 2500 deg^2 SPT-SZ survey. Galaxy clusters marked by a '*' have X-ray data from the *Chandra* satellite that are used in the cosmological analysis presented in dH14. For each candidate we report the position, the highest detection significance in the filtered maps and the core radius corresponding to the detection (in arcmin; see §3), the integrated Y_{SZ} within a $0.75'$ aperture, the redshift for confirmed systems (except for the three highest-redshift systems; see §5.3) or redshift lower limit for unconfirmed systems (see §4), and a mass estimate for each confirmed cluster (§6.1). Spectroscopic redshifts are quoted without uncertainties, which are typically $\sim 0.1\%$ (see e.g., Ruel et al. 2013). The spectroscopic redshifts derived from SPT follow-up observations are marked with a '+'.

[a] Strong-Lensing Cluster

[b] Cluster masses at low significance are only approximate; see §6.1.

[c] Cluster masses at low redshift ($z < 0.25$) may be underestimated; see §6.1.

[d] Confirmed, high-redshift cluster (see §5.3)

[1] Bright star impedes confirmation

[2] Possibly biased SZ-center owing to cluster's proximity to the edge of the cluster map; additional cluster offset $1.8'$ at $z \sim 0.55$

[3] Foreground group at $z \sim 0.3$

[4] Foreground group to N at $z \sim 0.35$.

[5] Foreground group at $z \sim 0.1$

[6] Group $z \sim 0.2$ centered $3'$ away from SPT center

[7] Small group $z \sim 0.4$ offset $2'$ to N

[8] Low-z group $z \sim 0.1$

[9] Very complex region; optical group on NW $z \sim 0.4$ and another group on SW $z \sim 0.65$. Confirmed in S12 by 1 method at $z = 0.38 \pm 0.04$.

[10] Bimodal redshift solution; additional solution $z = 0.29$

[11] High stellar density

[12] Foreground group at $z \sim 0.15$.

[13] Bimodal redshift solution; additional solution $z = 0.41$

[14] Group on SW $z \sim 0.4$.

[15] System $z \sim 0.3$ offset $2'$ to S

[16] Possibly biased SZ-center owing to cluster's proximity to the edge of the cluster map

[17] The mass is biased low by a factor of $\sim 1.5\times$ owing to contamination from a magnified high-redshift dusty star forming galaxy; see §6.4.3 and discussion in Andersson et al. (2011).

[18] Low-z group at $z \sim 0.15$ $>3'$ from SPT center

TABLE 5
Clusters with matches in other catalogs

SPT ID	First ID, ref.	All catalogs with match	z	Lit. z, ref.
SPT-CL J0010−5112	ACO S0013, 1	1	0.17± 0.02	–
SPT-CL J0013−4621	[BM78] 210, 2	1,2	0.18± 0.05	–
SPT-CL J0027−5015	Str 0025−505, 3	1,3,4,5,6	0.145	0.1448,[4]
SPT-CL J0036−4411	SpARCS J003645−441050, 7	7	0.869	0.869,[7]
SPT-CL J0041−4428	ACO S0067, 1	1	0.33± 0.02	–
SPT-CL J0051−4834	Str 0049−489, 3	1,3	0.187	0.1873,[8]
SPT-CL J0102−4915	ACT-CL J0102−4915, 9	6,9,10	0.870	0.8701,[11]
SPT-CL J0108−4341	ACO 2873, 1	1	0.19± 0.02	–
SPT-CL J0118−5638	[BM78] 148, 2	1,2	0.21± 0.04	–
SPT-CL J0124−5937	PSZ1 G295.19−56.99, 6	6	0.21± 0.03	0.22,[6]
SPT-CL J0129−6432	RXC J0129.4−6432, 12	12	0.326	0.3264,[12]
SPT-CL J0133−6434	PSZ1 G295.60−51.95, 6	6	0.29± 0.04	0.33,[6]
SPT-CL J0135−5904	PSZ1 G292.40−57.11, 6	6	0.49± 0.03	–
SPT-CL J0145−5301	Sersic 017/04, 13	1,4,5,9,13,14	0.117	0.1168,[4]
SPT-CL J0145−6033	RBS 0238, 15	4,6,15	0.179	0.1795,[16]
SPT-CL J0214−4638	QW 0213−468, 17	17	0.27± 0.02	–
SPT-CL J0216−4816	ACO 2998, 1	1,8,18	0.171	0.1709,[8]
SPT-CL J0217−5245	RXC J0217.2−5244, 4	4,9	0.343	0.3432,[4]
SPT-CL J0225−4155	ACO 3017, 1	1,4,8,14,19,20	0.220	0.2195,[8]
SPT-CL J0232−4421	[DBG99] 27, 14	8,10,14,15,20	0.284	0.2836,[14]
SPT-CL J0232−5257	ACT-CL J0232−5257, 9	9	0.556	0.5559,[21]
SPT-CL J0235−5121	ACT-CLJ0235−5121, 9	6,9	0.278	0.2777,[21]
SPT-CL J0236−4938	ACT-CLJ0237−4939, 9	9	0.334	0.4,[22]
SPT-CL J0243−4833	SPT-CL J0243−4833, 10	6,10	0.500	0.53,[10]
SPT-CL J0254−5857	SPT-CL J0254−5856, 10	10,20,23,24	0.438	0.438,[24]
SPT-CL J0256−4736	ACO 3072, 1	1	0.23± 0.03	–
SPT-CL J0304−4401	SPT-CL J0304−4401, 10	6,10	0.458	0.52,[10]
SPT-CL J0304−4921	ACT-CL J0304−4921, 9	6,9	0.392	0.3922,[21]
SPT-CL J0307−4123	PSZ1 G248.96−58.75, 6	6	0.67± 0.04	–
SPT-CL J0311−6354	PSZ1 G281.29−46.89, 6	6	0.25± 0.02	0.28,[6]
SPT-CL J0317−4849	ACO 3113, 1	1,6,8	0.164	0.1642,[25]
SPT-CL J0328−5541	ACO 3126, 1	1,4,14,15,18,20,23,26	0.084	0.0844,[27]
SPT-CL J0330−5228	ACT-CLJ0330−5227, 9	9	0.442	0.44,[22]
SPT-CL J0346−5439	ACT-CL J0346−5438, 9	9	0.530	0.5297,[21]
SPT-CL J0348−4515	ClG 0346−4524, 28	17,28	0.358	0.3251,[28]
SPT-CL J0404−6510	[BM78] 082, 2	1,2,6,23	0.12± 0.03	0.11,[29]
SPT-CL J0411−4819	SPT-CL J0411−4819, 10	10,20	0.422	0.42,[10]
SPT-CL J0411−6340	ACO 3230, 1	1,15	0.14± 0.01	0.14,[29]
SPT-CL J0431−6126	Sersic 040/06, 13	1,3,4,13,14,18,20,23,26,30,31,32	0.058	0.0577,[27]
SPT-CL J0438−5419	ACT-CL J0438−5419, 9	9,10,20	0.421	0.4214,[21]
SPT-CL J0458−5741	ACO 3298, 1	1,23	0.19± 0.02	–
SPT-CL J0500−5116	ACO 3303, 1	1,33	0.11± 0.03	0.14,[25]
SPT-CL J0504−4929	ACO 3311, 1	1	0.20± 0.03	–
SPT-CL J0505−6145	PSZ1 G271.28−36.12, 6	6	0.25± 0.03	–
SPT-CL J0509−5342	SPT-CL J0509−5342, 34	9,10,23,34,35,36	0.461	0.4626,[37]
SPT-CL J0509−6118	PSZ1 G270.64−35.68, 6	6	0.35± 0.03	0.31,[6]
SPT-CL J0510−4519	ACO 3322, 1	1,4,15,17,20,38	0.20	0.20,[27]
SPT-CL J0511−5154	SCSO J051145−515430, 39	23,35,39	0.645	0.645,[24]
SPT-CL J0512−5139	SCSO J051240−513941, 39	36,39	0.60± 0.03	0.66,[39]
SPT-CL J0516−5430	ACO S0520, 1	1,4,9,20,23,34,35,36,39	0.295	0.2952,[4]
SPT-CL J0519−4248	RCS J051919−4247.8, 40	40	0.59± 0.03	0.6,[40]
SPT-CL J0521−5104	SCSO J052113−510418, 39	21,23,35,36,39	0.675	0.6755,[21]
SPT-CL J0522−4818[a]	DLSCL J0522.2−4820, 41	1,33,41	0.296	0.296,[42]
SPT-CL J0522−5026	SCSO J052200−502700, 39	36,39	0.52± 0.03	0.5,[39]
SPT-CL J0525−4715	ACO 3343, 1	1,4,20	0.191	0.1913,[4]
SPT-CL J0528−5300	SPT-CL J0528−5300, 34	9,23,34,35,39	0.768	0.7648,[43]
SPT-CL J0535−4801	PSZ1 G254.58−32.16, 6	6	0.92± 0.07	–
SPT-CL J0542−4100	RDCS J0542−4100, 44	44,45	0.642	0.63,[44]
SPT-CL J0546−5345	SPT-CL J0547−5346, 34	9,23,34,35	1.066	1.067,[46]
SPT-CL J0549−6205	SPT-CL J0549−6204, 10	10,20	0.376	0.32,[10]
SPT-CL J0550−5019	LCS-CL J055019−5019.6, 36	36	0.65± 0.03	0.66,[36]
SPT-CL J0555−6406	SPT-CL J0555−6405, 10	6,10	0.345	0.42,[10]
SPT-CL J0559−5249	SPT-CL J0559−5249, 35	6,9,23,35	0.609	0.6112,[43]
SPT-CL J0603−4714	PSZ1 G254.54−27.32, 6	6	0.32± 0.04	0.27,[6]
SPT-CL J0611−5938	PLCKESZ G268.5−28.1;, 47	47	0.39± 0.03	0.47,[47]
SPT-CL J0615−5746	SPT-CL J0615−5746, 10	6,10,48	0.972	0.972,[10]
SPT-CL J0628−4143	ACO 3396, 1	1,4,6,10,14	0.176	0.1759,[14]
SPT-CL J0637−4829	ACO 3399, 1	1,4,20	0.203	0.2026,[4]
SPT-CL J0638−5358	ACO S0592, 1	1,4,9,10,14,20	0.226	0.2216,[14]
SPT-CL J0641−5001	ACO 3403, 1	1,33	0.123	0.1226,[49]
SPT-CL J0645−5413	ACO 3404, 1	1,4,9,10,14,20,33	0.164	0.167,[14]
SPT-CL J0651−4037	PSZ1 G250.29−17.29, 6	6	0.27± 0.02	0.27,[6]
SPT-CL J0658−5556	1E 0657−55.8 (Bullet), 50	4,9,10,14,20,50	0.296	0.296,[50]
SPT-CL J2011−5725	RXC J2011.3−5725, 4	4,23	0.279	0.2786,[4]

TABLE 5 — *Continued*

SPT ID	First ID, ref.	All catalogs with match	z	Lit. z, ref.
SPT-CL J2012−4130	[BM78] 236, 2	1,2,4,6	0.150	0.1496,[4]
SPT-CL J2012−5649	Str 2008−569, 3	1,2,3,4,14,15,17,20,23,31,33	0.055	0.0556,[27]
SPT-CL J2020−4646	ACO 3673, 1	1,23	0.19± 0.02	0.19,[23]
SPT-CL J2021−5257	Ser 138−5, 13	1,3,4,13,23	0.138	0.1383,[4]
SPT-CL J2023−5535	RXC J2023.4−5535, 4	4,10,20,23	0.232	0.232,[4]
SPT-CL J2025−5117	[BM78] 188, 2	1,2,6,23	0.22± 0.02	0.18,[23]
SPT-CL J2031−4037	RXC J2031.8−4037, 4	4,10	0.342	0.3416,[4]
SPT-CL J2032−5627[b]	[F81] 391, 51	1,4,6,23,33,51	0.284	0.284,[24]
SPT-CL J2055−5456	[BM78] 164, 2	1,2,4,23	0.139	0.139,[4]
SPT-CL J2059−5018	ACO S0912, 1	1,23	0.32± 0.02	0.41,[23]
SPT-CL J2101−5542	ACO 3732;, 1	1,23	0.25± 0.02	0.2,[23]
SPT-CL J2121−6335	ACO S0937, 1	1,23,52	0.217	0.217,[52]
SPT-CL J2134−4238	[BM78] 253, 2	1,2,6,31,51	0.196	0.1955,[27]
SPT-CL J2138−6008	SPT-CL J2138−6007, 23	6,23	0.319	0.319,[24]
SPT-CL J2148−6116	SPT-CL J2148−6116, 23	6,23	0.571	0.571,[24]
SPT-CL J2201−5956	[F81] 408, 51	1,4,10,14,15,18,20,23,26,51	0.097	0.0972,[27]
SPT-CL J2211−4833	[BM78] 202, 2	1,2	0.24± 0.03	0.0576,[53]
SPT-CL J2217−6509	Sersic 150/06, 13	2,3,4,13,14,17,20	0.095	0.0951,[14]
SPT-CL J2223−5015	APMCC 769, 18	18	0.24± 0.04	–
SPT-CL J2223−5227	ACO 3872, 1	1	0.27± 0.03	–
SPT-CL J2241−4001	EIS J2241−4001, 54	54,55	0.64± 0.03	1,[55]
SPT-CL J2241−4236	[BM78] 259, 2	1,2,8,31	0.20± 0.03	–
SPT-CL J2248−4431	ACO S1063, 1	1,4,8,10,14,15,20	0.351	0.3475,[4]
SPT-CL J2249−6426	[BM78] 108, 2	1,2,4,14,18,20,26,33	0.094	0.094,[56]
SPT-CL J2254−4620	ACO 3937, 1	1	0.27± 0.03	–
SPT-CL J2254−5805	[R76] 89, 57	3,14,57	0.153	–
SPT-CL J2254−6314	AM 2250−633, 31	4,14,31	0.211	0.2112,[14]
SPT-CL J2259−5617	[BM78] 165, 2	1,2,6,23,31,35	0.153	0.17,[23]
SPT-CL J2300−5331	ACO S1079, 1	1,23,35	0.262	0.262,[24]
SPT-CL J2301−4023	[LP96] Cl2259−4040, 58	58	0.73± 0.04	–
SPT-CL J2306−6505	PSZ1 G319.20−48.61, 6	6	0.530	0.69,[6]
SPT-CL J2313−4243	Sersic 159/03, 13	1,2,3,4,6,8,13,14,15,17,38,57	0.056	0.0564,[4]
SPT-CL J2316−5453	SCSO J231651−545356, 39	36,39,59	0.39± 0.05	0.44,[39]
SPT-CL J2325−4111[c]	ACO S1121, 1	1,6,10	0.358	0.358,[24]
SPT-CL J2327−5137	LCS-CL J232708−5137.5, 36	36	0.32± 0.02	0.37,[36]
SPT-CL J2332−5358	SCSO J233227−535827, 39	23,35,36,39	0.402	0.402,[24]
SPT-CL J2335−4544	PSZ1 G337.11−66.02, 6	6	0.547	0.5,[6]
SPT-CL J2344−4243	SPT-CL J2344−4243, 10	6,10	0.596	0.596,[60]
SPT-CL J2350−5301	SCSO J235055−530124, 39	39	0.54± 0.03	0.46,[39]
SPT-CL J2351−5452	SCSO J235055−530124, 39	23,36,39	0.384	0.3838,[61]
SPT-CL J2354−5633	SCSO J235454−563311, 39	39	0.53± 0.03	0.51,[39]

References. — [1] ACO catalog Abell et al. (1989); [2] Braid & MacGillivray (1978); [3] Stromlo catalog Duus & Newell (1977); [4] REFLEX catalog Böhringer et al. (2004); [5] Panko & Flin (2006); [6] Planck Cluster catalog Planck Collaboration et al. (2013a); [7] GCLASS catalog Muzzin et al. (2012); [8] Cruddace et al. (2002); [9] ACT-CL Catalog Marriage et al. (2011); [10] SPT-CL catalog Williamson et al. (2011); [11] Menanteau et al. (2012); [12] REFLEX II Catalog Chon & Böhringer (2012); [13] Sersic catalog Sérsic (1974); [14] [DBG99] catalog de Grandi et al. (1999); [15] RBS catalog Schwope et al. (2000); [16] Guzzo et al. (2009); [17] [QW] catalog Quintana & White (1990); [18] APMCC catalog Dalton et al. (1997); [19] Edinburgh-Durham Cluster Catalog Lumsden et al. (1992); [20] Planck Early SZ catalog Planck Collaboration et al. (2011a); [21] Sifón et al. (2013); [22] Menanteau et al. (2010b); [23] SPT-CL catalog Reichardt et al. (2013); [24] Ruel et al. (2013); [25] Coziol et al. (2009); [26] [DEM94] catalog Dalton et al. (1994); [27] Struble & Rood (1999); [28] West & Frandsen (1981); [29] Ebeling et al. (1996); [30] Lugger (1978); [31] Arp & Madore (1996); [32] Edge et al. (1990); [33] Einasto et al. (1997); [34] SPT-CL catalog Staniszewski et al. (2009); [35] SPT-CL catalog Vanderlinde et al. (2010); [36] LCS Catalog Bleem et al. (2014); [37] High et al. (2010); [38] Gioia et al. (1990); [39] Menanteau et al. (2010a); [40] Horesh et al. (2010); [41] Deep Lens Survey Cluster Catalog Wittman et al. (2006); [42] Abate et al. (2009); [43] High et al. (2010); [44] Tozzi et al. (2003); [45] 400d Cluster Catalog Burenin et al. (2007); [46] Brodwin et al. (2010); [47] Planck Collaboration et al. (2012); [48] Planck Collaboration et al. (2011b); [49] Coziol et al. (2009); [50] Tucker et al. (1998); [51] Feitsova (1981); [52] Webb et al. (2013); [53] Batuski et al. (1999); [54] Olsen et al. (1999); [55] Lobo et al. (2000); [56] Katgert et al. (1996); [57] Rose (1976); [58] Lidman & Peterson (1996); [59] XMM-BCS catalog Šuhada et al. (2012); [60] McDonald et al. (2012); [61] Buckley-Geer et al. (2011)

Note. — Cluster candidates coincident with galaxy clusters identified in other catalogs. We define a match if a candidate is within $5'$ ($2'$) of an identified cluster for clusters at $z \leq 0.3$ ($z > 0.3$ or unconfirmed). For each match, we report the name under which the cluster was first reported and all catalogs which include the cluster. We also quote the cluster redshift used in this work—either the photometric redshift or a spectroscopic redshift obtained from follow-up observations or the literature. We include error bars for red sequence redshifts but not spectroscopic redshifts. In the last column, we quote a redshift from the literature if available. Error bars are not reported for literature redshifts; two (three or four) significant digits are used if the literature redshift is photometric (spectroscopic), with the exception of SPT-CL J0510−4519 for which the literature spectroscopic redshift is reported to two significant figures.

[a] ACO 3338 is in the foreground.

[b] [F81] 391/ACO 3685 is in the foreground.

[c] ACO S1121 is in the foreground.